Alma Mater Studiorum · Università di Bologna

SCUOLA DI SCIENZE
Corso di Laurea in Astrofisica e Cosmologia
Dipartimento di Fisica e Astronomia

RADIO RELICS AND MAGNETIC FIELDS IN GALAXY CLUSTERS

Tesi di Laurea in Astrofisica e Cosmologia

Relatore:
Chiar.mo Prof.
Daniele DALLACASA

Candidato:
Andrea BOTTEON

Co-Relatore:
Dr. **Gianfranco BRUNETTI**

Sessione I
Anno Accademico 2014/2015

THIS THESIS WORK WAS DONE AS PART OF THE RESEARCH ACTIVITY OF THE ISTITUTO DI RADIOASTRONOMIA - ISTITUTO NAZIONALE DI ASTROFISICA (BOLOGNA)

Abstract

Radio relics are diffuse synchrotron sources generally located in the peripheries of galaxy clusters in merging state. According to the current leading scenario, relics trace gigantic cosmological shock waves that cross the intra-cluster medium where particle acceleration occurs. The relic/shock connection is supported by several observational facts, including the arc-shaped morphologies of relics, their high polarization and the spatial coincidence between relics and shocks found in the X-rays.

Under the assumptions that particles are accelerated at the shock front and are subsequently deposited and then age downstream of the shock, Markevitch et al. (2005) proposed a method to constrain the magnetic field strength in radio relics. Measuring the thickness of radio relics at different frequencies allows to derive combined constraints on the velocity of the downstream-flow and on the magnetic field, which in turns determines particle aging. We elaborate this idea to infer first constraints on magnetic fields in cluster outskirts. We consider three models of particle aging and develop a geometric model to take into account the contribution to the relic transverse size due to the projection of the shock-surface on the plane of the sky.

We selected three well studied radio relics in the clusters A 521, CIZA J2242.8+5301 and 1RXS J0603.3+4214. These relics have been chosen primarily because they are almost seen edge-on and because the Mach number of the shock that is associated with these relics is measured by X-ray observations, thus allowing to break the degeneracy between magnetic field and downstream velocity in the method. For the first two clusters, our method is consistent with a pure radiative aging model allowing us to derive constraints on the relics magnetic field strength. In the case of 1RXS J0603.3+4214 we find that particle life-times are consistent with a pure radiative aging model under some conditions, however we also collect evidences for downstream particle re-acceleration in the relic W-region and for a magnetic field decaying downstream in its E-region.

Our estimates of the magnetic field strength in the relics in A 521 and CIZA J2242.8+5301 provide unique information on the field properties in cluster outskirts. The constraints derived for these relics, together with the lower limits to the magnetic field that we derived from the lack of inverse Compton X-ray emission from the sources, have been combined with the constraints from Faraday rotation studies of the Coma cluster. Overall results suggest that the spatial profile of the magnetic field energy density is broader than that of the thermal gas, implying that the $\varepsilon_{th}/\varepsilon_B$ ratio decreases with cluster radius. Alternatively, radio relics could trace dynamically active regions where the magnetic field strength is biased high with respect to the average value in the cluster volume.

Sommario

I relitti radio sono emissioni diffuse di sincrotrone che si trovano generalmente nelle periferie degli ammassi di galassie in stato di *merger*. Lo scenario comunemente accettato per l'origine di queste sorgenti prevede che i relitti siano dei traccianti delle gigantesche onde d'urto che attraversano l'*intra-cluster medium* dove le particelle possono venire accelerate. La connessione tra i relitti e gli *shock* è supportata da diverse evidenze osservative, quali la morfologia inarcata dei relitti, il loro alto livello di polarizzazione e la corrispondenza spaziale con onde d'urto rilevate in banda X.

Markevitch et al. (2005) proposero un metodo per derivare l'intensità del campo magnetico nei relitti sotto l'assunzione che le particelle siano accelerate al fronte dell'onda d'urto per poi perdere energia mentre sono trasportate nella regione *downstream*. La misura della larghezza del relitto a diverse radio-frequenze permette di derivare delle stime combinate sulla velocità cui le particelle vengono trasportate downstream e sul campo magnetico della regione, il quale determina l'*aging* delle particelle. Questo è il punto di partenza del nostro lavoro da cui si è sviluppato il nostro metodo per stimare il campo magnetico nei relitti. Abbiamo considerato tre modelli di aging delle particelle da combinare con un modello geometrico che considera il contributo alla larghezza osservata del relitto dovuto alla proiezione della superficie dello shock sul piano del cielo.

Abbiamo selezionato un campione di tre relitti radio già molto studiati in letteratura, collocati negli ammassi di galassie A 521, CIZA J2242.8+5301 e 1RXS J0603.3+4214. Questi sono stati scelti in quanto i relitti sono osservati quasi *edge-on* e presentano una stima del numero di Mach dello shock derivante dall'analisi X. Questo permetterà di risolvere la degenerazione tra il campo magnetico e la velocità downstream nel nostro metodo. Per i primi due ammassi la nostra analisi è consistente con un modello di aging degli elettroni puramente radiativo che ci ha permesso di dare delle stime sull'intensità del campo magnetico della regione. Il caso di 1RXS J0603.3+4214 è anch'esso consistente con un modello di aging radiativo sotto alcune condizioni. Tuttavia, questo relitto potrebbe presentare uno scenario più complesso in quanto nella regione downstream abbiamo trovato evidenze di ri-accelerazione delle particelle nella parte W del relitto e di un possibile decadimento del campo magnetico nella sua parte E.

Le nostre stime sul campo magnetico nei relitti di A 521 e CIZA J2242.8+5301 danno informazioni uniche sulle proprietà del campo nelle periferie degli ammassi. Abbiamo combinato le nostre misure con i limiti inferiori all'intensità del campo magnetico derivanti dall'assenza di emissione X di Compton inverso da parte dei relitti. Questi sono stati confrontati con i risultati ottenuti dagli studi della rotazione di Faraday sull'ammassa di Coma. Dal confronto emerge che la distribuzione spaziale della densità di energia del campo magnetico sia più estesa rispetto a quella del gas termico, implicando dunque una diminuzione del rapporto $\varepsilon_{th}/\varepsilon_B$ con l'aumentare della distanza dal centro dell'ammasso. In alternativa, i nostri risultati potrebbero indicare che i relitti radio si collochino in regioni dinamicamente attive degli ammassi, dove il campo magnetico è sistematicamente più alto rispetto al suo valore medio.

Contents

List of acronyms **v**

Commonly used symbols **vii**

Introduction **xi**

1 Galaxy clusters **1**

1.1 Cluster of galaxies components 1

1.1.1 Galaxies 2

1.1.2 Intra-cluster medium 4

1.1.3 Dark matter 7

1.2 Mass estimates 7

1.3 Galaxy clusters as cosmological tools 9

1.3.1 Clusters formation 11

1.3.2 The Sunyaev-Zel'dovich effect 13

2 Non-thermal emission from galaxy clusters **15**

2.1 Radio relics 15

2.1.1 Origin of radio relics 17

2.2 Radio halos 20

2.2.1 Origin of radio halos 21

2.3 Radio mini-halos . . . 23
2.3.1 Origin of radio mini-halos . . . 24
2.4 Radio filaments . . . 25
2.5 Hard X-ray emission . . . 27

3 Magnetic fields in the ICM 29
3.1 Faraday rotation effect . . . 29
3.2 Inverse Compton emission . . . 32
3.3 Equipartition condition . . . 34
3.4 Cold fronts . . . 36
3.5 Radio relic emission . . . 38
3.6 Origin and amplification of cluster magnetic fields . . . 39

4 Constraining magnetic fields in radio relics 43
4.1 A geometric model . . . 43
4.2 X-ray analysis of the shock . . . 45
4.2.1 Limits to magnetic fields . . . 47
4.3 Particle life-time . . . 48
4.3.1 IC and spatially constant synchrotron emission . . . 48
4.3.2 Re-acceleration scenario . . . 49
4.3.3 Decaying magnetic field . . . 49

5 Relic sample 53
5.1 Abell 521 . . . 54
5.1.1 X-ray analysis . . . 54
5.1.2 Radio analysis . . . 56
5.2 CIZA J2242.8+5301 . . . 60
5.2.1 X-ray analysis . . . 60
5.2.2 Radio analysis . . . 62
5.3 1RXS J0603.3+4214 . . . 66

5.3.1 X-ray analysis 66
5.3.2 Radio analysis 68
5.4 Magnetic field estimates 72
5.4.1 A 521 73
5.4.2 CIZA J2442 75
5.4.3 1RXS J0603 77

6 Discussion **81**
6.1 Overall results 81
6.2 Magnetic field distribution 82
6.2.1 The role of numerical simulations 83
6.2.2 Constraints on thermal and magnetic field energy density ratio . 84
6.3 Limitations 87
6.4 The “Toothbrush” case 88

Conclusions **91**

A Mock radio relics **95**

Bibliography **101**

List of acronyms

2dFGRS	Two-degree-Field Galaxy Redshift Survey
2MASS	Two-Micron All-Sky Survey
AGN	Active Galactic Nucleus
AIPS	Astronomical Image Processing System
AMI	Arcminute Microkelvin Imager
ASCA	Advanced Satellite for Cosmology and Astrophysics
BB	Black Body
BCG	Brightest Cluster Galaxy
CDM	Cold Dark Matter
CfA	Center for Astrophysics
CIZA	Cluster In the Zone of Avoidance
CLASH	Cluster Lensing And Supernova survey with Hubble
CMB	Cosmic Microwave Background
DM	Dark Matter
DSA	Diffusive Shock Acceleration
ESA	European Space Agency
ETG	Early-Type Galaxy
FWHM	Full-Width at Half-Maximum
GC	Galaxy Cluster
GLASS	Grism Lens-Amplified Survey from Space
GMRT	Giant Metrewave Radio Telescope

HPBW	Half-Power Beam Width
HXR	Hard X-Ray
IC	Inverse Compton
ICM	Intra-Cluster Medium
ICL	Intra-Cluster Light
IGM	InterGalactic Medium
INTEGRAL	INTErnational Gamma-Ray Astrophysics Laboratory
IR	InfraRed
ISM	InterStellar Medium
LOFAR	LOw Frequency ARray
LS	Last Scattering
MACS	MAssive Cluster Survey
MHD	Magneto-Hydro Dynamics
NFW	Navarro-Frenk-White
NGC	New General Catalogue
NRAO	National Radio Astronomy Observatory
RM	Rotation Measure
ROSAT	ROentgen SATellite
RXS	Rosat X-ray Source
RXTE	Rossi X-ray Timing Explorer
SDSS	Sloan Digital Sky Survey
SFG	Star Forming Galaxy
SKA	Square Kilometre Array
SNR	SuperNova Remnant
SZ	Sunyaev Zel'dovich
USSRH	Ultra Steep Spectrum Radio Halo
VLA	Very Large Array
WSRT	Westerbork Synthesis Radio Telescope
XMM	X-ray Multi-Mirror mission
ZwCl	Zwicky Cluster

Commonly used symbols

α	Spectral index of the synchrotron radiation
ε_ν	Emissivity
ε_B	Magnetic field energy density
ε_{th}	Thermal energy density
Γ	Adiabatic index
γ	Lorentz factor
λ	Radiation wavelength
$\Lambda(T)$	Cooling function
$\mathcal{C}$	Compression factor
$\mathcal{M}$	Mach number
μ	Mean molecular mass
ν	Radiation frequency
Ω_Λ	Dark energy density of the Universe
Ω_m	Matter density of the Universe
τ_ν	Life-time of particle emitting at frequency ν
B	Magnetic field
B_{CMB}	Equivalent magnetic field strength of the CMB
B_{IC}	IC derived magnetic field
c	Speed of light
c_s	Speed of sound
E_e	Electron energy

G	Gravitational constant
h	Planck constant
H_0	Hubble constant
I_ν	Specific intensity
k_B	Boltzmann constant
L_X	X-ray luminosity
$M_\odot$	Solar mass
m_e	Electron mass
m_p	Proton mass
n_e	Electron density
p	Pressure
T_d	Downstream temperature
T_e	Electron temperature
t_H	Hubble time
T_u	Upstream temperature
V_d	Downstream velocity
z	Redshift

Introduction

GALAXY CLUSTERS (GC) are the most massive gravitationally bound systems in the Universe. They represent the last step in the hierarchical structure formation process where dark matter, which accounts for about 80% of cluster mass, is accumulated on Mpc-scales and shapes deep potential wells. First studies of GCs were carried out in the optical band by observing cluster galaxies. Thousands of galaxies are contained in clusters however they constitute only about 5% of cluster mass. About $\sim 75\%$ of the baryon mass indeed resides in the intra-cluster medium (ICM), a hot and tenuous medium which permeates the whole cluster volume. Its thermal bremsstrahlung emission in the X-rays makes clusters visible in the X-rays and plays an important role in the understanding of cluster physics.

In the recent years, radio observations revealed that a fraction of GCs produce synchrotron emission diffused on clusters scale. The discovery of radio sources not associated with any individual galaxy proves the presence of non-thermal components, such as relativistic particles and magnetic fields, mixed with the thermal ICM. According to their morphology and location in the cluster, cluster-scale radio sources have been classified as radio relic, radio halos and radio mini-halos.

Relics are elongated and arc-shaped synchrotron sources located in the peripheries of dynamically disturbed clusters. They are generally considered as tracers of shock waves generated during cluster-cluster merger events. The current leading scenario for their origin is based on diffusive shock acceleration theory, although several aspects of their formation mechanism are still unclear. The connection between radio relics and shocks is supported by several observational facts, including the coincidence between relics and shocks identified in the X-rays.

Halos and mini-halos are roundish radio sources located in the cluster central regions. The two classes differ in size and in the dynamical properties of the hosting clusters, with giant halos associated with merging systems and mini-halos with relaxed, cool-core, clusters.

Diffuse synchrotron sources in GCs prove the existence of magnetic fields and relativistic particles in the ICM spread on spatial scales that are comparable to the cluster size. So far, cluster magnetic field properties have mainly been gathered from Faraday rotation studies of polarized sources in or behind GCs. Faraday rotation reveals magnetic field strengths of the order of few μG in cluster cores and suggests that field decreases with cluster radius. Radio relics are unique probes of the properties of magnetic fields in the outskirts of GCs. In this Thesis we aim to extend our knowledge of

the field intensity at large distances from cluster centers using radio relics.

Under the assumption that particles are accelerated at the shock front and age downstream, the the thickness of the relic observed at a given frequency, Φ_ν, depends on the life-time of the emitting particles, τ_ν, and on the downstream velocity, V_d, hence $\Phi_\nu = V_d \tau_\nu$. Since the downstream velocity can be inferred from X-ray shock analysis, the measurement of the relic transverse size at different frequencies leads to constrain particle aging, hence the magnetic field of the emitting region.
The goal of the Thesis is to adopt this method to derive magnetic fields in the region of radio relics. Limits on the magnetic fields in radio relics can also be inferred from the non-detection of inverse Compton emission from these sources. These limits will be combined with the constraints obtained from the analysis of the thickness of relics.

The spatial profile of the magnetic field in GCs is still poorly known. In this respect constraints on magnetic fields at the distance of radio relics are expected to provide interesting insights. For this reason, we will also compare our results with the magnetic field profile obtained for the Coma cluster with Faraday rotation measurements.

This Thesis is organized in the following structure:

- In **Chapter 1** an introduction on GC general properties is presented. The main properties of the cluster galaxies, ICM emission and dark matter and are discussed. Methods for the determination of cluster mass and the process of formation and evolution of GCs are given.

- In **Chapter 2** an overview on non-thermal processes in GCs is presented. Observational properties of radio relics, halos, mini-halos and of radio filaments are presented. A brief discussion on the origin of these sources is also provided.

- In **Chapter 3** the methods for constraining magnetic fields in GCs are discussed together with the origin of magnetic fields.

- In **Chapter 4** we present our method to constrain magnetic field strengths in radio relics. We discuss three relevant scenarios of evolution of magnetic field and relativistic electrons downstream.

- In **Chapter 5** we analyze three radio relics in the clusters Abell 521, CIZA J2242.8+5301 and 1RXS J0603.3+4214 and report our results obtained for the magnetic field properties in these relics.

- In **Chapter 6** we combine our results with current constraints obtained for the spatial profile of the magnetic field in the Coma cluster. In this Chapter and in **Appendix A** we also discuss the limitations of our method.

- In the **Conclusions** an overview of this Thesis is presented. We highlight the main results and give some prospects for future studies on magnetic field in GCs.

Chapter 1

Galaxy clusters

CLUSTERS OF GALAXIES represent extraordinary laboratories in different research fields of modern astrophysics. These objects contain from hundreds to thousands of galaxies which are gravitationally bound in a deep potential well. Although galaxies are historically the first component that has been studied in galaxy clusters (GC), they represent the smallest part in term of their mass.

The largest cluster can reach mass up to $10^{15}\,M_{\odot}$ within a region of size up to few Mpc. The observable baryons in GCs can be in the form of *galaxies*, which represent about 5% of the mass of the cluster, or in the form of *intra-cluster medium* (ICM), a hot and low density thermal plasma permeating the cluster volume, which typically represent $15-20\%$ of the total mass. The largest part of the mass of GCs is in the form of *dark matter* (DM) which exhibits itself only through dynamical effects and gravitational lensing.

According to the current standard cosmological model ΛCDM (where Λ refers to a cosmological constant and CDM to *cold dark matter*), cosmic structures are built by a hierarchical formation process through the whole life of the Universe. Although the Universe expansion (the so-called Hubble flow) is in competition with structure formation, once gravity exceeds the contrast against the Hubble flow the process of growing matter is self-sustained and ends in the formation of more and more massive objects. For this reason, GCs are the most bound systems of such a "*bottom-up*" scenario and then it is likely to observe them at low redshifts. The mergers between clusters of galaxies are the most energetic phenomena in the Universe, where the dissipated energy can be as large as 10^{64} erg in a crossing life-time ($\sim$ Gyr).

1.1 Cluster of galaxies components

In order to have a more complete view of the components of GCs, multi-wavelength studies are required. Starting from radio frequencies to the X-ray band, clusters reveal themselves in various ways. Optical and IR observations are suitable for the analysis of the baryons which are in the form of stars in galaxies; X-ray and, more recently, radio observations are instead useful to study the tenuous medium which permeates the cluster environment. Moreover, relevant part of the cluster mass is constituted by non-baryonic matter that can not be directly observed but inferred studying the dynamics of GCs.

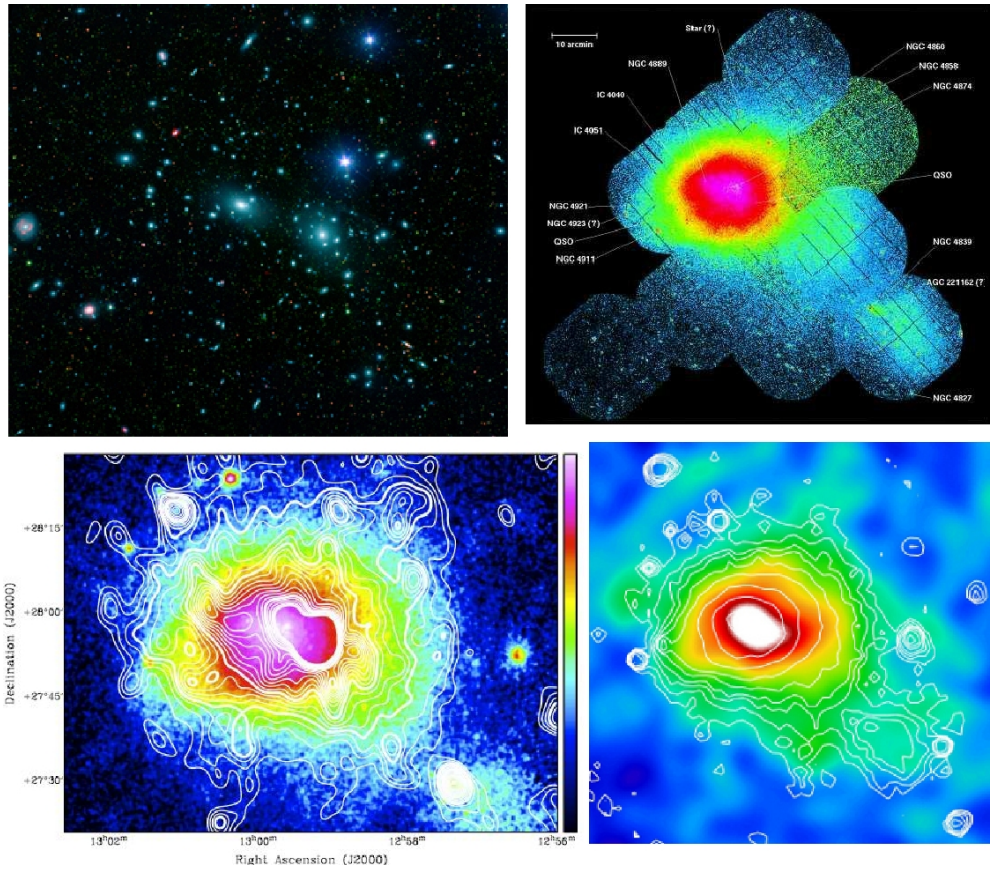

Figure 1.1: Multi-frequency view of the Coma cluster. *Top left*: optical emission of the cluster galaxies (Credit: SDSS). *Top right*: X-ray thermal emission of the ICM (Briel et al. 2001). *Bottom left*: the synchrotron diffuse radio emission at 352 MHz (contours) overlaid on the thermal X-rays (colors) (Brown & Rudnick 2011). *Bottom right*: overlay between thermal SZ signal (colors) and X-rays (contours) (Planck Collaboration 2011).

1.1.1 Galaxies

Because of their number and their optical emission, galaxies were the first GC component that has been investigated (Abell 1958). Starting from the typical value of their dispersion velocity, that is $\sigma_v \sim 1000\,\mathrm{km\,s^{-1}}$, and a cluster size, that is $R \sim 1\,\mathrm{Mpc}$, one can immediately infer the crossing time for a cluster

$$t_{cr} = \frac{R}{\sigma_v}$$

which is $\sim 1\,\mathrm{Gyr}$ and so significantly shorter than a Hubble time ($t_H \sim 13.7\,\mathrm{Gyr}$). This entails that GCs had enough time to dynamically relax.

Since the first investigations, it was clear that galaxies in cluster are different with respect to the ones of the field (see Fig. 1.2). In fact, GCs prevalently host early-type galaxies (ETG) and no star-forming galaxies (SFG) at all (see e.g. Abell 1965). Moreover, the few spiral galaxies detected in GCs have different properties with respect to the ones in the field (e.g. HI-deficiency). Such a distinctive galaxy population indicates that the interplay between cluster galaxies and the ICM has an impact on the properties of the interstellar medium (ISM).

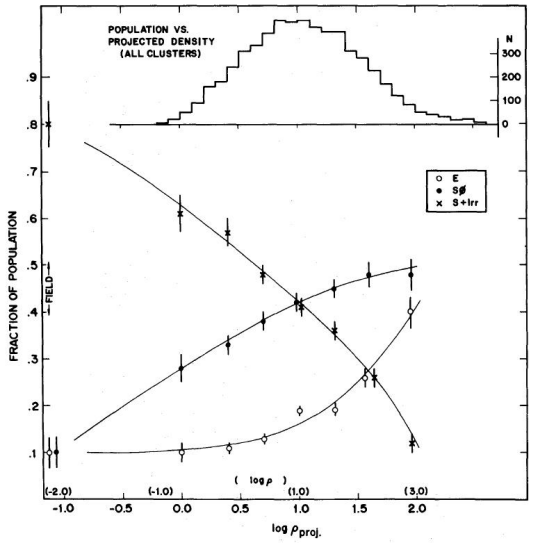

Figure 1.2: The fraction of elliptical (E), lenticular (S0), and spiral+irregular (S+I) galaxies as a function of the log of the projected density, in galaxies Mpc^{-2}, for a sample of cluster galaxies and for the field. The upper histogram shows the number distribution of the galaxies over the bins of projected density (Dressler 1980).

Over the years, theoretical studies on the dynamical processes that can modify the ISM were performed and some of these have been revised to justify the lack of gas in cluster spirals, such as collision between galaxies (Spitzer & Baade 1951), ram pressure ablation (Gunn & Gott 1972), gas stripping (Tarter 1975; Kritsuk 1983) and evaporation of the ISM (Cowie & Songaila 1977). The presence of the most gas deficient galaxies in the center of relaxed clusters (e.g. Giovanelli & Haynes 1985) seems to indicate that some of these processes (or a combination of them) are more relevant in the denser environments of GCs.

In the special environment of GCs, it is possible to find some kinds of galaxies that are not detected elsewhere. The most massive galaxies in the Universe are located in the cluster cores and are generally indicated as *brightest cluster galaxies* (BCG). These are characterized by properties that reflect the unique conditions that led their formation.

Although similar in colors and morphologies to ETGs, BCGs (e.g. cD galaxies) reveal some remarkable features (De Lucia & Blaizot 2007, for a review), like some blue stars (hence ongoing star formation) (Crawford et al. 1999), very extended low-surface brightness halos (Oemler 1976), multiple nuclei (Merritt 1984) and the prevalence of radio-loud *active galactic nuclei* (AGN) with respect to other galaxies of the same stellar mass (Best et al. 2007). Most of their properties can be explained assuming that BCGs are formed by the merger of many of the more luminous galaxies within the clusters core, in a process known as *galactic cannibalism* (Ostriker & Hausman 1977). However, other processes have to be considered to correctly describe the whole properties of such galaxies, like ICM dynamics and close encounters between the objects. The latter are especially needed to reproduce the extended cD envelopes (Gallagher & Ostriker 1972) that might be responsible of the intra-cluster light (ICL); that is the diffuse optical light which permeates the denser region of GCs due to stars being stripped from the central galaxies (or, eventually, from smaller galaxies crossing the central region in their motion).

1.1.2 Intra-cluster medium

The majority of the baryonic matter ($\sim 75\%$) in clusters is in the form of gas permeating the ICM. Its physical properties are those typical for an astrophysical hot plasma, like very low density ($n_e \sim 10^{-3} - 10^{-4}\,\mathrm{cm}^{-3}$) and high temperature ($T \sim 2\times10^7 - 10^8\,\mathrm{K}$) which produces thermal bremsstrahlung emission in the X-rays. The bremsstrahlung emissivity at a given frequency ν of an ion of charge Z in a plasma with an electron temperature T_e is

$$\varepsilon_\nu \propto Z^2 n_e n_i g_{ff}(Z,T_e,\nu) T_e^{-1/2} \exp\left(-h\nu/k_B T_e\right) \tag{1.1}$$

where g_{ff} is the Gaunt factor which accounts for quantum mechanics effects. The sharp exponential cutoff of continuum can lead to the determination of ICM temperature, whose typical values inhibit thermal emission above few $\times 10\,\mathrm{keV}$. Since GCs are very luminous in the X-ray band ($L_X \sim 10^{45}\,\mathrm{erg\,s^{-1}}$), many catalogs were made based on their high-energy emission. The X-ray selection still is one of the easier ways to search for clusters (e.g. Rosati et al. 1998).

Clusters of galaxies appear as diffuse X-ray sources in the sky. A property that can be investigated through X-ray imaging is the distribution of the ICM gas. Assuming spherical symmetry of the gas, the surface brightness at frequency ν at a projected radius b is

$$\Sigma_\nu(b) = 2\int_{b^2}^{\infty} \frac{\varepsilon_\nu(r)\,dr^2}{\sqrt{r^2-b^2}} \tag{1.2}$$

where $\varepsilon_\nu = n_i n_e \Lambda(T)$ is the emissivity, n_i and n_e are ion and electron number densities and $\Lambda(T)$ is the cooling function. Eq. (1.2) can be Abel inverted

$$\varepsilon_\nu = -\frac{1}{2\pi r}\frac{d}{dr}\int_{b^2}^{\infty} \frac{\Sigma_\nu(b)\,db^2}{\sqrt{b^2-r^2}}$$

and since $n_{gas} = n_i + n_e$, the gas distribution can be finally obtained (e.g. Sarazin 1986).

Cavaliere & Fusco-Femiano (1976, 1978) proposed a method to estimate the spatial distribution of the ICM under the simple assumption that the distributions of gas (with mean molecular mass μ) ρ_{gas} and of galaxies ρ_{gal} are both isothermal and in equilibrium in the cluster gravitational potential Φ

$$\frac{d\ln\rho_{gas}}{dr} = -\frac{\mu m_p}{k_B T_{gas}}\frac{d\Phi(r)}{dr}$$

$$\frac{d\ln\rho_{gal}}{dr} = -\frac{1}{\sigma_{gal}^2}\frac{d\Phi(r)}{dr}$$

where the galaxy velocity dispersion σ_{gal}^2 is assumed isotropic. The above equations lead to

$$\frac{d\ln\rho_{gas}}{dr} = \frac{\mu m_p \sigma_r^2}{k_B T_{gas}}\frac{d\ln\rho_{gal}}{dr} \tag{1.3}$$

where the ratio between the gas temperature T_{gas} and the equivalent galaxy temperature $T_{gal} = \mu m_p \sigma_r^2/k_B$ emerges, usually indicated as

$$\beta \equiv \frac{\mu m_p \sigma_r^2}{k_B T_{gas}}$$

hence the name β-*model*. Eq. (1.3) can be integrated assuming a King approximated model (King 1962) for the galaxy density profile with a core radius r_c (it is a measurement of the size of the central core)

$$\rho_{gal}(r) = \rho_{gal}(0)\left[1+\left(\frac{r}{r_c}\right)^2\right]^{-\frac{3}{2}}$$

so that the gas distribution will become

$$\rho_{gas}(r) = \rho_{gas}(0)\left[1+\left(\frac{r}{r_c}\right)^2\right]^{-\frac{3\beta}{2}} . \tag{1.4}$$

Observations suggest that the best fit values for β-models are $\beta_{\rm fit} \sim 2/3$, thus for $r \gg r_c$ the density of galaxies is $\rho_{gal} \propto r^{-3}$ while the gas distribution is more extended, with $\rho_{gas} \propto r^{-2}$. However, it has to be noticed that the determination of T_{gas} through X-ray spectral measurements and optical investigations of the velocity dispersion σ^2_{gal} claim a discrepancy between the β inferred by observations and the one from the fits, indicating $\beta_{\rm spec} \sim 2\beta_{\rm fit}$ (Mushotzky 1984). Further theoretical studies (Bahcall & Lubin 1994) showed that β-discrepancy could be avoided if $\rho_{gal} \propto r^{-2.4}$, some assumptions on the original model (Cavaliere & Fusco-Femiano 1976, 1978) were indeed oversimplified.

In addition to imaging studies, information about the ICM can be gathered from X-ray spectra which are characterized by a continuum from thermal bremsstrahlung emission and lines from highly ionized species. In the spectra, the number and the kind of lines are strongly dependent of the chemical species ionization degree and and of the medium temperature, becoming less relevant at high temperatures, where continuum emission is the most effective process. Spectral analysis reveals the presence of highly ionized metals, like Fe, C, O, Ne, Si, S and more, which can lead useful information about cluster abundance through line-to-continuum ratios. A typical estimate for the hot gas metallicity inferred from spectral analysis is a third of the solar value. Since such a value is too large to be of cosmological origin, it is likely that part of the primordial gas has been enriched by galactic winds of the cluster galaxies (e.g. De Lucia et al. 2004). Moreover, this feedback scenario is also supported by the fact that the high metallicity values observed in the inner region of GCs can be produced by the BCGs (De Grandi & Molendi 2001; De Grandi et al. 2004). The powerful AGNs detected in the center of GCs clearly demonstrate that they can distribute metals in the ICM through outflow activity (e.g. Ettori et al. 2013) and then spread them in the surroundings (Gaspari et al. 2011).

A natural reason of having a peaked density profile in the inner region is that the cooling time of the gas

$$t_{cool} = \frac{5}{2}\frac{k_B \rho_{gas} T_{gas}}{\mu m_p}\frac{1}{n_e n_i \Lambda(T)}$$

is shorter in the cluster center than in its outskirts. Fig. 1.3 shows that at small radii from the cluster center $t_{cool} < t_H$ and so radiative losses are important for the ICM evolution. For this reason, *cool-cores* are found only in dynamically relaxed clusters, in contrast to GCs which are not in a relaxed state, where external energetic phenomena (e.g. mergers) can remove such a higher density feature.

Due to radiative losses, gas loses pressure support in the center and must flow inward with a mass rate (Fabian 1994)

$$\dot{M}_{cool} = \frac{2}{5}\frac{\mu m_p}{kT_{gas}} L_{cool}$$

where L_{cool} denotes the X-ray luminosity associated with the cooling region. However, X-ray observations with *XMM-Newton* and *Chandra* satellites, found that the expected *cooling flow* rates were overestimated (see Peterson & Fabian 2006 for a review). This triggered the discussion on the phenomena that could contribute to slow down that natural process.

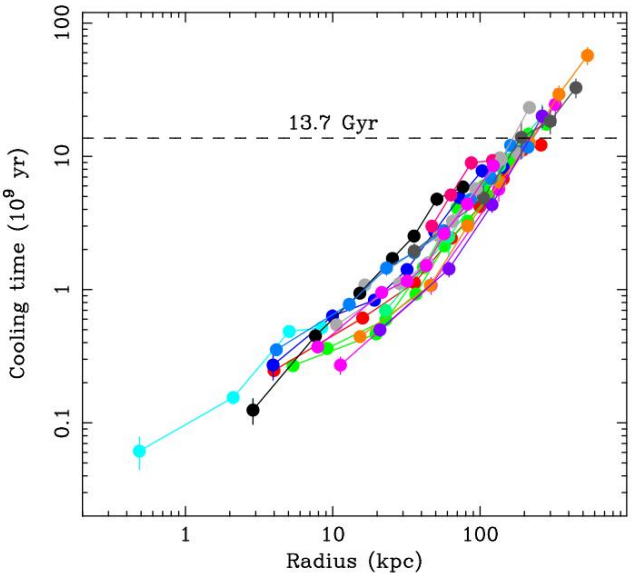

Figure 1.3: The cooling time as a function of radius for a sample of relaxed clusters (Peterson & Fabian 2006).

The most promising scenario to resolve the cooling flow problem is actually the *AGN feedback*. In fact, the huge amount of energy released by the powerful AGNs in cluster centers could provide heating and pressure support to the inflowing gas, slowing down the cooling. The interplay between the ICM and the non-thermal plasma ejected from the AGNs is well demonstrated by the detection of *X-ray cavities* and *radio bubbles* in the cluster volume (see e.g. McNamara & Nulsen 2007; Gitti et al. 2012 for reviews).

In the recent years, radio observations of GCs revealed the presence of non-thermal components in the ICM, such as magnetic fields and relativistic particles, in addition to the well studied thermal one. Non-thermal phenomena in GCs draw the attention of many researches due to the requirement of new physical mechanisms that may effect the largest scale structures of the Universe. Since these are the main topic of this Thesis, they will be broadly discussed in the next Chapter.

1.1.3 Dark matter

Different approaches in the investigation of the cluster mass (see the next Paragraph) led to a disconcerting result about the total mass of GCs. In fact, their high mass-to-light ratio values ($M/L \gg 100$) imply the presence of a large amount (up to 80% of the cluster mass) of non-baryonic matter that can not be detected in any electromagnetic band, hence its name: dark matter (DM).

In the standard scenario of structure formation, DM halos hierarchically form through gravitational collapse starting from small density fluctuations that merge themselves becoming more and more massive (i.e. the “merger trees") (Lacey & Cole 1993; Kauffmann et al. 1993). Navarro, Frenk, & White (1997) showed through numerical simulations that the equilibrium state of CDM halos is described by an analytic formula for the DM density profile, known as NFW profile,

$$\rho_{DM}(r) = \rho_{crit} \frac{\delta_c}{(r/r_s)(1+r/r_s)^2}$$

where r_s is a scale radius, δ_c is a characteristic (dimensionless) density and $\rho_{crit} = 3H^2/8\pi G$ is the critical density for Universe closure (H is the Hubble constant). Although different models to fit DM profiles were proposed (Einasto 1965; Begeman et al. 1991; Burkert 1995), NFW profile is one the most used shapes for CDM halos and seems to be a universal profile since it is independent of the halo mass and of the adopted cosmological model.

1.2 Mass estimates

Determining the mass of GCs is the first step in the understanding of the physics of the formation and evolution of large scale structures; however, the mass estimation represent a complicated issue. With simple assumptions and the use of known cluster physics, mass estimates can be achieved with different approaches.

Virial theorem

In the case that a cluster is in dynamical equilibrium, the simplest way to have a first estimate of its total mass M_{tot} is based on the virial theorem

$$2T + U = 0$$

and it uses the fact that cluster galaxies sample the cluster potential well. In the above equation, T is the kinetic energy

$$T = \frac{1}{2} M_{tot} \sigma_V^2$$

and U is the gravitational potential energy

$$U = -\frac{GM_{tot}^2}{r_g}$$

of the cluster. The quantities σ_V and r_g refer to the virial velocity dispersion and the gravitational radius, respectively. The latter can be evaluated assuming that the galaxy distribution traces the mass distribution

$$r_g = 2\left(\sum_i M_i\right)^2 \left(\sum_{i\neq j} \frac{M_i M_j}{r_{ij}}\right)^{-1}$$

where M_i is the mass of the i-th galaxy and r_{ij} is the galaxy-galaxy separation. In term of the projected galaxy-galaxy separation R_{ij}, the gravitational radius becomes $r_g = (\pi/2)R_g$ (Limber & Mathews 1960), where

$$R_g = 2\left(\sum_i M_i\right)^2 \left(\sum_{i\neq j} \frac{M_i M_j}{R_{ij}}\right)^{-1} .$$

With the assumptions of spherical symmetry and Gaussian velocity distribution, that is $\sigma_V^2 = 3\sigma_r^2$ (σ_r is the radial velocity dispersion of cluster galaxies), one can derive

$$M_{tot} = \frac{3 r_g \sigma_r^2}{G}$$

to obtain the mass of the cluster once r_g and σ_r are known.

This kind of approach is very simplified and is based on assumptions that are not completely justified (e.g. the virial equilibrium). However, it brought the first mass estimate for a GC, for the Coma cluster (Zwicky 1937), and evidenced a mass excess with respect that evaluable as the sum of the optical cluster components. In fact, the mass-to-light ratio revealed the presence of a "dark" component that dominates the cluster mass.

Hydrostatic equilibrium of gas

Another simple method to estimate the mass of a GC is based on measurements of the ICM. This method uses two assumptions that may not be completely satisfied: (i) the hydrostatic equilibrium of the ICM in the cluster gravitational potential Φ

$$\nabla p = -\rho_{gas} \nabla \Phi$$

and (ii) spherically symmetry, so that

$$\frac{dp}{dr} = -\rho_{gas}\frac{d\Phi}{dr} = -\rho_{gas}\frac{GM(r)}{r^2} .$$

Considering the state equation of a perfect gas, the mass at a given radius r is

$$M(r) = -\frac{k_B T_{gas} r}{\mu m_p G}\left(\frac{d\ln \rho_{gas}}{d\ln r} + \frac{d\ln T_{gas}}{d\ln r}\right)$$

and it requires the knowledge of the temperature and gas density profiles. The former requires spectral analysis at different annuli, the latter can derived by assuming a β-model (Eq. 1.4) or, in the best cases, it can be estimated from deprojection analysis.

Gravitational lensing

As a consequence of being the most massive gravitational systems in the Universe, GCs are good environments to test the Theory of General Relativity. One of the most majestic effects that can be observed in GCs is light deflection due to the passage of radiation near massive objects. That is *gravitational lensing*.

Objects seen through a gravitational lens may appear distorted, with arc-shaped structures, or even fragmented in a number of individual images with identical spectral energy distribution but different shape and intensity. The study of such kinds of apparent "artifacts" can be used to infer the mass responsible for the lens.

Despite the two methods previously illustrated to estimate GC mass, gravitational lensing is not easy to deal with, however it may give the best constraints on mass determination.

Generally, gravitational lensing can be distinguished in *strong lensing* events and in *weak lensing* events, which differ with respect to the source-lens-observer geometry and then to the importance of the phenomenon. Both of them provide useful information about the GC mass and its distribution, that is: (i) baryons are not sufficient to explain the total mass of clusters, (ii) the presence of thin arcs indicates steep mass profiles and (iii) complex distorted geometries suggest that mass is not symmetrically arranged and substructures may exist.

The detection of gravitationally lensed sources is not easy. For this reason, although weighting GCs through relativistic effects was proposed in Zwicky (1937), the first discovery of a gravitational lens due to a GC was reported several years later (Soucail et al. 1987).

Nowadays there are several projects aimed to search lensed sources around GCs (e.g. CLASH, GLASS, Frontier Fields) which are crucial to explore the deepest field ever recored in high-z astronomy. The technology which lays under the projects of the modern telescopes is precisely helped by the presence of "natural telescopes" due to gravitational lensing. Taking advantage from the significant distortions near GC fields, it is possible to search the most distant objects ever observed (e.g. Watson et al. 2015). Looking at the first galaxies which populated the young Universe is a fundamental step in the understanding of what was the starting point from which nowadays objects began their evolution.

1.3 Galaxy clusters as cosmological tools

Being the largest collapsed objects in the Universe, GCs are fundamental tools in the discrimination of cosmological models. Cosmic structures are formed by gravitational collapse starting from small density fluctuations. The existence of such density perturbations can be inferred from the temperature perturbations of the *cosmic microwave background* (CMB) map shown in Fig. 1.4. Once the collapse starts more and more matter is accumulated and that results in the formation of more massive objects.

The understanding of *how* and *when* GCs formed during the history of the Universe is one of the most successful ways to test cosmology; in fact, the number of GCs versus redshift is one of the proofs which models have to explain (see Fig. 1.5).

Clusters are the largest galaxy aggregations and for this reason they can be used like luminous-matter tracers. Furthermore, since they also contain a lot of non-baryonic

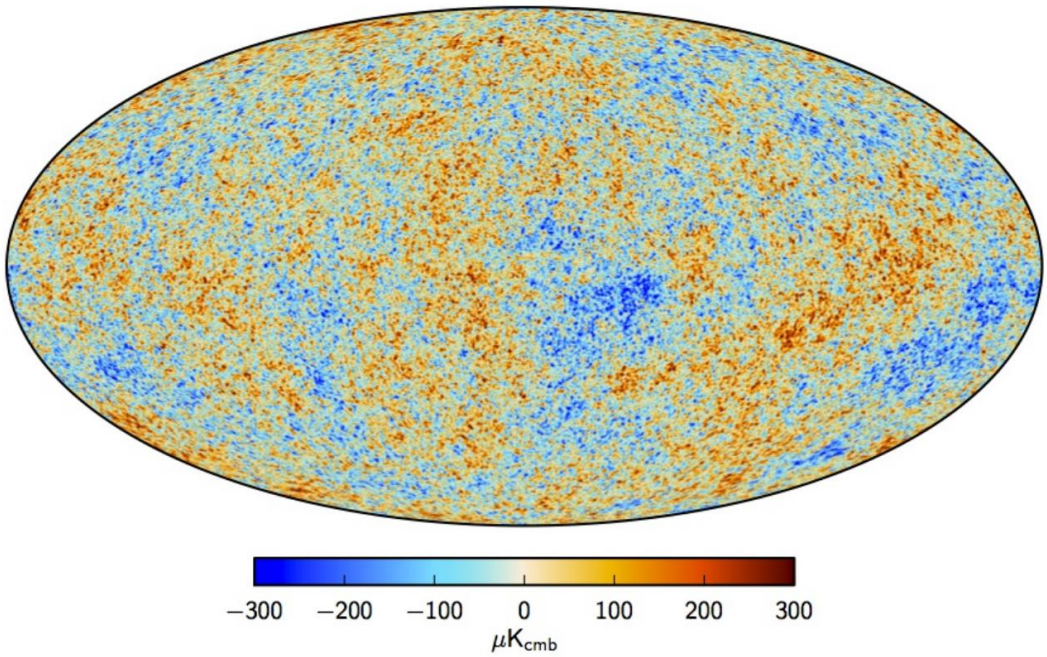

Figure 1.4: Temperature map of the CMB (Credit: ESA and the Planck Collaboration).

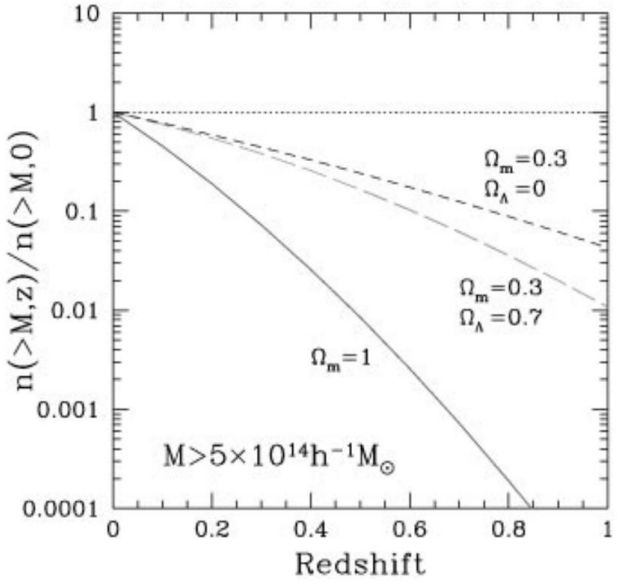

Figure 1.5: The sensitivity of the cluster mass function $n(>M,z)$ evolution for three different cosmological models: *solid line*, $\Omega_m = 1$; *short-dashed line*, $\Omega_m = 0.3$, $\Omega_\Lambda = 0.7$; *long-dashed line*, $\Omega_m = 0.3$, $\Omega_\Lambda = 0$ (Rosati et al. 2002).

matter, they are tools to (indirectly) infer the DM distribution in the Universe. For this purpose large field surveys have been made in the optical and near-IR band, such as 2dF Galaxy Redshift Survey (2dFGRS), Two Micron All-Sky Survey (2MASS), Sloan Digital Sky Survey (SDSS) and so on. The large amount of data achieved with these observations is essential to constrain clustering of galaxies in the Universe, which is a basic test to prove the reliability of cosmological simulations. An exemplar view of that is shown in Fig. 1.6.

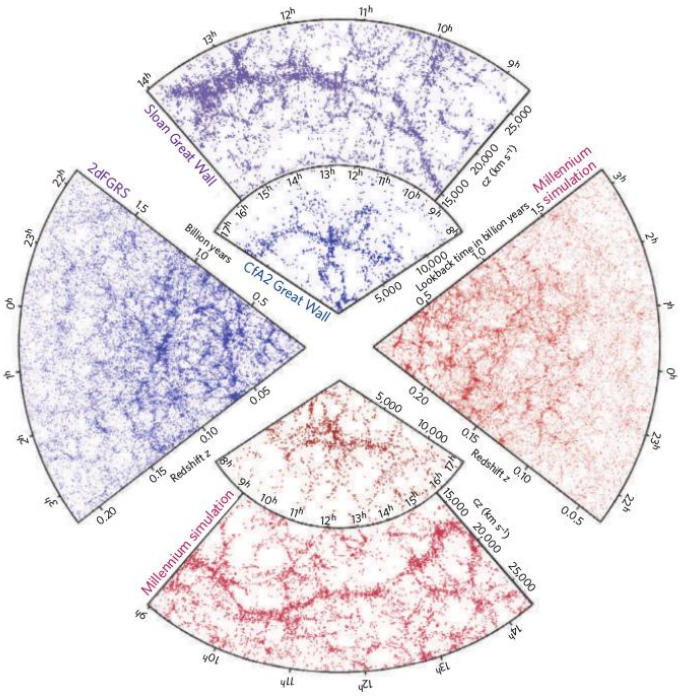

Figure 1.6: Comparison between the galaxy distribution obtained from spectroscopic redshift surveys (CfA2, SDSS, 2dFGRS) and from mock catalogs constructed from cosmological simulations (Millennium simulation, Springel et al. 2005) (Springel et al. 2006).

In this respect surveys must be deep because models are more and more different at higher and higher redshift, as shown in Fig. 1.5. For this reason, the cluster epoch of formation can be a powerful tool to determine which cosmological model has the best agreement with the data. Nowadays, the standard cosmological model is the ΛCDM model; the updated values of model parameters have been recently reported in Planck Collaboration (2015).

1.3.1 Clusters formation

The density fluctuations responsible of the formation of the first cosmic structures are believed to develop at the end of the inflation era (e.g. Mukhanov & Chibisov 1981), when any physical privileged scale did not exist. Theoreticians, therefore, choose a power-law to describe the initial density perturbation spectrum (as known as scale-free spectrum)

$$P_{in}(k) = Ak^s \tag{1.5}$$

where k is the a characteristic scale of the perturbation, A is the normalization of the spectrum (not predictable by any inflation model) and s is the spectral index of the power-law.

The first studies on gravitational collapse has been done in linear theory, i.e. that the density perturbations δ in the system are small $\delta \ll 1$. Nevertheless, observations prove the existence of objects that underwent the non-linear regime (e.g. GCs). It is thus necessary to deal with more complex physics.

Starting from the results provided by the linear theory it is possible to obtain useful non-linear scaling laws that describe the evolutionary properties of virialized systems that can be tested with observations and cosmological simulations.

In linear regime, a perturbation δ_i evolves in time in a self-similar way: $\delta_i \rightarrow \delta_i \delta_+(t)$ where $\delta_+(t)$ indicates the growing time dependent solution that does not depend on the scale k, i.e. all perturbations grow equally in every possible scale. Considering a filter function $\hat{W}(kR)$ that discriminates the contribution of $P(k)$ for different k and a co-moving scale R, the mass variance is

$$\sigma_M^2 = \frac{1}{(2\pi)^3} \int P(k) \hat{W}^2(kR)\, d^3r$$

which, adopting a scale-free spectrum (Eq. 1.5), becomes

$$\sigma_M^2 \propto \delta_+^2(t) k^{s+3}$$

and since $k \propto 1/R$ and the mass $M \propto R^3$, it eventually becomes

$$\sigma_M^2 \propto \delta_+^2(t) R^{-(s+3)} \propto \delta_+^2(t) M^{-\frac{s+3}{3}} .$$

The above equation sets the typical mass M_* collapsing at time t when non-linear regime is established, i.e. when $\delta \sim 1$ and so $\sigma_M^2 \propto \delta^2 \sim 1$. It can be easily derived

$$M_*(t) \propto \delta_+(t)^{\frac{6}{s+3}} \tag{1.6}$$

which solution depends of the chosen cosmological model leading the dependences of $\delta_+(t)$. Starting from Eq. (1.6) one can derive other scaling laws for the typical epoch t_* of formation of the structure with mass M_*, size R_*, density ρ_* and velocity dispersion σ_*^2. As a simple reference, for an Einstein-de Sitter Universe it is $\delta_+(t) \propto (1+z)^{-1}$ and the above mentioned quantities become

$$M_* \propto (1+z)^{-\frac{6}{s+3}} ,$$

$$R_* \propto M_*^{\frac{1}{3}} (1+z)^{-1} ,$$

$$\rho_* \propto (1+z)^3 ,$$

$$\langle \sigma_*^2 \rangle \propto M_*^{\frac{2}{3}} (1+z) .$$

Since GCs are the most non-linear structures in the Universe, these relations can be tested in GC samples. However, the above relations have been derived under the

assumption that gravity is the only force acting during collapse. Deviations from the expected laws are attributed to the presence of baryonic matter which enters in the formation process with effects which are not (well) understood jet (e.g. cooling, feedback). In this respect, numerical simulations are powerful tools to solve such discrepancies.

1.3.2 The Sunyaev-Zel'dovich effect

The CMB radiation is detected in all directions of the sky and it is interpreted as the echo of the Big Bang (Penzias & Wilson 1965; Dicke et al. 1965). It was produced around $z_{LS} \sim 1100$ when there was the last scattering (LS) between matter and radiation. These two components were in thermal equilibrium at the moment of LS and so the CMB has the shape of black body (BB) radiation with specific intensity

$$I_\nu = \frac{2h\nu^3}{c^2}\left[\exp\left(\frac{h\nu}{k_B T}\right) - 1\right]^{-1}. \tag{1.7}$$

During an adiabatic expansion of the Universe the form of the CMB spectrum (Eq. 1.7) remains the same but changes its temperature T, since the number of photons per unit frequency in the volume

$$N_\nu = \left[\exp\left(\frac{h\nu}{k_B T}\right) - 1\right]^{-1}$$

must be conserved (see e.g. Coles & Lucchin 2002). In fact, the expansion creates a variation of $\nu \propto (1+z)$ and, in order to conserve N_ν, T also varies as $(1+z)$. The CMB temperature then cools from its original value till the actual temperature of $T_{CMB} = 2.72548 \pm 0.00057\,\mathrm{K}$ (Fixsen 2009).

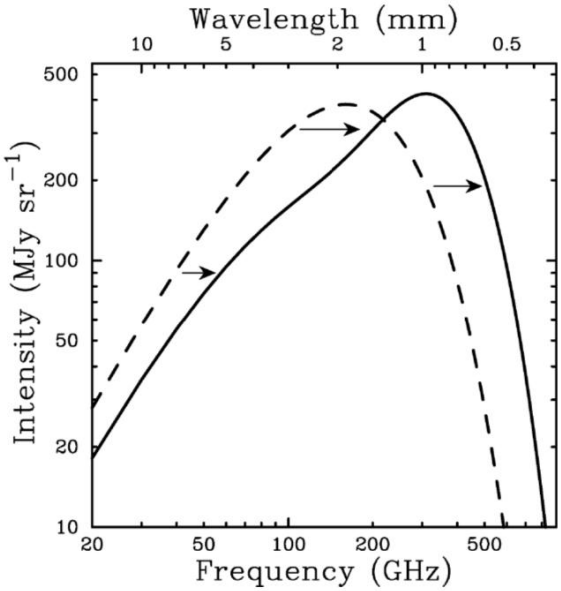

Figure 1.7: The CMB spectrum, undistorted (*dashed line*) and distorted by the SZ effect (*solid line*). To emphasize the effect, the SZ distortion shown is for a fictional cluster 1000 times more massive than a typical massive GC (Carlstrom et al. 2002).

The CMB photons travel the whole Universe and might encounter hot plasmas like the ICM in GCs. Due to the scattering between the cool CMB photons and the hot electrons ($T_e \sim 2\times10^7 - 10^8$ K) of the ICM, the former gain energy via Inverse Compton (IC) process. Its amplitude is proportional to the Comptonization parameter

$$y_e \propto \int n_e T_e \, dl$$

which is the optical depth of the Compton scattering and it depends on the electron density n_e and temperature T_e along the line-of-sight L. The CMB intensity changes due to the interaction between the ICM electrons and the photons of the CMB spectrum at dimensionless frequency $x_\nu = \frac{h\nu}{k_B T_{CMB}}$ as

$$\frac{\Delta I}{I_0} = f(x_\nu) y_e$$

where $I_0 = 2(k_B T_{CMB})^3/(hc)^2$ and the frequency dependence is given by

$$f(x_\nu) = \frac{x_\nu^4 e^{x_\nu}}{(e^{x_\nu}-1)^2}\left(x_\nu \frac{e^{x_\nu}+1}{e^{x_\nu}-1} - 4\right)(1+\delta(x_\nu, T_e))$$

where $\delta(x_\nu, T_e)$ is the relativistic correction to the frequency dependence (Carlstrom et al. 2002). This effect results in a distortion around 218 GHz in the BB shape of the CMB, as shown in Fig. 1.7.

This physical process, known as Sunyaev-Zel'dovich (SZ) effect (Sunyaev & Zeldovich 1972), was firstly verified several years ago (Pariiskii 1972) and now it represents one of the more fashionable tools to search GCs (e.g. with the *Planck* spacecraft). In fact, this effect is independent of the redshift of the (spatially resolved) source responsible for the photon up-scatter and it can be detected in maps like the one of *Planck* (see Fig. 1.8).

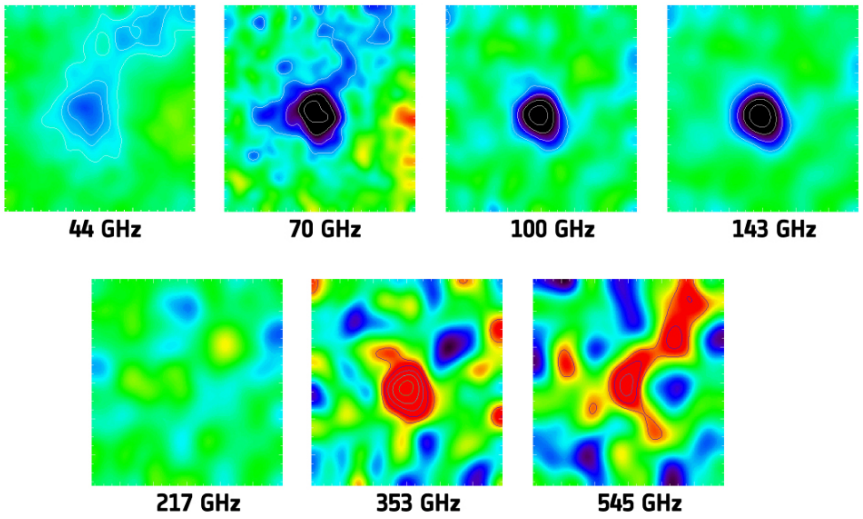

Figure 1.8: The SZ effect seen in the cluster A 2319. Images at various frequencies (see panels) show that the cluster appears as a decrement on the photon number for $\nu < 218$ GHz and as an increment above 218 GHz (Credit: ESA).

Chapter 2

Non-thermal emission from galaxy clusters

In the past decades, an increasing number of GCs showing the presence of diffuse radio emission not associated with any individual (radio) galaxy has been detected.

The radio spectra of such emissions are power-law like ($S_\nu \propto \nu^{-\alpha}$, where α is the spectral index), indicative of synchrotron emission demonstrating the presence of relativistic particles and magnetic fields. To understand the origin of these diffuse sources in GCs, it is then crucial to investigate (i) how particles are accelerated at relativistic energies in such environments and (ii) what are the proprieties of the magnetic field in the ICM.

The diffuse, extended (up to Mpc-scales), low surface brightness ($\sim \mu$Jy arcsec^{-2} at 1.4 GHz) radio sources in GCs are typically classified in three species. According to their location in the cluster, their radio properties, their morphology and their host cluster type (merging or cool-core), one might distinguish: *relics*, *halos* and *mini-halos*. Further diffuse radio emissions are expected from cosmic *filaments* but no clear detection has been found to date, since their elusive nature.

In the following, an overview of the known proprieties of radio relics is presented since they are the main astrophysical subjects of this Thesis. Other diffuse radio sources in GCs are also discussed (for reviews on non-thermal emission in GCs see Feretti et al. 2012; Brunetti & Jones 2014). At the end of the Chapter, a brief summary of non-thermal X-ray emission from GCs is also given.

2.1 Radio relics

Radio relics are diffuse synchrotron sources that are only found in merging systems and currently $\gtrsim 50$ of them are known. The classification of relics may be troublesome in some cases; the first step before providing more details on these sources is to define what *we* mean for radio relic in this work. Historically, relics have been divided into three groups (Kempner et al. 2004): *radio gischt*, *AGN relics* and *radio phoenices*. The first class is related to diffuse emission in the ICM while the other two are associated with a previous AGN activity. Attempts to more detailed classification have been made

in the last years (e.g. Giovannini & Feretti 2004; Feretti et al. 2012). In this Thesis we focus on the most relevant and spectacular class of radio relics, the so-called *giant radio relics*. The prototype source of this class is the relic 1253+275 detected in the Coma cluster (Giovannini et al. 1991), shown in Fig. 2.1. Relics are characterized by elongated morphologies, peripheral locations and significant linear polarization (typically up to 30%). They can reach linear extensions above the Mpc-scale and represent important probes of the magnetic field properties in the clusters outskirts, as they can be found at distances up to a large fraction of the cluster virial radius. Relics show quite steep spectra, with an average integrated value of $\alpha \sim 1.3$ (Feretti et al. 2012).

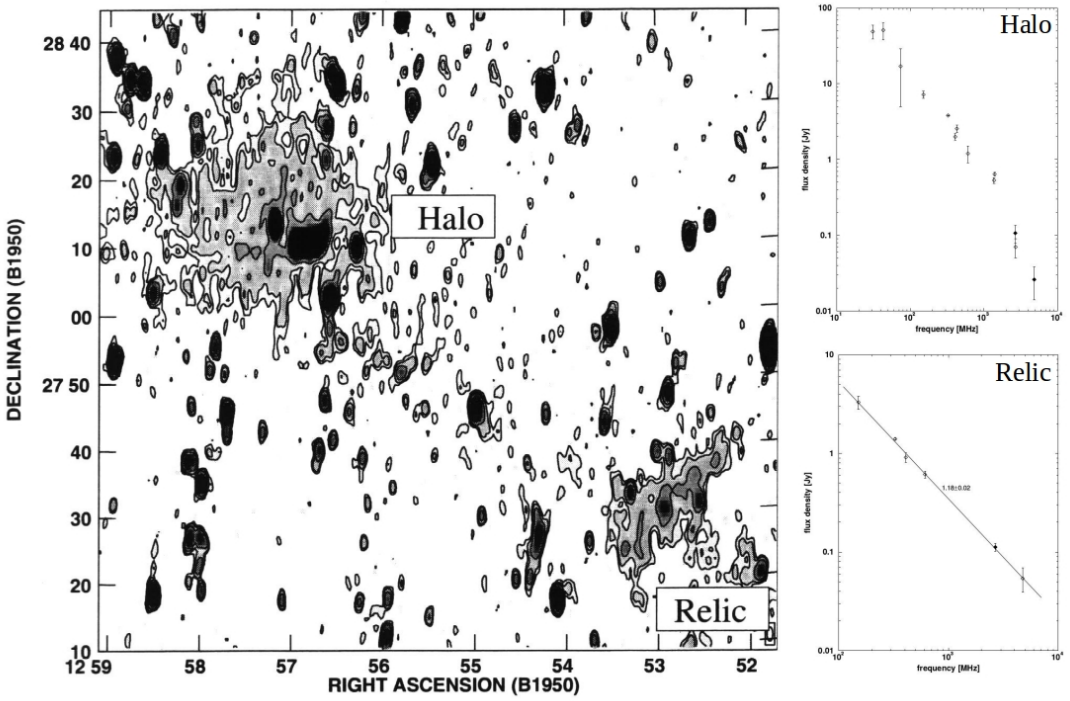

Figure 2.1: *WSRT* radio image of the Coma cluster at 326 MHz (resolution $55'' \times 125''$). The radio halo Coma C is at the cluster center, the radio relic 1253+275 is at the cluster periphery (Giovannini et al. 1993). Spectra for both sources are also reported (Thierbach et al. 2003).

The search of correlations between relics and host cluster properties are fundamental to unveil the origin of these objects. However, these studies are still affected by the poor source statistics and possible observational biases. A correlation between the radio power at 1.4 GHz and the X-ray cluster luminosity is well established (Feretti et al. 2012). More recently, de Gasperin et al. (2014) found that the radio luminosity of relics is a steep function of the cluster mass, suggesting that the magnetic field at the location of radio relics is rather uniform in all relics.

Some relics are spatially connected with other cluster diffuse sources through a low brightness bridge of radio emission (e.g. Coma cluster, Kim et al. 1989), or, in other cases, by more complex structures (e.g. A 754, Bacchi et al. 2003). The connection between peripheral (i.e. relic) and central (i.e. halo) emissions suggests that these sources share a common trigger mechanism that, as we will see, is imputable to cluster merger events.

2.1.1 Origin of radio relics

There is a broad consensus on the hypothesis that radio relics are connected with shocks (e.g. Brunetti & Jones 2014). Such a connection is highlighted by several observational results, as (i) the arc-shaped structures roughly perpendicular to the cluster center direction that many relics exhibit, (ii) their high level of polarization, (iii) their similarity with supernova remnants (SNR) (Fig. 2.2) and, in some cases, (iv) by the spatial correlation with X-ray discontinuities in the thermal gas (see Chapter 5). These properties provide the starting point for the theoretical understanding of radio relics.

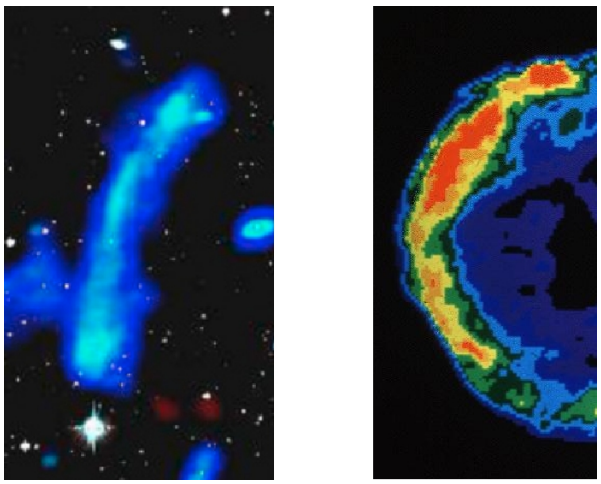

Figure 2.2: Morphology comparison between a radio relic and a SNR. *Left panel*: 323 MHz emission of the radio relic in the cluster of galaxies PLCKG287.0+32.9 (Bonafede et al. 2014). *Right panel*: 1.4 GHz emission from the SNR 3C 10 (Tycho) (Credit: NRAO).

In a number of cases, *double relics*, symmetric sources located on opposite sides, are detected. They are very important to unveil the origin of this class of radio sources. Numerical simulations of merging GCs (e.g. Roettiger et al. 1997) show that during such energetic events large-scale shocks and turbulence may arise (see Bykov et al. 2008 for a review). In the case of a merger between clusters with similar mass and small impact parameter, relics are expected to come in pairs and be located on opposite sides of the cluster along the axis merger. This is the case of the prototype double relic found in A 3667, shown in Fig. 2.3, where two almost symmetric relics have been detected on opposite sides of the host cluster (Rottgering et al. 1997). These are thought to trace diametrically outward traveling shocks coming from the center. Several other cases are known and $\gtrsim 10$ double relics have been detected so far. Multi-frequency observations and numerical simulations of these double relics seem to confirm the scenario for which double relics emerge from a head-on merger in the plane of the sky of two roughly equal mass clusters. It is then an indisputable fact that shocks play a fundamental role in the acceleration or re-acceleration of radio electrons generating relics, even though the details of the mechanism are still under debate (Brüggen et al. 2012; Brunetti & Jones 2014).

Particle acceleration at shocks is customarily described according to the *diffusive shock acceleration* (DSA) theory (Krymskii 1977; Bell 1978a,b; Drury 1983; Blandford & Eichler 1987; Jones & Ellison 1991; Malkov & Drury 2001). It is a Fermi I process where particles are scattered up and downstream the shock, gaining energy at

each reflection. In this respect, turbulence is a crucial ingredient in the DSA theory as it governs the scattering of particles across the shock surface. Turbulence also generates hydrodynamical instabilities that may play a role in the magnetic field amplification in the downstream region (e.g. Iapichino & Brüggen 2012). Nevertheless, as a consequence of plasma compression, the preexisting magnetic field is unavoidably amplified, stretched and aligned along the shock front, hence the synchrotron luminosity of the region is increased and high polarization levels are expected (Enßlin et al. 1998) and observed, as shown in Fig. 2.4.

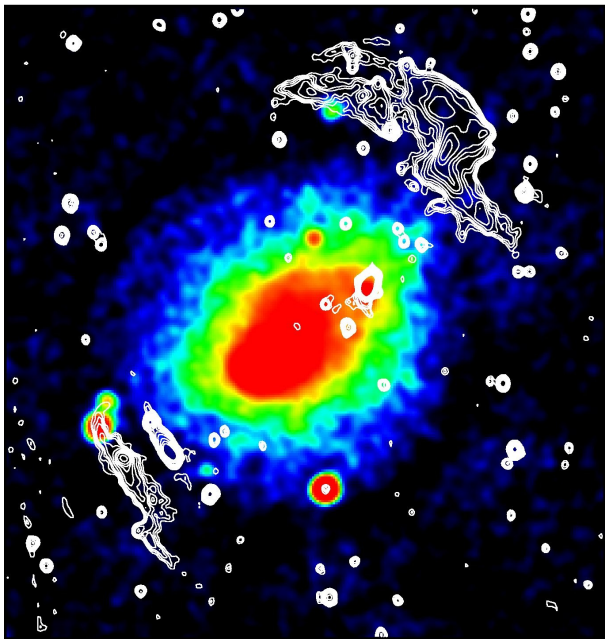

Figure 2.3: The prototype double radio relic (contours) and the ICM X-ray emission (colors) in the cluster A 3667 (Rottgering et al. 1997).

The DSA theory was originally developed in the framework of SNR in our Galaxy, where *strong shocks* with Mach numbers up to 10^3 are able to transfer $\sim 10\%$ or more of the energy flux though them into relativistic particles. By contrast, most of the kinetic energy flux penetrating cluster merger shocks is associated with *weak shocks* ($\mathcal{M} \lesssim 5$) where the acceleration efficiency is probably much less, although still poorly understood (e.g. Kang & Jones 2005). It is worth noting that stronger *external shocks* associated with the accretion of cold gas on gravitationally attracting nodes are expected in the tenuous *intergalactic medium* (IGM) (e.g. Miniati et al. 2001). However, the low gas density of such environments implies that the energy dissipated by external shocks, $\propto \rho V_{sh}^3$ (where V_{sh}^3 is the shock speed), is small. Conversely, the bulk of energy is dissipated at relatively weak shocks with $\mathcal{M} \sim 2-3$ that are associated with *major mergers* (Ryu et al. 2003; Vazza et al. 2009a). In this respect, radio relics are special environments as they are unique laboratories for constraining the physics of particle acceleration at (Mpc-scale) weak shocks. As a final remark, in DSA theory a minimum particle momenta for which particles are efficiently accelerated exists. For this reason, non-relativistic electrons are difficult to accelerate and an already existing seed population of relativistic particles is often invoked to overcome such problem (e.g. Pinzke et al. 2013). In this respect, the scenario is referred as particle *re-acceleration*.

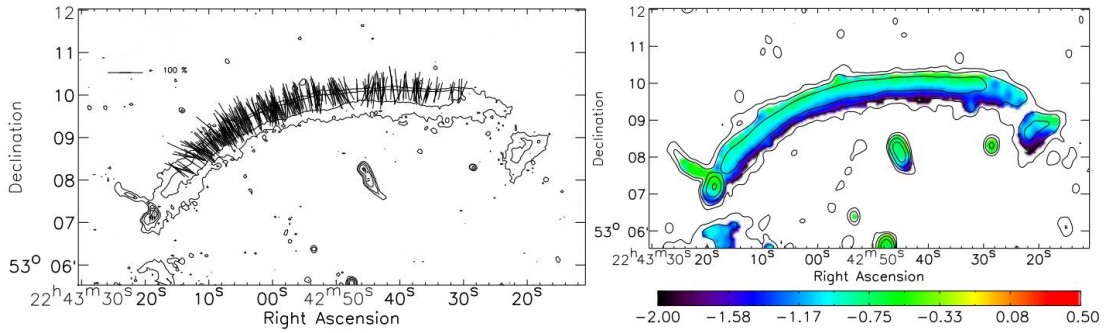

Figure 2.4: Radio polarization and spectral index maps of the northern relic in CIZA J2242.8+5301 (van Weeren et al. 2010). *Left panel*: contours of the radio emission obtained with the *GMRT* at 610 MHz. Superimposed lines represent the polarization electric field vectors obtained with the *VLA* at 4.9 GHz. The length of the vectors are proportional in length to the polarization fraction. A reference vector for 100% polarization is shown in the upper left corner. *Right panel*: radio spectral index map of the same relic, obtained with a power-law fit to measurements at five frequencies between 2.3 and 0.61 GHz. Contours of the radio emission are from the *WSRT* 1.4 GHz image.

According to the DSA linear theory, the steady-state energy power-law spectrum of an electron population with slope δ_{inj} (i.e. the injection spectrum) is related to the shock Mach number $\mathcal{M}$ (e.g. Blandford & Eichler 1987) as

$$\delta_{inj} = 2\frac{\mathcal{M}^2+1}{\mathcal{M}^2-1}, \tag{2.1}$$

which for strong shocks (e.g. supernova), $\mathcal{M} \to \infty$, is $\delta_{inj} \to 2$, while for weak shocks (e.g. galaxy mergers) is $\delta_{inj} > 2$. Hence, the acceleration process is concentrated in the lowest energy particles, which gain relatively little energy before they escape downstream, and the DSA efficiency is much greater in strong shocks than in weak shocks. Once electrons have been advected downstream, radiative cooling due to IC and synchrotron reduces the maximum electron energy causing the "volume integrated" electron spectrum to steepen by one in the power-law index, $\delta = \delta_{inj} + 1$ (Enßlin et al. 1998; Hoeft & Brüggen 2007), provided that other mechanism do not play a role behind the shock. Detailed studies of the spectral index distribution in radio relics provide indeed evidence of transverse steepening toward the cluster center (e.g. 1RXS J0603.3+4214, van Weeren et al. 2012; CIZA J2242.8+5301, Stroe et al. 2013) that strongly supports a shock origin for such sources. The integrated synchrotron spectrum from the downstream region will then result in the spectral slope $\alpha = (\delta - 1)/2 = \alpha_{inj} + 1/2$. Since the acceleration occurs at the shock location, the newest and flattest relativistic particle population is expected to reside at the shock front while the older particles age downstream producing the steepening from the outer to the inner edge observed in some relic (e.g. Fig. 2.4).

An interesting consequence of DSA theory is that one can use the spectral index at the relic front (i.e the injection index) to constrain the Mach number of the shock responsible of the particle acceleration (Eq. 2.1). This is an alternative method in the investigation of the Mach number which, so far, has always been focused in the search of X-ray discontinuities across the region of the putative shock (see Paragraph 4.2). How-

ever, recent results from X-ray observations (e.g. Akamatsu & Kawahara 2013) show that a discrepancy exists between the Mach number derived with these two different approaches. Recently, numerical simulations have been performed in order to clarify such an inconsistence. The emerging scenario is that Mach number variations over shocks (Skillman et al. 2013) and projection effects along the line-of-sight (Hong et al. 2015) might mitigate the observed differences.

2.2 Radio halos

The largest synchrotron emissions in the Universe can be found in the form of diffuse radio halos. These are giant ($\gtrsim 1$ Mpc), cluster scale, non-thermal sources permeating the central volume of merging GCs, hence they are the main proof of the existence of magnetic field on cluster-wide scales. Radio halo morphologies are quite regular and typically recall the distribution of the thermal gas of the ICM. Unlike relics, radio halos emission is unpolarized down to a few percent level, although significant polarization have been found in some cases (e.g. A 2255, Govoni et al. 2005; MACS J0717.5+3745, Bonafede et al. 2009a). Currently there have been observed about 50 halos, all in merging cluster: that, as for relics, is a crucial information to understand their origin.

The prototype of this class, Coma C at the center of the Coma cluster (Fig. 1.1 and 2.1), was detected long time ago (Large et al. 1959) and represents the best target to investigate the properties and the origin of radio halos since its vicinity ($z = 0.0231$). For this reason, it has been studied in detail by many authors in the past years (e.g. Willson 1970; Giovannini et al. 1993; Brown & Rudnick 2011). The Coma C spectrum is measured over a broad range of frequencies (Thierbach et al. 2003), showing a significant steepening for high frequencies (Fig. 2.1). This suggests a break (or cutoff) in the spectrum of the emitting particles. Such a spectral feature is relevant in the understanding of the mechanism responsible of particle acceleration (Schlickeiser et al. 1987). Nevertheless, Coma halo spectrum represents a unique case of a well sampled spectrum. Most of giant halos spectra are indeed constrained by only a few data-points, covering a small range of frequencies and do not allow a clear view of the processes that might be involved in these synchrotron sources. Recent observations of radio halos indicate that the integrated spectrum of such sources span a broad range of values, $\alpha \sim 1-2$ (Venturi et al. 2013), indicating that their synchrotron spectrum is not a universal power-law and putting relevant constraints on the mechanisms responsible for the acceleration of emitting particles.

The most extreme spectra are found in the so-called *ultra-steep spectrum radio halos* (USSRH). As their name suggests, these are characterized by spectral indexes of $\alpha \gtrsim 1.5$, which are indicative of a cutoff or a break in the spectrum of the emitting electrons at high frequency. A number of them are currently known (A 1914, Bacchi et al. 2003; A 521, Brunetti et al. 2008; A 697 Macario et al. 2010). However, because their spectral properties, this particular population of sources are likely missed by present observations at GHz frequencies (Cassano et al. 2010), being best detectable at low frequencies by future surveys (Cassano et al. 2012).

A remarkable link between the radio and X-ray properties of GCs exists. In fact, a close similarity in the morphology of radio halos and the X-ray emission of their host clusters has been noticed since the first studies (e.g. Deiss et al. 1997) and in several

cases this led to a correlation between the point-to-point surface brightness of the cluster radio and X-ray emission (Govoni et al. 2001). Furthermore, several scaling relations between the radio and thermal gas properties of GCs have been widely studied in the literature (Cassano et al. 2006, 2013). The observed correlations between the halo radio power and ICM X-ray luminosity and temperature (Fig. 2.5) could reflect a dependence of the radio halo luminosity on the cluster mass. The most striking argument that supports the connection between the origin of radio halos and cluster mergers is the so called "radio bi-modality" (Brunetti et al. 2007, 2009; Kale et al. 2015). Essentially it is found that clusters branch into two populations: one is constituted by merging systems hosting radio halos and the other one is constituted by relaxed systems that indeed do not host large-scale diffuse radio sources. This kind of analysis, together with the fact that a limited number of GCs host radio halos, represents the starting point of the theoretical models that explain the origin of relativistic particles.

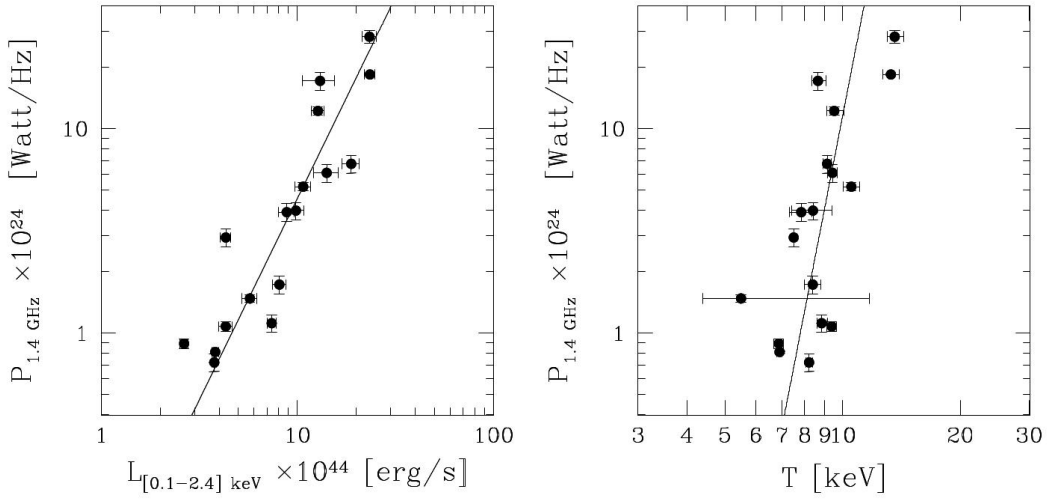

Figure 2.5: Radio power at 1.4 GHz of radio halos with size > 1 Mpc versus cluster X-ray luminosity (*left*) and versus cluster temperature (*right*) (Ferrari et al. 2008; adapted from Cassano et al. 2006).

2.2.1 Origin of radio halos

The main problem in explaining the origin of radio halos is their large scale emission. In fact, the time-scale that is necessary to electrons to diffuse on the scale of radio halos $L \sim$ Mpc is

$$\tau_{diff} \sim \frac{L^2}{4D} \gg \tau_{loss}$$

where D is the spatial diffusion coefficient and τ_{loss} is the radiative life-time of relativistic electrons undergoing synchrotron and IC energy losses. This highlights the so-called *slow diffusion problem*. Radio halos cannot originate from the diffusion of electrons, but these electrons should be continuously accelerated/re-accelerated "in situ" in the volume of the radio halo (Jaffe 1977). In the past years two main classes of models for the origin of radio halos have been proposed:

- **leptonic models** (or **re-acceleration models**): relativistic particles (i.e. *primary* electrons) injected in the cluster volume by radio galaxies, supernovae, galactic winds, etc., are continuously re-accelerated by MHD turbulence in the ICM driven by merger events (Petrosian 2001; Brunetti et al. 2001; Fujita et al. 2003; Cassano & Brunetti 2005; Brunetti & Lazarian 2007; Brunetti et al. 2008; Brunetti & Lazarian 2011; Donnert et al. 2013; Pinzke et al. 2015). In this scenario, particles are stochastically accelerated in situ by Fermi II-like mechanisms, solving in this way the slow diffusion problem for ongoing or most recent merging clusters exhibiting radio halo emission;

- **hadronic models** (or **secondary models**): inelastic nuclear collisions between relativistic protons and the nuclei of the thermal ICM continuously produce *secondary* electrons (Dennison 1980; Blasi & Colafrancesco 1999; Miniati et al. 2001; Pfrommer & Enßlin 2004; Enßlin et al. 2011). Since relativistic protons diffuse on large scale because their energy losses are negligible (Berezinsky et al. 1997; Völk et al. 1996), this scenario is able to explain the diffuse emission throughout the cluster volume.

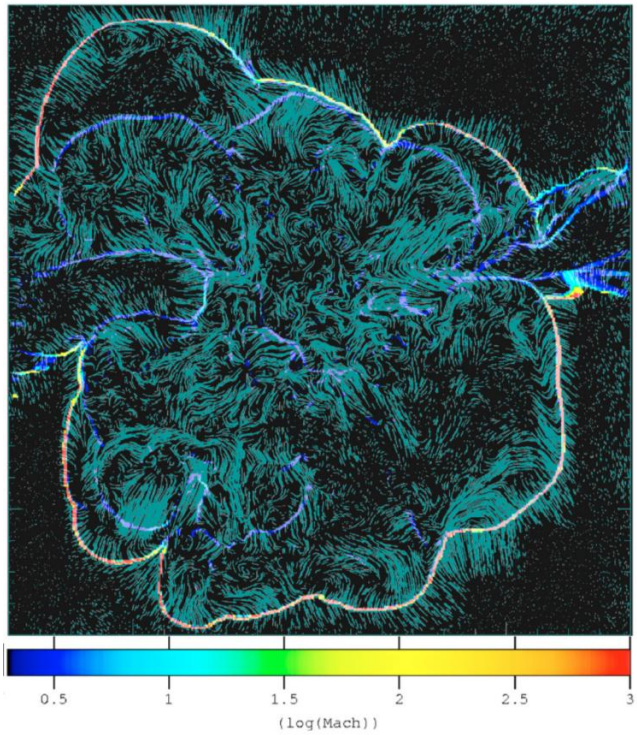

Figure 2.6: Map of Mach number (colors) and turbulent gas velocity field (arrows) in a simulated major merger (Vazza et al. 2009b). The panel is 7.5×7.5 Mpc.

Observations mostly support the re-acceleration models. Indeed, the most relevant indication that turbulence may play a fundamental role in particle re-acceleration is given by the fact that radio halos are only found in merging systems (e.g. Cassano et al. 2010). In this case, the bi-modality between halo and non-halo clusters would reflect the dichotomy existing in the evolutionary state of GCs, with merging clusters more turbulent than relaxed ones (Brunetti et al. 2009). Numerical simulations show that

mergers can generate turbulence on Mpc-scales (e.g. Dolag et al. 2005b; Vazza et al. 2006, 2012; Miniati 2015), as shown in Fig. 2.6. However, the existence of merging clusters without halos indicates that mergers are not the only necessary ingredient to power such extended emissions.

Further supports to the re-acceleration scenario come from the spectral properties of radio halos, in particular the evidence for breaks and/or ultra-steep spectra in several cases (Schlickeiser et al. 1987; Brunetti et al. 2008; Dallacasa et al. 2009; Macario et al. 2010). Their spectra indeed suggest that the energy losses of the relativistic electrons emitting in the radio band are barely balanced by the re-acceleration process, implying re-acceleration time-scales $\sim 10^8$ yr, that are consistent with Fermi II mechanisms.

Most important, hadronic models bump into important constraints coming from the combination of radio and γ-ray observations. In fact, current upper limits to the γ-ray emission from GCs (Ackermann et al. 2010, 2014) put stringent constraints on the role of hadron-hadron collisions, because high-energy emission should arise as secondary product of the interactions (see e.g. Blasi et al. 2007; Jeltema & Profumo 2011; Brunetti et al. 2012).

2.3 Radio mini-halos

Mini-halos, as their name suggests, presents some similarities with radio halos, as roundish morphologies, central location in the clusters and steep spectra. Indeed, they are smaller ($\lesssim 500$ kpc) diffuse synchrotron radio sources. The main difference between mini-halos and giant halos resides in the typical properties of their host clusters. In fact, mini-halos are detected only in relaxed, cool-core clusters, where recent major merger activity has not taken place (e.g. Gómez et al. 2002). Furthermore, these two (source) classes also differ in the synchrotron volume emissivity, which is typically larger in mini-halos (Cassano et al. 2008; Murgia et al. 2009).

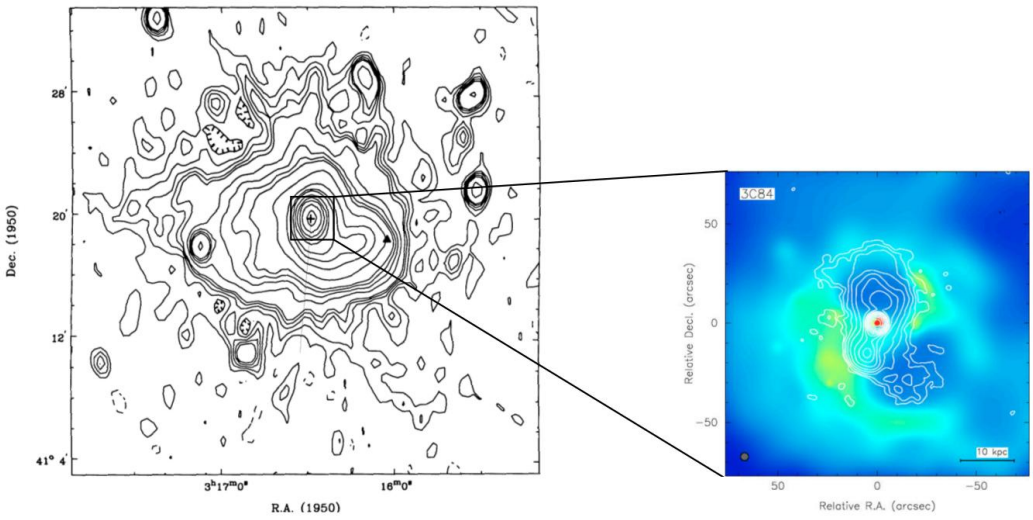

Figure 2.7: *Left panel*: 327 MHz map of the mini-halo in the Perseus cluster at a resolution of $51'' \times 77''$ (Sijbring 1993). *Right panel*: X-ray (gray scale)/radio (contours) overlay for the central part of the Perseus cluster (Fabian et al. 2000).

The non-thermal components of mini-halos, relativistic particles and magnetic fields, are mixed with the thermal ICM gas. This distinguishes them from other kind of steep spectrum radio sources in the center of relaxed/cooling core clusters, such as radio bubbles related to AGN activity, in which the ambient thermal gas is clearly separated by the non-thermal plasma. However, mini-halos emission typically embeds the powerful radio galaxies at the center of these GCs, in sizes comparable to that of the cooling region (hence they are substantially smaller than the giant halos). The presence of radio-loud AGNs into the center of GCs makes difficult to detect mini-halos. Therefore, observations with high-dynamic range and high-resolution images are requested to separate AGN/bubbles from the truly diffuse emission of the ICM. This represents a severe issue in the detection of radio mini-halos and the current observational knowledge is indeed limited to around a dozen known sources.

The prototype example of radio mini-halo is found in the near Perseus cluster (Fig. 2.7). Its proximity ($z = 0.0179$) allows a very detailed view of the phenomenon both in term of sensitivity and angular resolution. The radio source 3C 84 at its center shows X-ray cavities in the inner region, where the AGN radio activity interacts with the thermal gas (e.g. Fabian et al. 2003), but on larger scale the cluster exhibits a diffuse radio emission mixed with the thermal ICM gas. Indeed, the Perseus cluster represents a marvelous ambient to study the possible link between AGNs and mini-halos and their feedback on the ICM.

The detection of mini-halos only in dynamically relaxed systems suggests that cluster mergers do not play a fundamental role for their formation. However, in a few cases, mini-halos have been found in cooling core clusters with signatures of merging activity in the central region (A 2142, Giovannini et al. 2010; RX J1347.5-1145, Gitti et al. 2007; Ophiuchus cluster, Govoni et al. 2009). Indications of possible mergers have been claimed also in other clusters hosting radio mini-halos (e.g. Perseus cluster) even if the merging substructures detected in the X-rays are located well outside the diffuse radio source. These should be referred as *minor merger* events which were not able to destroy the central cool-core region. Consequently, it is possible that even minor mergers might play a role in particle re-acceleration in GCs (e.g. Cassano et al. 2008).

2.3.1 Origin of radio mini-halos

Although to less extent with respect to radio halos, a slow diffusion problem exists also for mini-halos, hence no diffuse emission should be possible on mini-halos scales without any in situ injection/acceleration mechanism. Similarly to radio halos, two main models have been suggested so far to explain the origin of these sources: (i) re-acceleration of electrons (leptonic models or re-acceleration models) and (ii) generation of secondary electrons (hadronic or secondary models).

According to leptonic models, seed relativistic particles are accelerated in mini-halos by MHD turbulence via Fermi-like mechanisms (e.g Gitti et al. 2002). These seeds may be naturally provided by relativistic outflows, in the form of radio lobes or bubbles, generated by the radio-loud AGNs in cluster centers. The origin of turbulence in cool-core clusters is however an open question. In order to preserve the cool-core region, more gentile processes must be involved, possibly connected with the inward advection of turbulent matter within the cooling flow region (Gitti et al. 2002, 2004).

Further indications for complex dynamics in GCs come from the spiral-shaped *cold fronts* seen in the majority of cool-core clusters (Markevitch & Vikhlinin 2007). These might be produced by *sloshing* motions in the ICM gas (Fig. 2.8) that can produce turbulence, hence powering the mini-halos (e.g. ZuHone et al. 2011b). This scenario is supported by a correlation between radio mini-halos and cold fronts that has been discovered in a few clusters (Mazzotta & Giacintucci 2008) and is also supported by recent numerical simulations (ZuHone et al. 2013).

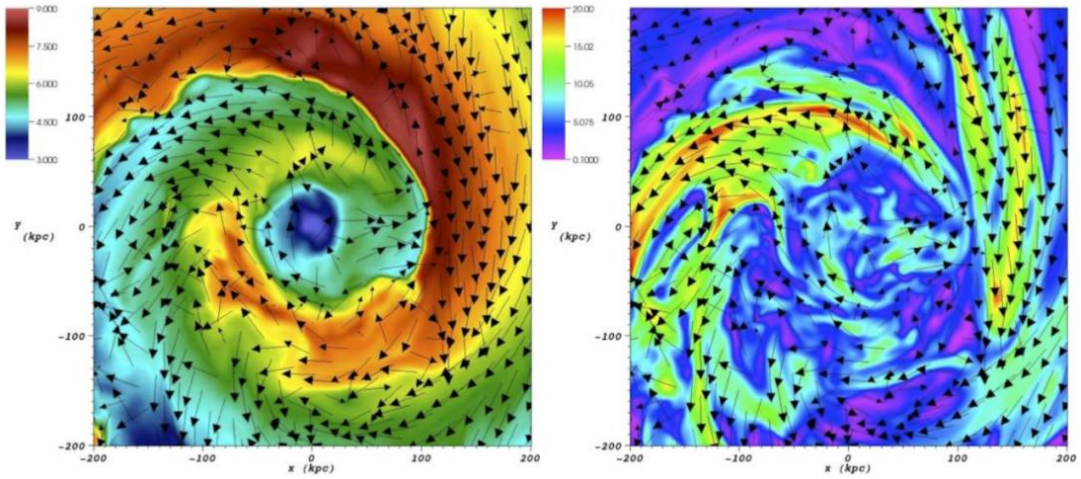

Figure 2.8: Simulation of gas sloshing in the center of a GC (ZuHone et al. 2011a). *Left panel*: Temperature (keV), showing prominent spiral-shaped cold fronts. *Right panel*: Magnetic field strength (μG), showing the field amplification near the front surfaces. Vectors show the magnetic field direction. Each panel is 400 kpc on a side.

Hadronic models are based on the generation of secondary particles via inelastic proton collisions (Pfrommer & Enßlin 2004; Keshet & Loeb 2010; Zandanel et al. 2013; ZuHone et al. 2015). In the case of mini-halos, the primary protons could be naturally provided by the powerful central AGN and then advected, streamed or diffused across the cluster core. Secondary models are particularly attractive for mini-halos as the cluster radio emission traces the denser regions, namely where the thermal targets number density is larger.

Currently, the discrimination between a leptonic and hadronic models for radio mini-halos formation is very challenging. The lack of radio observations on a wide range of frequencies is a severe limitation in the comparison between the two, preventing detailed spectral studies. At the same time, current γ-ray upper limits are not yet able to put significant constraints on the origin of these radio sources, being still consistent with a purely hadronic origin of mini-halos (Perkins et al. 2006; Aleksić et al. 2012).

2.4 Radio filaments

Magnetic fields and relativistic particles might extend on very large scales, beyond GCs, in the tenuous environment of the ICM, in cosmic filaments. In this case, faint synchrotron emission can be produced revealing the cosmic magnetic field which geometry, i.e. the spatial distribution of the field strength and its orientation, should be correlated with the large scale structures of the Universe (Ryu et al. 1998), as shown

in Fig. 1.6. Filamentary radio structures may be powered by the aggregation process which GCs undergo during their evolution, where part of the merger energy is channeled in particle acceleration and magnetic field amplification, as in the case of radio relics. This scenario is often investigated trough numerical simulations (e.g. Vazza et al. 2014).

There are several claims for detection of "filaments" in radio, although it is not clear whether observations are revealing cosmic filaments or filamentary radio emitting sources within GCs.

The prototype of such sources is the intergalactic emission detected at 325 MHz (*WSRT* data) by Kim et al. (1989) in the Coma cluster, between the radio halo Coma C and the relic 1253+275. Further follow-up observations with *VLA* confirmed the detection of diffuse emission not associated with any galaxy at 74 MHz (Enßlin et al. 1999a). However, this source is well within the GC and we may speculate that it traces a turbulent bridge generated by the presence of a group of galaxies in-falling into the main GC.

Later, Bagchi et al. (2002) discovered a large scale filamentary emission (multi-Mpc) in the network of galaxies in the cluster ZwCl 2341.1+0000. Images of such a filament have been obtained at 320 MHz and 1.4 GHz (Fig. 2.9) with the *VLA* observations. Further radio analysis of this source were performed (van Weeren et al. 2009a; Giovannini et al. 2010) and optical and X-ray data seem to confirm the complex state of this system, indicating an ongoing or recent merger (Boschin et al. 2013). Also this structure may be interpreted as diffuse emission associated with a complex merger and thus not really emission from a cosmic filament.

Only few additional examples of "filaments" are know so far (e.g. in 0809+39, Brown & Rudnick 2009) that also points out the difficulty to detect these structures.

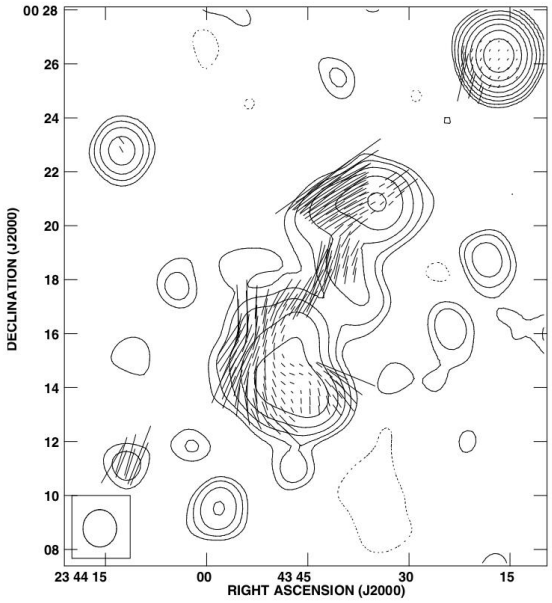

Figure 2.9: Large-scale radio emission from ZwCl 2341.1+0000, obtained with the *VLA* at 1.4 GHz (resolution $83'' \times 75''$). Contours show the total intensity emission, lines refer to the polarized emission. Their orientations represent the projected electric-field (not corrected for the Galactic rotation), the length is proportional to the fractional polarization (Giovannini et al. 2010).

Despite their elusive nature, radio filaments within or beyond GCs could provide a tool to understand the process of amplification of magnetic field in the ICM. For this reason, these sources are particularly interesting (see the next Chapter for more details on ICM magnetic fields). Next generation instruments will shed light on this point and forecasts for their detection with future surveys has already been presented (Vazza et al. 2015).

2.5 Hard X-ray emission

Non-thermal signals from GCs are not only found in the radio band. In fact, since GCs contain the relativistic electrons responsible for extended synchrotron sources, hard X-ray (HXR) emission by IC scattering with CMB photons is also expected (Harris & Grindlay 1979; Rephaeli 1979).

The main difficulty in studying IC emission from GCs is the confusion due to the thermal emission from the ICM. This problem can be solved aiming the X-ray observations at higher energies ($\gtrsim 10\,\mathrm{keV}$), where thermal bremsstrahlung contribution drops dramatically (Eq. 1.1). The first instruments that allowed such studies were *BeppoSAX* and *Rossi X-ray Timing Explorer* (*RXTE*) satellites.

Non-thermal HXR emission has been claimed for the first time in the Coma cluster (Rephaeli et al. 1999; Fusco-Femiano et al. 1999), even if the detection has remained controversial (Rossetti & Molendi 2004; Fusco-Femiano et al. 2007; Wik et al. 2009). It appears as an excess of the thermal emission in the hardest tail of the spectrum (Fig. 2.10) that is interpreted as due to IC process. Although supra-thermal bremsstrahlung was originally proposed as an alternative explanation (Enßlin et al. 1999b; Blasi 2000; Sarazin & Kempner 2000; Dogiel 2000), Petrosian (2001) showed that unrealistic energy budget would be required by these alternative models. Consequently if these controversial observational claims will be confirmed by future observations, IC emission provides the most reasonable explanation.

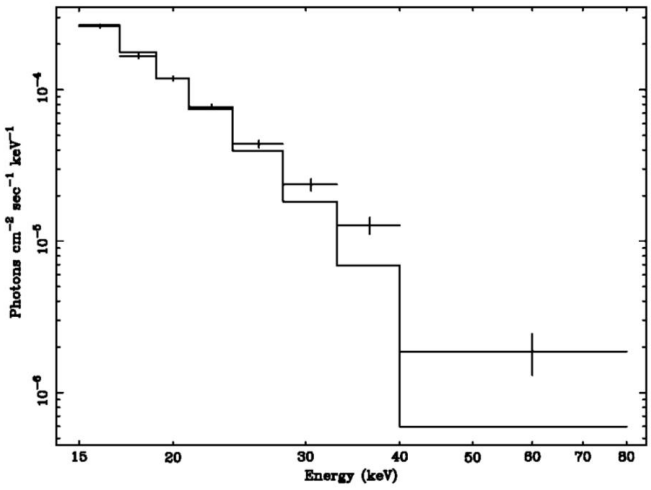

Figure 2.10: HXR spectrum of the Coma cluster (*BeppoSAX*). The continuous line represents the best fit with a thermal component at the average cluster gas temperature of 8.1 keV. The emission excess in the data is evident (Fusco-Femiano et al. 2004).

The detection of IC and synchrotron emissions in GCs is an important tool in the investigation of some properties of the ICM.
The typical energy of ultra-relativistic electrons emitting photons observed in the HXR band ($> 20\,\mathrm{keV}$), with energy E_{ph}, via IC of the seed CMB photons is

$$E_e \sim 3 \left(\frac{E_{ph}}{30\,\mathrm{keV}} \right)^{\frac{1}{2}} \quad [\mathrm{GeV}]$$

the energy of relativistic electrons emitting synchrotron radiation, emitted at redshift z and observed at frequency ν_0 is

$$E_e \sim 7 \left(\frac{\mu\mathrm{G}}{B} \frac{\nu_0}{\mathrm{GHz}} \right)^{\frac{1}{2}} (1+z)^{\frac{1}{2}} \quad [\mathrm{GeV}]$$

as a consequence synchrotron emission in clusters diffuse radio sources and IC emission in the HXR sample pretty much the same population of relativistic particles. Assuming that X-ray and radio emissions arise both from the same power-law electrons population, in the form $N(E_e) \propto E_e^{-\delta}$, synchrotron and IC spectra are both power-law and share the same spectral index $\alpha = (\delta - 1)/2$. The IC flux received by the observer at frequency ν_X can be calculated from the synchrotron flux received at the frequency ν_R with

$$F_{IC}(\nu_X) = 1.38 \times 10^{-34} \left(\frac{F_{syn}(\nu_R)}{\mathrm{Jy}} \right) \frac{(1+z)^{\alpha+3}}{\langle B_{\mu\mathrm{G}}^{1+\alpha} \rangle} \left(\frac{\frac{\nu_X}{\mathrm{keV}}}{\frac{\nu_R}{\mathrm{GHz}}} \right)^{-\alpha} \zeta(\alpha) \quad [\mathrm{erg\,s^{-1}}] \qquad (2.2)$$

where $\langle \ldots \rangle$ denotes the emission-weighted quantity in the emitting volume and $\zeta(\alpha)$ is a dimensionless function whose values for different spectral indexes can be found in Brunetti & Jones (2014). The above equation reveals that the detection of IC emission from GCs in the HXR band constrains (or provides a measure for, if the emission is detected) the average value of the magnetic field in the emitting region (see Paragraph 3.2 for more details).

So far, HXR detections in GCs have been claimed with instruments with very poor angular resolution and sensitivity. Thus, future observations with *NuSTAR* and, especially, *ASTRO-H* are necessary to solve the current lack of data providing information on the HXR emission or by providing deeper upper limits to the IC flux (Bartels et al. 2015).

Chapter 3

Magnetic fields in the ICM

MAGNETIC FIELDS are essential to produce the diffuse synchrotron emissions detected in GCs and they may play an important role in the microphysics of the ICM (e.g. thermal conduction, particle transport). The presence of magnetic fields with intensity of the order of μG in the ICM is now well established by several measurements arising from different and independent observations. However, their origin is still under debate and several processes have been proposed to justify their actual measured values.

The information on magnetic fields is directly provided from radio observations of cluster-wide diffuse sources and from studies of rotation measure of polarized radio sources embedded in clusters or behind them. Further techniques adopted to infer the presence and give limits to ICM magnetic field strengths are X-ray analysis of IC emission, physical considerations in the case of of cold fronts.

Extended synchrotron emission over the whole cluster volume, e.g. a radio halo, shows that magnetic field can be spread on very large scales. Furthermore, polarization and Faraday rotation studies indicate that ICM fields are not regularly ordered on Mpc scales but follow more complex topologies. A scaling of the magnetic field strength with the thermal gas density has been claimed implying a decrease of the field strength with cluster radius.

In the cluster outskirts, magnetic fields reveal themselves through radio relics. The presence of these synchrotron sources in the peripheries is relevant to prove the existence of magnetic fields $\gtrsim 1\,\mu$G even at large distance ($\gtrsim$ Mpc) from cluster centers.

In the following, a brief overview of the main techniques to investigate ICM magnetic field will be provided (for reviews, see Carilli & Taylor 2002; Govoni & Feretti 2004; Dolag et al. 2008).

3.1 Faraday rotation effect

Linearly polarized radiation propagating in a magnetized plasma experiences Faraday rotation (see Fig. 3.1), i.e. a phase displacement of its plane of polarization. A wave with an intrinsic polarization angle Ψ_0 has its position angle rotated by an amount

$$\Delta\Psi = \Psi - \Psi_0 = \lambda^2 RM \tag{3.1}$$

where λ is the observed wavelength of the radiation and

$$RM \propto \int_0^L n_e B_{\parallel}\, dl \tag{3.2}$$

is the rotation measure (RM) which is related to the electron density n_e and the magnetic field component along the line-of-sight $B_{\parallel}$ sampled through the plasma path length L.

The observations of polarized radio sources within or behind cluster of galaxies are a promising technique to gather information about ICM magnetization level. In fact, performing multi-frequency analysis of such objects, an estimate of RM along a given source direction is provided by a linear fit of Eq. (3.1). At least three different wavelength measurements are needed to determine RM due to the $\Psi = \Psi \pm n\pi$ ambiguity.

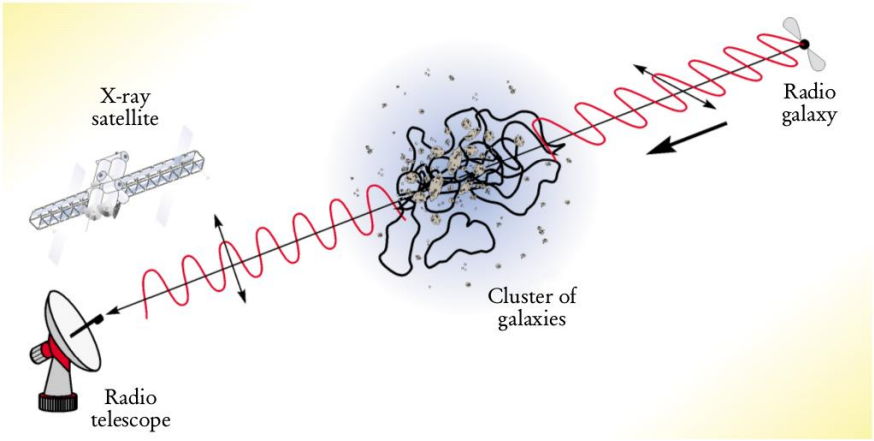

Figure 3.1: Faraday rotation due to the passage of a linearly polarized wave through the magnetized ICM (Kronberg 2002).

The study of the RM of extended sources located at different projected distances from the cluster center allows to collect information on the coherence structure of ICM magnetic field. The observed fluctuations of RM led to the conclusion that the field is not regularly ordered on cluster sizes ($\sim$ Mpc) but patchy and turbulent on a range of scales (see e.g. Tribble 1991). If one assumes that field reversal scales are filling the entire cluster volume and are uniform in size but with random orientation, the RM distribution along any given line-of-sight is expected to be Gaussian with zero mean, $\langle RM \rangle = 0$, and variance given by

$$\sigma^2_{RM} \propto \int_0^L (n_e B_{\parallel})^2\, dl\,. \tag{3.3}$$

Considering a β-model distribution for the ICM density (Eq. 1.4) and a reference coherence scale of the magnetic field Λ_c, the RM dispersion as a function of the projected distance from the cluster center $r_\perp$ is obtained by integrating Eq. (3.3)

$$\sigma_{RM}(r_\perp) \propto \frac{B n_0 r_c^{1/2} \Lambda_c^{1/2}}{(1 + r_\perp^2/r_c^2)^{(6\beta-1)/4}} \sqrt{\frac{\Gamma(3\beta - 0.5)}{\Gamma(3\beta)}}$$

where n_0 is the central gas density and Γ the Gamma function (Feretti et al. 1995; Felten 1996). If Λ_c is inferred from the measurements of RM signal across extended sources, the cluster magnetic field can be estimated.

The presence of cells is nowadays well established and is needed to explain part of the features of cluster fields. Nevertheless, filaments and/or substructures with different coherence scales are likely present in the ICM, thus the assumption of a single cell size Λ_c is too simplified (Newman et al. 2002). In this respect, models with different cell properties and numerical investigation have been preformed (e.g. Murgia et al. 2004).

Some caveats on this approach must be taken into account during RM studies. First of all, Faraday rotation estimations of the cluster magnetic field give averaged values of B along the line-of-sight, weighted by the thermal gas distribution (see Eq. 3.2). Moreover, some contributions to RM may be due to our Galaxy or could be local to the source itself. If, on one hand, the Galactic effect is known from the study of different sources at different Galactic latitudes and so can be subtracted, on the other hand, internal or local contributions due to the source, which is very uncertain, bias results. In fact, some fluctuations of RM in the cluster volume that are interpreted as patchiness of the ICM field may be produced by the compression of the plasma due to an expanding radio source in the cluster, enhancing the local RM values (e.g. Bicknell et al. 1990; Rudnick & Blundell 2003).

Observational constraints

First attempts to use Faraday rotation were carried out for the radio source Cygnus A. Dreher et al. (1987) rejected the hypothesis that the observed structure of the rotation was internal to the source or produced in our Galaxy but proposed that it was originated in the hot ICM enshrouding Cygnus A. They found that the observed RM can be reproduced for cluster magnetic field strengths of $2-10\,\mu$G.

Since the study on Cygnus A, the observation of RM in GCs has become a fruitful tool to investigate ICM magnetic field. The strategy adopted thereafter was to obtain RM of background sources located at different cluster impact parameters and to derive the value of σ_{RM} in order to estimate the magnetic field once the thermal gas density is assumed/obtained from X-ray data analysis.

Clarke et al. (2001) presented a remarkable statistical work on the RM due to magnetized ICM. They did a statistical study of 16 Abell clusters considering polarized sources at different impact parameters plus a control sample. The results, shown in Fig. 3.2, demonstrated that the cluster sample is affected by larger RM, which become more significant as the source is seen at smaller impact parameter. The model constrained magnetic fields $\sim 5\,\mu$G and cell sizes of the order of $\sim 10\,$kpc, demonstrating that Faraday rotation is due to the ICM.

The Coma cluster has been one of the most important targets for RM analysis and its magnetic field was investigated with several approaches (see the next Paragraphs). A first statistical analysis came from Kim et al. (1990), who analyzed 18 radio sources founding larger RM in the inner part of the cluster. The estimated magnetic field strength responsible for this excess was found to be $\sim 2\,\mu$G, with a cell size in the range $10-30\,$kpc. Then, in Kim et al. (1991), a better source statistics provided a value of the field strength of $\sim 1\,\mu$G. However, an analysis of the radio source NGC 4869, located near the cluster center, led Feretti et al. (1995) to conclude for a field of $\sim 6\,\mu$G and a cell size of $\sim 1\,$kpc for the same cluster. More recently, Bonafede et al. (2010) investigated the radial profile and the strength of the Coma cluster magnetic field comparing RM images with numerical simulations of the magnetic field power spectrum.

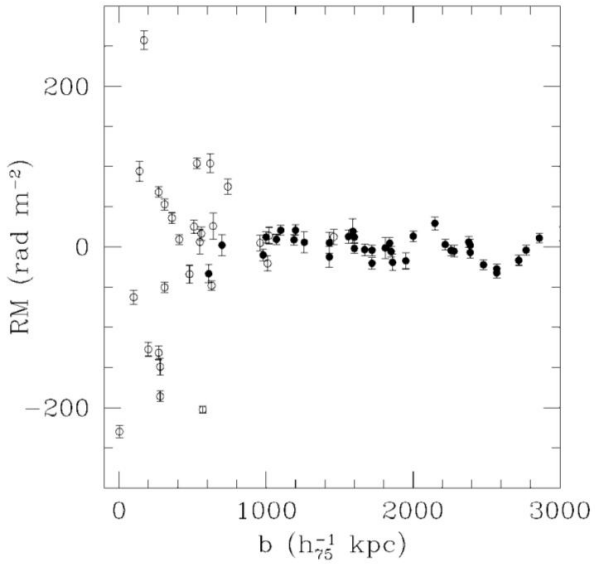

Figure 3.2: The values of RM as a function of source impact parameter for 16 Abell clusters. The *open symbols* represent sources viewed through the cluster, while the *closed symbols* are the control sample sources at impact parameters beyond the cluster gas (Clarke et al. 2001).

A central magnetic field of $\sim 5\,\mu$G was estimated and its profile was found to decrease with the radial distribution of the thermal component.

Studies on cooling core clusters derived values of the magnetic field strengths that are typically $2-3$ times higher compared to those non-cooling core ones (Perley & Taylor 1991; Taylor & Perley 1993; Allen et al. 2001) possibility due the compression in cool-cores and to the peculiar dynamics of these regions.

As a final point, we also point out that Faraday rotation analyses are essential in the study of the magnetism on large scale at early cosmological epochs. Deeper observations, in fact, lead the analysis of RM of high-z polarized sources that are sensitive to the average environment they passed through. As a result, an increase of RM with redshift is observed (Pentericci et al. 2000).

3.2 Inverse Compton emission

Radiative cooling of high-energy relativistic electrons is due to synchrotron and IC emission. Particle energy time evolution is described by

$$\frac{d\gamma}{dt} \propto -\left(B_{CMB}^2 + B^2\right)\gamma^2$$

where

$$B_{CMB} = 3.25(1+z)^2 \quad [\mu\mathrm{G}] \tag{3.4}$$

is the equivalent magnetic field due to IC with the CMB at redshift z. The dominance of any of the two depends on the strength of the field in the region where the emission is produced. For $B > B_{CMB}$, synchrotron will be the dominant radiative process, otherwise IC will dominate.

The IC emissivity is proportional to the energy density in the photon field $\varepsilon_{ph} = B_{CMB}^2/8\pi$ whereas the synchrotron emissivity is proportional to the energy density in the magnetic field $\varepsilon_B = B^2/8\pi$. A proportionality between synchrotron and IC luminosities thus exists

$$\frac{L_{syn}}{L_{IC}} \propto \frac{\varepsilon_B}{\varepsilon_{ph}}.$$

In the above equation the only unknown quantity is ε_B. For this reason, once the X-ray and radio luminosities are measured, an estimation of the magnetic field can be performed.

The main difficulty in deriving magnetic field strengths with this approach is caused by the lack of clear detections of IC emission. In this case, lower limits to the strength of the field can only be derived (see Paragraph 2.5).

Observational constraints

Thermal emission is the dominant mechanism at high energy from GCs. For this reason, detection of IC emission is possible only at higher energies, in the HXR, where thermal emission fades away. Before the launch of the satellites *BeppoSAX* and *RXTE* there was not enough sensitivity in the HXR band to study IC emission from GCs. For this reason, only lower limits to the ICM magnetic field strength were set to $B > 0.1\,\mu$G (Rephaeli et al. 1987). The new instruments allowed to study the high-energy emission (or its lack). Some results concerning (i) radio halos and (ii) radio relics follow.

(i) Independent detections (still controversial) of non-thermal IC emission in the Coma cluster (Fig. 2.10) were claimed (Rephaeli et al. 1999; Fusco-Femiano et al. 1999). The comparison between the flux in radio band, due to the halo, and in the X-rays, due to IC, allowed an estimate of the volume-averaged cluster magnetic field of $\sim 0.2\mu$G. Only upper limits to the non-thermal X-ray emission were derived for the clusters A 3667 (Fusco-Femiano et al. 2001) and A 2163 (Feretti et al. 2001). Fusco-Femiano et al. (2000) found further indications of a magnetic field below the μG level in A 2256. More recently, the advent of new instruments such as *INTEGRAL*, *Swift* and *Suzaku*, made possible observational campaigns well beyond the X-ray domain. However, the difficulties in observing high-energy emission and in disentangling it between thermal and non-thermal origin still remain. As an example, *Suzaku* and *Swift* views of the Coma cluster provided only lower limits of $0.15 - 0.25\,\mu$G (Wik et al. 2009, 2011).

(ii) Few constraints on radio relics IC emission exist so far. On one hand, relics cover an aperture angle that is smaller than halos and have peripheral locations, making their detection in the HXR band less problematic. On the other hand, however, relics are associated with shock compression regions where the average magnetic fields is presumably larger than that (averaged) in the region of radio halos, thus reducing the expected IC flux. Due to the smaller aperture angle of relics and their peripheral position where thermal emission is fainter, it is possible to check the presence of IC emission also in the soft X-rays. The first result came from *ROSAT* observations of A 85. For this cluster, a magnetic field strength value of about $1\,\mu$G was achieved in the relic region (Bagchi et al. 1998). Limits on the magnetic field of the relic in A 3667 have been obtained in the X-rays with *Suzaku* (Nakazawa et al. 2009; Akamatsu et al. 2012) and *XMM-Newton* (Finoguenov et al. 2010).

3.3 Equipartition condition

The magnetic field in a radio source can be also inferred under the hypothesis of minimum energy (particles+field) of the relativistic plasma producing the observed synchrotron luminosity. The total energy of a relativistic plasma cloud is made of the contribution due to the kinetic energy in relativistic protons (U_{pr}) and electrons (U_{el}) and the magnetic field contribution (U_B)

$$U_{tot} = U_{el} + U_{pr} + U_B \,.$$

The magnetic field energy contained in a given source in a volume V is given by

$$U_B = \frac{B^2}{8\pi}\xi V$$

where ξ is the filling factor that accounts for the fraction of the source volume effectively occupied by the magnetic field B. Given k, ratio of the energy between the relativistic protons to that in electrons, the kinetic energy in relativistic particles can be written as

$$U_{part} = (k+1)U_{el} \,.$$

It is possible to infer the electron energy content as a function of the synchrotron luminosity L_{syn} and obtain the basic dependencies of the total energy content on B

$$U_{tot} = (1+k)c_{12}L_{syn}B^{-3/2} + \frac{B^2}{8\pi}\xi V \,. \tag{3.5}$$

The above equation has a minimum, as shown in Fig. 3.3, that is achieved when the contributions of magnetic field and relativistic particles are approximately equal

$$U_B = \frac{3}{4}(1+k)U_{el}$$

and from that the name "energy equipartition" was set. The minimum total energy content of the relativistic plasma cloud is then

$$U_{tot}(min) = c_{13}\left(\frac{3}{4\pi}\right)^{3/7}(1+k)^{4/7}\xi^{3/7}V^{3/7}L_{syn}^{4/7}$$

which is the minimum of Eq. (3.5) and it leads to the total minimum energy density

$$u_{min} = \frac{U_{tot}(min)}{V\xi} = c_{13}\left(\frac{3}{4\pi}\right)^{3/7}(1+k)^{4/7}\xi^{-4/7}V^{-4/7}L_{syn}^{4/7} \,.$$

The constants c_{12} and c_{13} are related to synchrotron theory and are dependent of the spectral index of the synchrotron radiation and of the frequency range over L_{syn} is integrated (typically between 10 MHz and 100 GHz). They can be found in Pacholczyk (1970).

Once u_{min} has been evaluated, the equipartition magnetic field can finally be computed as

$$B_{eq} = \sqrt{\frac{24\pi}{7} u_{min}}\,.$$

Equipartition of energy is a simple and direct method to estimate the magnetic field of a radio source. However, the condition of minimum energy content is not justified a priori.

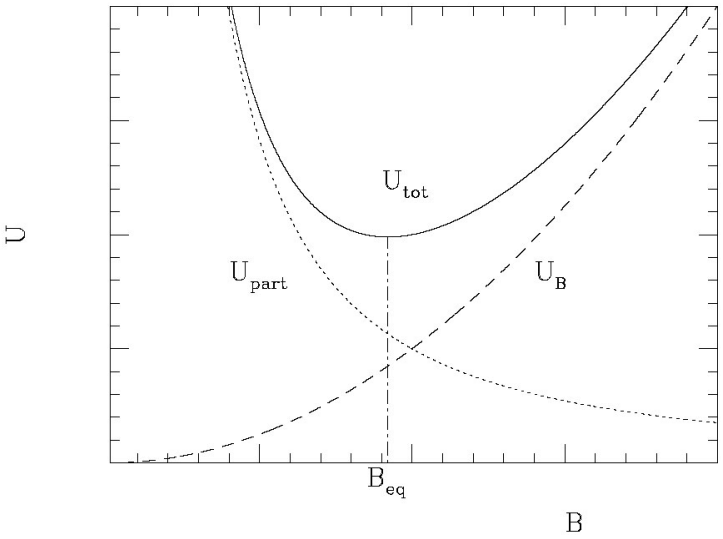

Figure 3.3: Total energy content U_{tot} in a radio source (in arbitrary units) shown as the contribution of the energy in magnetic field ($U_B \propto B^2$) and in relativistic particles ($U_{part} = U_{el} + U_{pr} \propto B^{-3/2}$) (Govoni & Feretti 2004).

The previous treatment to obtain the equipartition magnetic field is the "classical" approach that can be found in Pacholczyk (1970). In Brunetti et al. (1997) a "revised" approach to equipartition is presented, where the substantial change is in the analysis of particle energy content. In fact, the adoption of a frequency range in which evaluate the particle energy content leads to a physical bias. The emission frequency of electrons irradiating via synchrotron process is indeed $\nu \propto \gamma B^2$, hence for a given frequency range the resulting range of energy of the electrons depends on B, which is an unphysical condition. For this reason it is better to directly assume an energy interval for evaluating U_{el}. In such a way the energy ratio between particles and magnetic field is

$$\frac{U_{part}}{U_B} = \frac{2}{1+\alpha}$$

which leads to a "perfect equipartition" for $\alpha = 1$ (Brunetti 2004).

Assuming that in the computation of energy content $\gamma_{min} \ll \gamma_{max}$, the new expression for the equipartition magnetic field (for $\alpha > 0.5$) is

$$B'_{eq} \sim 1.1 \gamma_{min}^{\frac{1-2\alpha}{3+\alpha}} B_{eq}^{\frac{7}{2(3+\alpha)}} \quad [\mathrm{G}] \tag{3.6}$$

where B_{eq} is the "classical" equipartition magnetic field obtained by integrating the radio spectrum between 10 MHz and 100 GHz.

It is worth noting that the framework of energy equipartition presents unavoidable uncertainties due to some quantities that appear in Eq. (3.5). These are the poorly know values of k, which depends on the mechanism of generation of relativistic electrons, the unknown of the volume filling factor ξ and the geometry, and so to the volume V, of the source. In fact, the value of k is unknown, depending on the acceleration mechanism (and that is still under debate for GCs diffuse radio emissions, as discussed in Chapter 2), on the plasma composition ($k = 0$ for a light plasma made of electrons and positrons) and age (electrons lose energy with time while protons do not, leading to a large k). Furthermore, the filling factor, generally assumed to be 1, may be an oversimplification, given that radio sources exhibit inhomogeneous traits.

Observational constraints

Despite its uncertainties, estimating the magnetic field of a synchrotron source through equipartition condition is often used in the literature as a zeroth order value since its simple observable requirements. For cluster diffuse emission, $k = 1$ (or $k = 0$) and $\xi = 1$ are typically assumed. For (i) radio halos spherical symmetry is also assumed while for (ii) radio relics the geometry can be a difficult issue to deal with. In the following a taste of the main equipartition results is given.

(i) Radio halos are easier to treat with such an approach and the first estimate came for the Coma cluster. For this source, Giovannini et al. (1993) found a strength value of $0.45\,\mu$G. For A 2256, instead, the estimated field is slightly above the μG level (Clarke & Enßlin 2006). In this respect, a scatter in magnetic field intensities between clusters exists but, overall, estimates for minimum energy magnetic field strengths for radio halos are typically in the range $0.1 - 1\,\mu$G (Feretti 1999). On the other hand, van Weeren et al. (2009b) estimated a conspicuous higher field strength for the cluster MACS J0717.5+3745 of either $3.2\,\mu$G or $5.8\,\mu$G if "revised" instead of "classic" approach is used. This is justified by the fact that MACS J0717.5+3745 is one of the most luminous radio halo, with an atypical high luminosity.

(ii) Estimates of equipartition magnetic field in radio relic have also been obtained. In studying the diffuse emission in the Coma cluster, Giovannini et al. (1991) found a magnetic field strength of $0.55\,\mu$G for the relic region. For the relic in A 3667 the field intensity was set to be in the range $1.5 - 2.5\,\mu$G (Johnston-Hollitt 2003). Double relics are suitable targets to measure field strengths, which are typically in the range from 0.5 to $3\,\mu$G (Bagchi et al. 2006; Bonafede et al. 2009b; van Weeren et al. 2009a). These results indicate that magnetic fields in relics are larger than in halos. One possibility is that the field enhances its strength due to the shock compression.

3.4 Cold fronts

Cold fronts (e.g. Fig. 3.4) are detected as discontinuities in the X-ray surface brightness and are likely produced at late times during minor cluster mergers. These structures are distinguished from shocks because the density increase across the fronts are not accompanied by a temperature drop. Across cold fronts there are no significant changes in the pressure of the gas (see e.g. Markevitch & Vikhlinin 2007 for a review).

The presence of sharp edges can be justified only if the thermal conduction is assumed two order of magnitude smaller than the "standard" (Spitzer 1962)

$$\kappa = \frac{1.84 \times 10^{-5} T_e^{5/2}}{\ln \Lambda} \quad [\mathrm{erg\,s^{-1}\,K^{-1}\,cm^{-1}}] \tag{3.7}$$

where $\ln \Lambda$ is the Coulomb logarithm. If not, temperature gradients and cool structures in the hot ICM on scales of ~ 0.1 Mpc would not occur in the X-rays as they would evaporate on time-scales of $\sim 10^7$ yr because heat conduction. Chandran & Cowley (1998) showed that the presence a tangled magnetic field can reduce the thermal conductivity from the Spitzer value. Furthermore, magnetic field also leads to the suppression of Kelvin-Helmholtz mixing along the contact discontinuities, not detected in cold fronts, preserving therefore the sharp features.

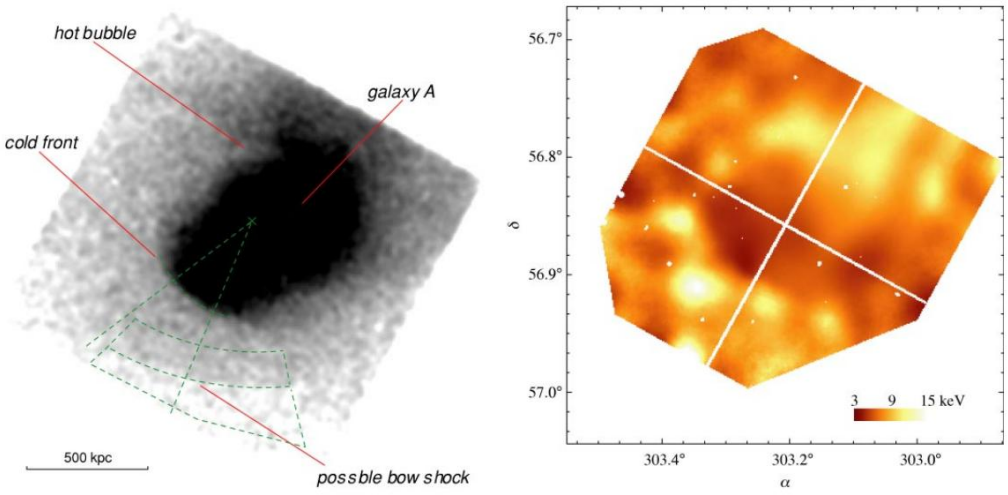

Figure 3.4: X-ray view of A 3367 (Vikhlinin et al. 2001a). *Left panel*: a smoothed $0.5-4$ keV *Chandra* image of the cluster where a sharp surface brightness discontinuity, i.e. the cold front, emerges. *Right panel*: temperature map of the same region.

This scenario explains the sharp fronts detected in some GCs and leads to an estimate of the invoked magnetic field. Using theoretical arguments, one can infer the strength and the geometry of the field necessary to avoid the smearing of the cold front due to Kelvin-Helmholtz instabilities that would occur if no stabilization factors would be present. The magnetic field estimates with such an approach refer to layers of plasma that are amplified by the stretching of the field lines. However, they can be related to the unperturbed field values by simply correcting for the gas compression factor in the cold front.

Observational constraints

The high resolution and sensitivity of *Chandra* satellite allowed the detection of several cold fronts in GCs due to major/minor mergers, AGN activity inside the ICM and gas sloshing motions.

The detection of a sharp discontinuity in the X-rays in A 2142 (Markevitch et al. 2000) pointed out that thermal conductivity needs to be suppressed. In fact, in order to produce the temperature jump of such a cold front, a suppression at least by a factor of 100 (Ettori & Fabian 2000) with respect to the classical value (Eq. 3.7) is required.

In Fig. 3.4 a marvelous manifestation of a cold front detected in A 3667 (Vikhlinin et al. 2001a) is presented. In that case, the temperature discontinuity occurs over a scale of ~ 5 kpc and the front appears very sharp, becoming smeared at larger angles from its curvature center. Vikhlinin et al. (2001b) pointed out that the presence a of layer in which the magnetic field is roughly parallel to the front would reproduce such a feature. The field required for this interpretation has a strength of the order of $10\,\mu$G. Since that value refers to a region near the cold front, where the field is compressed and amplified, this must be considered as an upper limit to the field strength in the ICM.

3.5 Radio relic emission

Markevitch et al. (2005) proposed a method to constrain magnetic field strengths in radio relics independently of the details of the mechanisms responsible for the acceleration of the emitting electrons.

After being accelerated/re-accelerated at shocks associated with relics, relativistic electrons are advected into the downstream region at the downstream velocity V_d and cool due to IC and synchrotron losses. As first approximation, the combination of transport and aging of the emitting electrons determines the thickness of the radio relic as measured at different frequencies. The emitting electrons can travel a maximum distance from the shock $= V_d \tau_\nu$, where τ_ν is the radiative life-time, which depends on the magnetic field B, on the equivalent magnetic field due to IC with the CMB at redshift z (Eq. 3.4), and on the observing frequency ν

$$\tau_\nu = 1.6 \times 10^3 \frac{B^{1/2}}{B^2 + B^2_{CMB}} \times [\nu(1+z)]^{-1/2} \quad [\mathrm{Myr}] \tag{3.8}$$

where magnetic fields have been expressed in μG and the frequency in GHz (Parma et al. 1999). For this reason, the measurement of the relic transverse size at several frequencies constrains the magnetic field strength in the source, once the downstream velocity is derived from X-ray observations (see Paragraph 4.2).

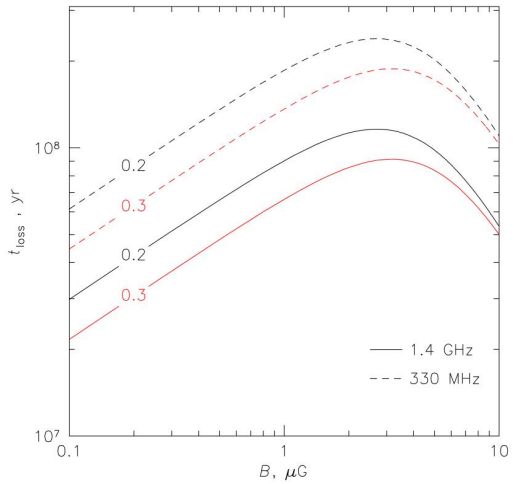

Figure 3.5: Life-time of relativistic electron that contribute the most to the synchrotron emission at a given frequency as a function of the magnetic field (Markevitch et al. 2005). Two frequencies are shown as *solid* and *dashed* lines. *Black* and *red* lines correspond to two different redshifts.

Since Eq. (3.8) is not a monotonic function of B (see Fig. 3.5), the solution provides two different values of the magnetic field strength responsible of the energy losses of the emitting particles, in one case $B_{CMB} > B$ and in the other $B_{CMB} < B$. The maximum particle life-time is achieved when $B = B_{CMB}/\sqrt{3}$.

Observational constraints

The approach proposed by Markevitch et al. (2005) is simple and straightforward but was applied only once in the literature. In fact, one has to take into account some caveats in adopting this method. One is given by the fact that Eq. (3.8) has not a unique solution, hence two value for the field strength are gathered. Another critical point is due to the estimation of the downstream velocity that is constrained by X-ray observations only in a very few cases. In addition, the model does not consider projection effects that could influence the measurement of the relic thickness. We will discuss all these problems in Chapter 4.

The northern relic in CIZA J2242.8+5301 (Fig. 2.4) represents a suitable object to be investigated with this method. In this respect, van Weeren et al. (2010) measured the full-width at half-maximum (FWHM) of the relic at one frequency and combined it with an estimate of the downstream velocity. Their estimate for the field strength is 1.2 or $5\,\mu$G. However, projection effects can increase the observed width of the relic and affect the derived magnetic field strength. Therefore, the true intrinsic width of the relic could be smaller, which implies that $B > 5\,\mu$G or $< 1.2\,\mu$G.

3.6 Origin and amplification of cluster magnetic fields

Different theoretical frameworks have been made to explain the observed magnetic properties of the ICM. A fundamental point that is broadly accepted is that whatever the field origin is, some amplification mechanisms are required to enhance the extremely weak seed fields to the typical strengths $\sim \mu$G of nowadays clusters. Currently, two scenarios can be distinguished for the ICM magnetic field origin as a function of the epoch of its establishment:

- in a number of **primordial models**, magnetic fields are generated in the early Universe before the epoch of recombination. Inflation, neutrino-photon decoupling and phase transitions were proposed as periods of formation of the weak seeds of the order of $\sim 10^{-21}$ G (see Grasso & Rubinstein 2001 for a review), when mechanisms as the "Biermann battery" effect (Biermann 1950) might be involved in the creation of the field. A cosmological origin for magnetic fields is supported by the evidence that they are present almost everywhere in the Universe, i.e. the "cosmic magnetism";

- in the second scenario, a **galactic origin** is considered. These models argue that the ejection from galactic winds due to stellar outflows and supernova explosions in normal and starbust galaxies (e.g. Kronberg et al. 1999), as well as radio jets ejected by AGNs in clusters, contributes to deposit magnetic fields in the ICM. Such a scenario is supported by the fact that the ICM is polluted by metals produced by SFGs and its main expectation is that magnetic fields are prevalently located around galaxies and within the cluster.

Independently from their origin, magnetic fields in the ICM are unavoidably amplified during the evolution of GCs. Several mechanisms connected with the hierarchical process of structure formation can produce amplification of the field. In merger events, shocks, bulk flows and turbulence are generated within the ICM. The first two simply compress the magnetized plasma increasing its strength (non-linear amplification is not considered since the weak shocks expected in mergers), while turbulence and instabilities are promising sources of non-linear amplification and so are efficient to enhance the seed field, as shown in Fig. 3.6.

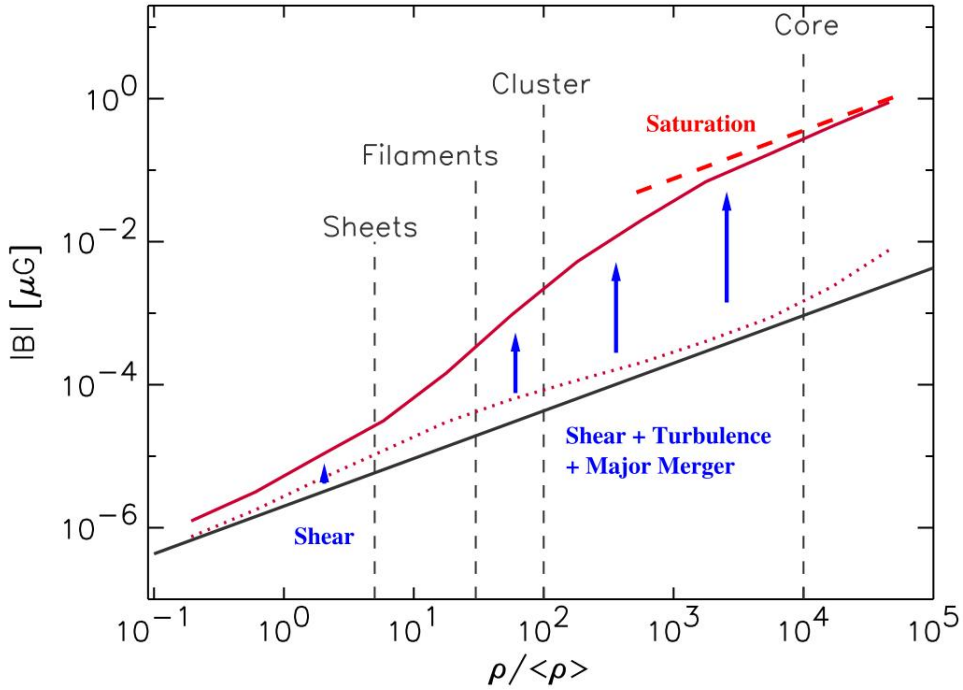

Figure 3.6: The strength of the magnetic field as a function of baryonic overdensity within a cosmological simulation (Dolag et al. 2008). The *straight line* shows the expectation for a purely adiabatic evolution, the *solid line* gives the mean field strength at a given overdensity within a cosmological simulation (Dolag et al. 2005b). While the latter is close to the adiabatic value in underdense regions, in clusters there is a significant inductive amplification due to shear flows and turbulence; this amplification however saturates in the cluster cores. At any given density, a large fraction of particles remains close to the adiabatic expectation, as shown by the *dotted line*, which gives the median of the distribution at each density.

Information on large scale magnetic fields evolution is also provided by numerical simulations (Fig. 3.7). In the past years, different codes were used to perform cosmological simulations involving magnetic fields (see e.g. Dolag et al. 2008 for a review). What emerges from simulations, assuming that a seed magnetic field exists before structure formation, is that the amplification occurring during cluster formation is highly non-linear. As a result, the final structure and strength of the field is totally driven by the formation process itself and the information on the initial seed is then lost. Such an approach indicates that studying large scale magnetic fields is an indirect way to investigate the microphysics that is described by the mechanisms driving structure formation.

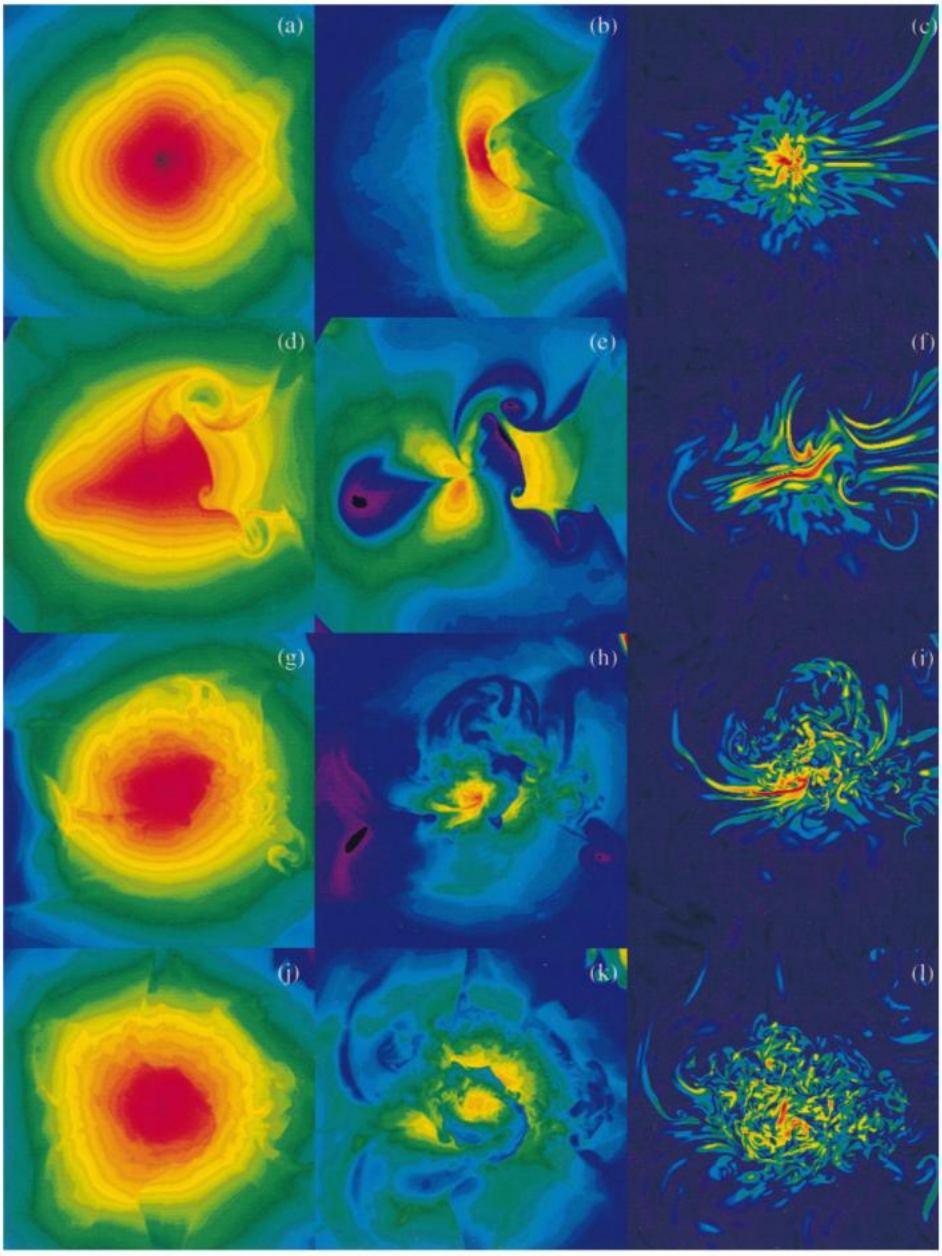

Figure 3.7: Three-dimensional numerical MHD simulation of magnetic field evolution in merging clusters of galaxies (Roettiger et al. 1999b). The evolution for different epoch ($t = 0, 1.3, 3.4$ and 5 Gyr from top to bottom) of gas temperature (*left column*), gas density (*central column*) and magnetic pressure (*right column*) in logarithmic scale in two dimensional slices through the cluster core are shown. Each panel is 3.75×3.75 Mpc.

Chapter 4

Constraining magnetic fields in radio relics

In order to constrain magnetic fields in radio relics we extend the method proposed by Markevitch et al. (2005) (Paragraph 3.5). First of all, we take into account possible projection effects to the relic transverse size by adding to the original approach a basic geometric model. Thanks to the availability of observations at different radio frequencies the geometry and the magnetic field of the region can both be simultaneously fixed.

The approach of Markevitch et al. (2005) considers that the particles accelerated at the shocks coincident with radio relics are advected in the downstream region and age by losing energy via synchrotron and IC emission. In addition, we evaluate two further aging models to fit the data:

- the first model takes into account the possibility that turbulence is produced in the downstream region. In this case, particles are subjected to a Fermi II-like energization, thus **re-acceleration** occurs;
- in the second model particles experience a **decaying magnetic field** while are advected downstream. In this case, the combination of IC and decrease of synchrotron losses leads to a different particle life-time with respect to the standard model by Markevitch et al. (2005).

4.1 A geometric model

The physical thickness of shocks is negligible. In a simple scenario where a radio relic is perfectly seen edge-on its thickness Φ_ν is totally due to the aging of the emitting particles advected downstream: $\Phi_\nu = V_d \tau_\nu$. However, in general, relics are observed at some angle θ between the surface of shock front and the plane of the sky and projection effects must be taken into account. For this reason we develop a geometric model that accounts for projection effects and that will be adopted in the subsequent analysis. A sketch of our view is shown in Fig. 4.1.

The observed thickness of the relic Φ_ν is due to the projection of the "surface" of the shock (that is frequency independent) and to the (projected) region covered downstream by the emitting electrons (that is frequency dependent)

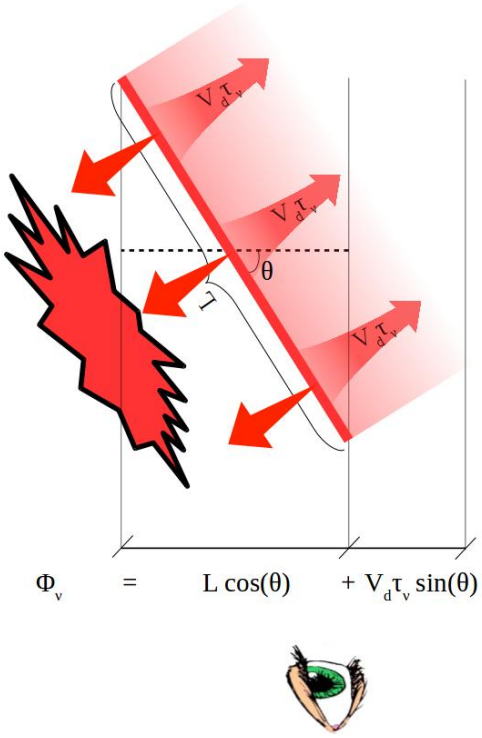

Figure 4.1: Geometric model adopted for the relic/shock that accounts both projection effects and aging.

$$\Phi_\nu = L\cos\theta + V_d\tau_\nu \sin\theta \tag{4.1}$$

where L is the size of the major axis of the relic (Fig. 4.1). Although the addition of the angle θ introduces a new free-parameter in the problem, we will show that multi-frequency observations can constrain it.

Our analysis requires estimates of the thickness of the relic. In this respect, we extract radial brightness profiles at various frequencies (see Chapter 5), where point sources (e.g. AGN) have been subtracted out as much as possible. Then, we evaluate the progressive broadening at lower and lower observing frequencies by measuring the FWHMs. This effect can be interpreted as due to the aging/advection of the downstream electrons.

Once the downstream velocity V_d is provided by X-ray data (see the next Paragraph), our model consists in fitting

$$\mathrm{FWHM}_\nu = L\cos\theta + V_d\tau_\nu \sin\theta \tag{4.2}$$

that provides a combined estimate of the life-time of the electrons emitting at different observing frequencies and of the position angle of the relic (τ_ν, θ).

The simplest aging model for relativistic particles that are cooling is due to (constant in space) synchrotron and IC losses. In this case, particle life-time is given by Eq. (3.8). Its combination with Eq. (4.2) and with the observed FWHM at different frequencies defines an "allowed" region in the (B, θ) plane that constrains a combination of magnetic field strengths and angles, as shown in Fig. 4.2. The effects of the different parameters on the contour regions are presented in Appendix A.

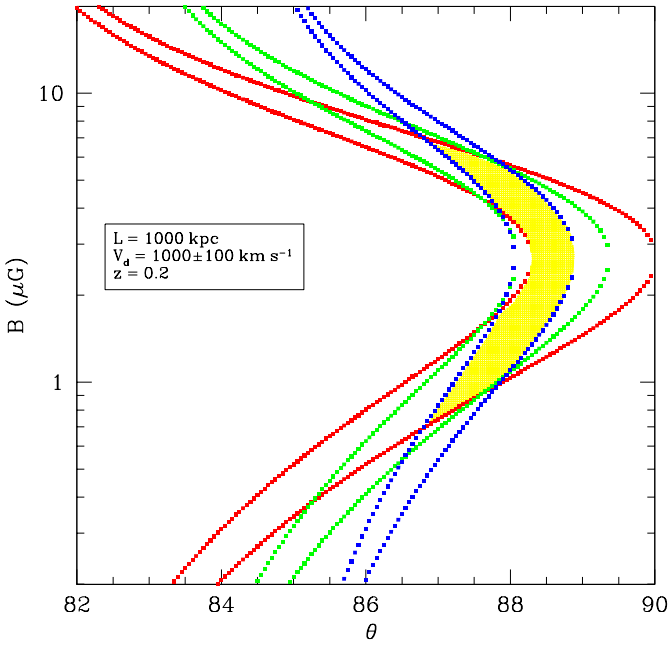

Figure 4.2: Magnetic field and angle contour regions for a mock radio relic (see panel for the parameters). Three frequencies are considered (color scheme: *red* for the low-frequency, *green* for the intermediate-frequency and *blue* for the high-frequency). The *yellow* region displays the "allowed" combination of (B, θ).

4.2 X-ray analysis of the shock

The model needs some ancillary quantities that can be obtained from X-ray observations of the shock. Shock strength can be characterized by its Mach number, that for a shock moving at speed V_{sh} is

$$\mathcal{M} = \frac{V_{sh}}{c_s}$$

where $c_s = (\partial p/\partial \rho)^{1/2}$ is the sound speed of the medium where the shock is moving into (p and ρ are its pressure and density, respectively). For an adiabatic perturbation ($p \propto \rho^{\Gamma}$, where Γ is the adiabatic index) it becomes

$$c_s = \sqrt{\frac{\Gamma k_B T}{\mu m_p}} \tag{4.3}$$

and since k_B is the Boltzmann constant, m_p is the proton mass and μ is the mean molecular mass of the considered gas (hereafter $\mu = 0.6$, which is a typical value for the ICM), c_s basically depends from the square root of temperature T of the unperturbed medium.

Once X-ray images and spectra are obtained and data analysis has been carried out, one can use the Rankine-Hugoniot jump conditions to relate the quantities upstream and downstream (subscripts u and d) of the shock (see e.g. Landau & Lifshitz 1959). For a generic gas with an adiabatic index Γ undergoing a shock with Mach number $\mathcal{M}$, the ratios in density ρ, velocity V, temperature T and pressure p are given by

$$\frac{\rho_d}{\rho_u} = \frac{(\Gamma-1)p_u + (\Gamma+1)p_d}{(\Gamma+1)p_u + (\Gamma-1)p_d} = \frac{(\Gamma+1)\mathcal{M}^2}{(\Gamma-1)\mathcal{M}^2+2},$$

$$\frac{V_d}{V_u} = \frac{(\Gamma+1)p_u + (\Gamma-1)p_d}{(\Gamma-1)p_u + (\Gamma+1)p_d} = \frac{(\Gamma-1)\mathcal{M}^2+2}{(\Gamma+1)\mathcal{M}^2},$$

$$\frac{T_d}{T_u} = \frac{p_d}{p_u}\left[\frac{(\Gamma+1)p_u + (\Gamma-1)p_d}{(\Gamma-1)p_u + (\Gamma+1)p_d}\right] = \frac{[2\Gamma\mathcal{M}^2-(\Gamma-1)][(\Gamma-1)\mathcal{M}^2+2]}{(\Gamma+1)^2\mathcal{M}^2}, \tag{4.4}$$

$$\frac{p_d}{p_u} = \frac{2\Gamma\mathcal{M}^2}{\Gamma+1} - \frac{\Gamma-1}{\Gamma+1}.$$

Adopting an adiabatic index for a monatomic gas ($\Gamma = 5/3$), the Mach number investigation can be performed by fitting the following formulas to temperature and density profiles extracted across the shock region

$$\frac{T_d}{T_u} = \frac{5\mathcal{M}_{kT}^4 + 14\mathcal{M}_{kT}^2 - 3}{16\mathcal{M}_{kT}^2}, \tag{4.5}$$

$$\frac{\rho_d}{\rho_u} = \frac{4\mathcal{M}_\rho^2}{\mathcal{M}_\rho^2+3}. \tag{4.6}$$

Typically, the density ratio is preferred in the Mach number investigation since the errors associated with the temperature measurements can be large, especially in the upstream region (see e.g. Markevitch & Vikhlinin 2007).

Additionally, surface brightness jumps can be used to infer the Mach number of the shock. However, since the dependencies of thermal X-ray emissivity on the density of the region where emission arises (see Eq. 1.1), this method substantially is an investigation of the underlying density profile. In this respect, the surface brightness profile is usually fitted with a model that consists in a broken power-law density profile

$$\begin{aligned} \rho_d(r) &= \mathcal{C}\rho_0\left(\tfrac{r}{r_{sh}}\right)^{a_1}, \quad \text{if} \quad r \le r_{sh} \\ \rho_u(r) &= \rho_0\left(\tfrac{r}{r_{sh}}\right)^{a_2}, \quad \text{if} \quad r > r_{sh} \end{aligned} \tag{4.7}$$

where $\mathcal{C} \equiv \rho_d/\rho_u$ is the compression factor of the shock, ρ_0 is the density normalization, a_1 and a_2 are the power-law indexes, r is the radius from the cluster center and r_{sh} is the radius corresponding to the putative shock front.

In order to apply our model, the downstream velocity V_d of the advected particles needs to be estimated (see Eq. 4.1). X-ray spectroscopy provides an estimate of T_u which leads to a measurement of the sound speed c_s upstream of the shock (see Eq. 4.3). The combination of the Mach number and the sound speed gives

$$V_d = c_s\frac{\mathcal{M}^2+3}{4\mathcal{M}} \tag{4.8}$$

and then all the required quantities are finally collected (in this equation $\Gamma = 5/3$).

To minimize the errors in the determination of V_d and thus in the relic measured thickness (see Eq. 4.2), precise measurements of T_u are required. However, shocks are typically located in the cluster outskirts where the gas density decreases (see e.g. Eq. 1.4) and so the X-ray brightness is small (see the dependencies of Eq. 1.1), leading to large errors in the determination of the upstream quantities, T_u in particular.

The problem of properly evaluating the temperature of the unperturbed region is a known issue. In this respect, the Rankine-Hugoniot condition for the temperature jump leads to circumvent such a difficulty: starting from the well measured downstream temperature and provided that the Mach number is determined from the density jump, Eq. (4.4) gives a better constraint on the upstream one.

As a final remark, we point out that the magnetic field involved in our approach refers to the downstream field, where the plasma is compressed, hence the field amplified. An estimate of the upstream magnetic field is given by

$$B_u = \mathcal{C}^{-1} B_d \,. \tag{4.9}$$

4.2.1 Limits to magnetic fields

The magnetic field estimates must unavoidably bump into the limits coming from (i) the relic (lack of) IC emission and (ii) the energy budget of the ICM magnetic field.

(i) The IC scattering between radio synchrotron electrons with the CMB photons produces emission in the HXR band (see Paragraph 2.5). By using X-ray analyses of shock in the soft X-rays one can infer a rough lower limit to the magnetic field of the relic region assuming that the population of the radio emitting electrons extends by a factor of $\sim 3-5$ below in energy following a power-law energy distribution. The power-law index can be inferred from radio observations. If a significant fraction, say $30-50\%$, of the X-ray brightness across a relic would be contributed by IC from the relic, this should be visible in the X-ray images and profiles. The absence of this feature results in a limit to the relic IC X-ray emission and thus to a lower limit to the magnetic field strength.

(ii) Further limits concerning magnetic fields in GCs arise from considerations about the energy budget of the ICM. Both observations and theoretical studies agree on the fact that magnetic field is not dynamically important in the ICM and represents a small fraction ($\lesssim 30\%$) of the thermal ones. In fact, if one compares the thermal energy density to that of the field

$$3 n_e(r) k_B T(r) = \frac{B(r)^2}{8\pi}$$

it should be

$$B(r) < \sqrt{3 n_e(r) k_B T(r) 8\pi f} \tag{4.10}$$

with $f \sim 0.3$. In oder to apply Eq. (4.10) an estimate of the thermal density profile $n_e(r)$, or at least of $p(r) = 2 n_e(r) k_B T(r)$, is required. We will compute limits on the magnetic field assuming that the field energy density is 10 and 30% of the local thermal energy density (i.e. at the position of the relic).

4.3 Particle life-time

As a first approximation, the relic size is given by $\Phi_\nu = V_d \tau_\nu$. The relic thickness at various frequencies thus depends on how particles age downstream. In this respect, we will consider three aging models.

The life-time τ_ν is affected by several physical processes that lead to energy losses and, in case, energy gains. The theoretical investigation of such mechanisms is useful to determine the particle break energy γ_b (i.e. the largest energy of electrons). Since the critical frequency $\nu_c \propto \gamma_b^2$ provides an observational quantity, models can be directly tested.

In the following, magnetic fields will be expressed in μG, times in Myr and ν_c in GHz. The observed (i.e. redshift-corrected) critical frequency thus is

$$\nu_c = 4.2 \times 10^{-9} B \gamma_b^2 (1+z)^{-1} \quad [\mathrm{GHz}]\,. \tag{4.11}$$

4.3.1 Standard scenario: IC and spatially constant synchrotron emission

Relativistic particles unavoidably lose energy through radiative losses. The time evolution of the energy of electrons undergoing synchrotron and IC losses is

$$\frac{d\gamma}{dt} = -6.0 \times 10^{-8} \left(B_{CMB}^2 + B^2\right) \gamma^2 \quad [\mathrm{Myr}^{-1}] \tag{4.12}$$

where an isotropic distribution for the scattering is assumed. Here, constant magnetic field B is considered.

In order to evaluate the break energy γ_b of the relativistic particles aging via radiative losses in a life-time τ, the following equation must be integrated

$$\int_\infty^{\gamma_b} \frac{d\gamma}{\gamma^2} = -6.0 \times 10^{-8} \int_0^\tau \left(B_{CMB}^2 + B^2\right) dt$$

where the left side integration lower limit formally is infinity. The integration leads to

$$\gamma_b = 1.7 \times 10^7 \left[\tau (B_{CMB}^2 + B^2)\right]^{-1}$$

hence the critical frequency (Eq. 4.11) results in

$$\nu_c = 1.2 \times 10^6 B \left[\tau (B_{CMB}^2 + B^2)\right]^{-2} (1+z)^{-1}\,. \tag{4.13}$$

The above equation represents the starting point of our work. Solving Eq. (4.13) in τ leads to the particle life-time already presented in Eq. (3.8). Particle life-time, hence the relic thickness, is $\Phi_\nu \propto \tau_\nu \propto \nu_c^{-1/2}$ in this "standard" simple scenario where only radiative losses are considered.

4.3.2 Re-acceleration scenario

Particle re-acceleration is a key processes in the physics of non-thermal phenomena in GCs. Turbulence is a Fermi II-like mechanism and seems to play a crucial point in powering radio halo sources (Paragraph 2.2.1). On the other hand, radio relics post-shocked regions are also ideal environments to produce significant turbulent motions.

We define the re-acceleration efficiency as $\chi = 1/t_{acc}$, where t_{acc} is the re-acceleration time. In this respect, the electron energy time evolution is described by

$$\frac{d\gamma}{dt} = -6.0 \times 10^{-8} \left(B_{CMB}^2 + B^2\right) \gamma^2 + \chi\gamma \quad [\mathrm{Myr}^{-1}]$$

that leads to

$$\gamma_b = 1.7 \times 10^7 \frac{\chi}{(B_{CMB}^2 + B^2)[1 - \exp(-\chi\tau)]}$$

and, at the end, to the critical frequency (Eq. 4.11)

$$\nu_c = 1.2 \times 10^6 B \left\{ \frac{\chi}{(B_{CMB}^2 + B^2)[1 - \exp(-\chi\tau)]} \right\}^2 (1+z)^{-1} .$$

Particle life-time for different t_{acc} and B is displayed in Fig. 4.3. Emitting particles increase their life-time as a consequence of being re-accelerated. Relic transverse sizes thus become broader with respect to the pure radiative losses model. This effect is more prominent at low frequencies, where re-accelerations more easily balance energy losses that are less strong. Since re-accelerations balance radiative losses for sufficient re-acceleration, particles can "freeze" their energy; that results in a vertical slope in the τ vs ν plot for the curves with short re-acceleration times (Fig. 4.3).

4.3.3 Decaying magnetic field

Plasma compression at the shock front leads to magnetic field amplification. Particles thus feel a progressively smaller magnetic field while they are advected downstream. This affects the electron life-time.

If we assume a magnetic field that is subjected to an exponential decay from a initial magnetic field strength B_0 (i.e the value at the shock location) and on a time-scale t_e

$$B(t) = B_0 \exp\left(-\frac{t}{t_e}\right)$$

the time evolution of electron energy is

$$\frac{d\gamma}{dt} = -6.0 \times 10^{-8} \left[B_{CMB}^2 + B_0^2 \exp\left(-\frac{2t}{t_e}\right)\right] \gamma^2 \quad [\mathrm{Myr}^{-1}]$$

that for long decay times ($t_e \to \infty$), i.e. a quasi-stationary magnetic field, it becomes the "standard" Eq. (4.12). Again, we must integrate

$$\int_\infty^{\gamma_b} \frac{d\gamma}{\gamma^2} = -6.0 \times 10^{-8} \int_0^\tau \left[B_{CMB}^2 + B_0^2 \exp\left(-\frac{2t}{t_e}\right)\right] dt$$

in order to obtain the break energy

$$\gamma_b = 1.7 \times 10^7 \left\{ B_{CMB}^2 \tau + \frac{B_0^2 t_e}{2} \left[1 - \exp\left(-\frac{2\tau}{t_e} \right) \right] \right\}^{-1} .$$

The critical emitting frequency (Eq. 4.11) results in

$$\nu_c = 1.2 \times 10^6 B_0 \exp\left(-\frac{\tau}{t_e} \right) \left\{ B_{CMB}^2 \tau + \frac{B_0^2 t_e}{2} \left[1 - \exp\left(-\frac{2\tau}{t_e} \right) \right] \right\}^{-2} (1+z)^{-1}$$

which does not imply the "standard" $\nu_c \propto \tau^{-1/2}$ but more complex scaling.

Particle life-time for different t_e and B_0 is displayed in Fig. 4.4. The life-time of electrons emitting at low frequency can either be shorter or longer than the "standard" case. This is due to the prevalence of IC on synchrotron losses and vice-versa. Two cases can be distinguished:

- for $B_0 < B_{CMB}$ synchrotron losses are always below IC emission which provides the main radiative process. This leads to shorter particle life-times (=narrower relic sizes) for electrons emitting at low frequencies with respect to the "standard".

- if $B_0 > B_{CMB}$ there is a time-period during the evolution of downstream electrons where synchrotron is the main cooling process. The decreasing of B with time implies that lower energy electrons, that have longer life-times, experience in such a period a magnetic field weaker than those at higher energies. This results in an increase of the thickness of the relic at lower frequencies that is larger than that expected in the "standard" case ($\Phi_\nu \propto \tau^{-1/2}$). This occurs till t_{cr}, i.e the time for which $B(t_{cr}) \sim B_{CMB}$. For $t > t_{cr}$ synchrotron contribution progressively fades and IC dominates the cooling resulting in faster aging of electrons emitting at frequency ν.

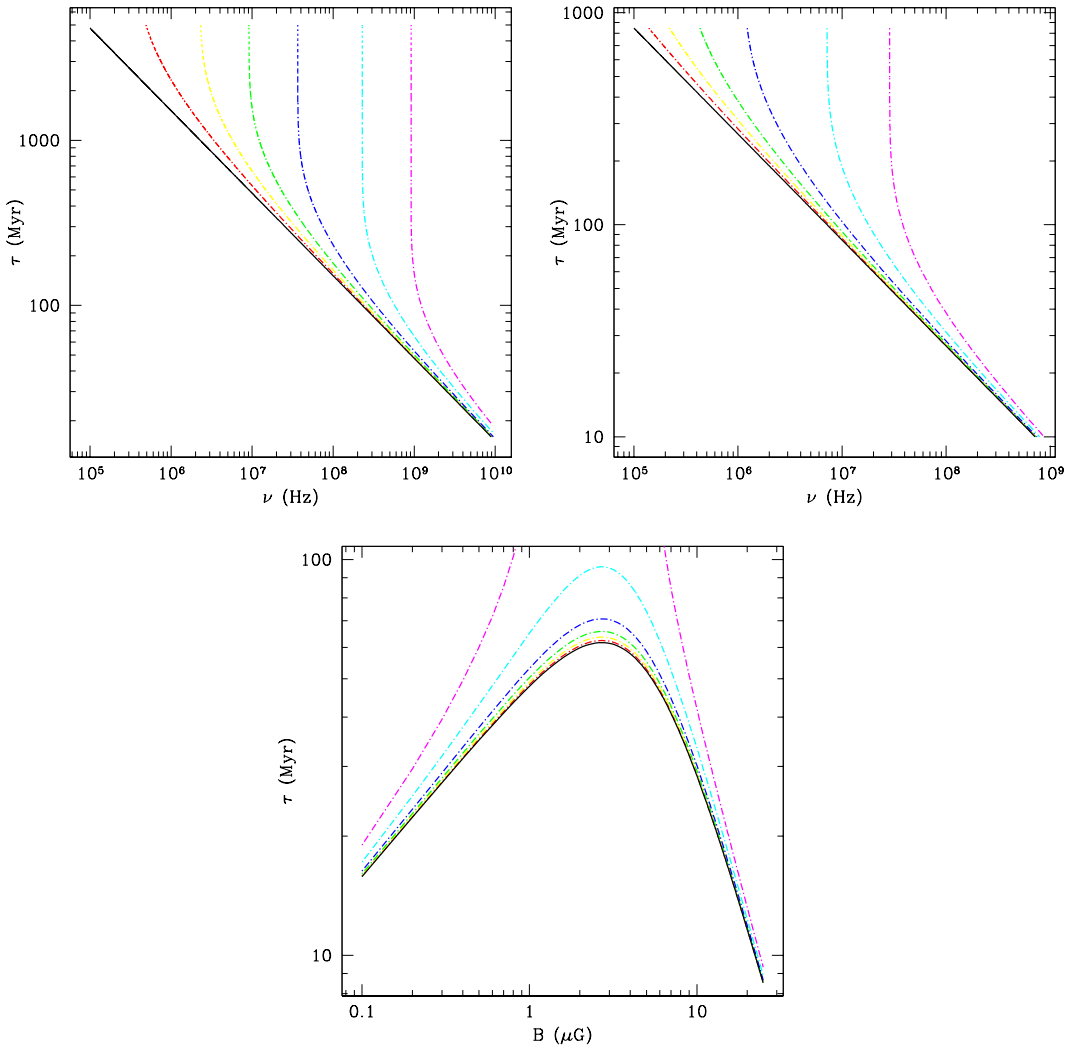

Figure 4.3: Comparison between the "standard" (*solid line*) and re-acceleration models (*dot-dashed lines*) with different t_{acc} (color scheme: *red* 2.5 Gyr, *yellow* 1 Gyr, *green* 500 Myr, *blue* 250 Myr, *cyan* 100 Myr and *magenta* 50 Myr). The equivalent magnetic field strength of the CMB was set to $B_{CMB} = 4.68\,\mu$G. *Top panels*: particle life-time as a function of the emitted frequency at fixed $B = 1\,\mu$G (*left*) and $B = 25\,\mu$G (*right*). *Bottom panel*: particle life-time as a function of the magnetic field strength at fixed emitted frequency $\nu = 1$ GHz.

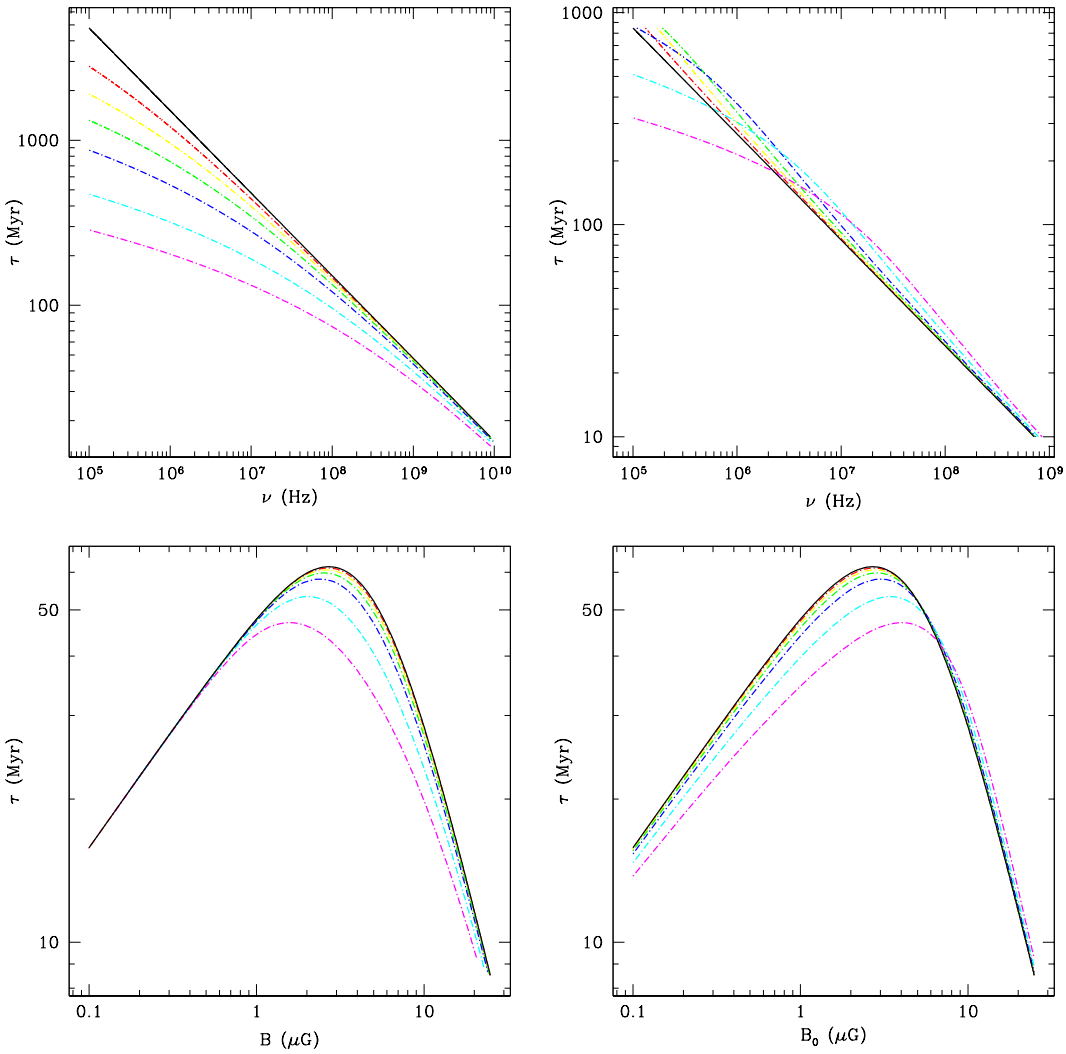

Figure 4.4: Comparison between the "standard" (*solid line*) and decaying magnetic field models (*dot-dashed lines*) with different t_e (color scheme: *red* 2.5 Gyr, *yellow* 1 Gyr, *green* 500 Myr, *blue* 250 Myr, *cyan* 100 Myr and *magenta* 50 Myr). The equivalent magnetic field strength of the CMB was set to $B_{CMB} = 4.68\,\mu$G. *Top panels*: particle life-time as a function of the emitted frequency at fixed $B_0 = 1\,\mu$G (*left*) and $B_0 = 25\,\mu$G (*right*). *Bottom panels*: particle life-time as a function of the magnetic field strength B (*left*) and of the initial magnetic field strength B_0 (*right*) at fixed emitted frequency of $\nu = 1$ GHz.

Chapter 5

Relic sample

In this Chapter we derive constraints on the magnetic field in radio relics applying the method discussed in the previous Chapter. We shall combine our estimations with the limits derived from the non-detection of relic IC emission in the X-rays and with considerations on the magnetic field energy budget at the relic location.

For a proper application of our simple geometric model, we need to select radio relics with specific characteristics. Particularly, the ideal sources must be:

- **nearly seen edge-on along the line-of-sight**, in order to have little projection effects. In this way, the thickness of the radio relic is mostly due to the aging of the emitting particles advected downstream;
- **almost regular in their morphology**, that is necessary to extract sharp radial surface brightness profiles;
- **observed at several radio frequencies**, to maximize the constraints on both the geometry and the magnetic field;
- **with good X-ray observations and analysis of the relic/shock region**, which are essential to obtain the main properties of the underlying shock.

Based on these requests, we selected three radio relics suitable for this kind of work. They are hosted in the clusters A 521, CIZA J2242.8+5301 and 1RXS J0603.3+4214. The main properties of the GCs are reported in Tab. 5.1.

Table 5.1: Properties of the clusters hosting the selected radio relics.

Name	RA_{J2000} (h, m, s)	Dec_{J2000} (°, ′, ″)	Redshift	L_X [a] ($erg\,s^{-1}$)	Scale [b] (″/kpc)
Abell 521	04 54 09.1	−10 14 19	0.247	8.0×10^{44}	3.875
CIZA J2242.8+5301	22 42 53.0	+53 01 05	0.192	6.8×10^{44}	3.197
1RXS J0603.3+4214	06 03 13.4	+42 12 31	0.225	1.0×10^{45}	3.619

[a] In the $0.1 - 2.4\,keV$ *ROSAT* band.

[b] A ΛCDM cosmology with $H_0 = 70\,km\,s^{-1}\,Mpc^{-1}$, $\Omega_m = 0.3$ and $\Omega_\Lambda = 0.7$ is adopted.

We perform our analysis using the best radio images and X-ray studies available so far. This is particularly critical in the case of the shock characterization through X-ray analysis, which is affected by several uncertainties and then represents an issue in our model (see Appendix A). Good radio maps at several frequencies are necessary to extract radial brightness profiles that are required to constrain the thickness of the relic at several frequencies. In order to properly choose the maps in which the profiles will be extracted, a preliminary image inspection must be done. One must pay attention in defining extracting regions avoiding discrete sources whose emission can be embedded to that of the relic. Possible contributions coming from other diffuse sources in the cluster (e.g. a radio halo) have also to be taken into consideration.

In radio, the ideal dataset should span the widest possible frequency range with adequate resolution and sensitivity to have a proper measurement of the relic physical properties. The radio images available for the three clusters/relics have been obtained with different instruments and softwares. Important, the used images must be (i) convolved at common resolution, (ii) transformed to the same coordinate system and (iii) corrected to the same projective geometry to correctly compare with each others. For these purposes we use the the tasks `CONVL` and `REGRD` of the package NRAO/AIPS.

In the following, we report results for the three GCs of the sample. We give a general introduction for each cluster, summarizing the main X-ray properties of the ICM and of the shock region. Afterwards, information on the diffuse radio emission is given. We mainly focus the attention on the radio relic sources, displaying their radial brightness profiles and the regions in which the measurements have been made. At the end of the Chapter we present the magnetic field constraints gathered from our method/approach by combining X-ray and radio observations for each relic.

5.1 Abell 521

A 521 is an X-ray luminous and massive cluster located at $z = 0.247$. Multiple merging episodes have occurred in this cluster whose X-ray properties are indicative of an object in a complex dynamical state (Arnaud et al. 2000; Ferrari et al. 2006). Further optical investigations confirm the merging nature of this cluster (Maurogordato et al. 2000; Ferrari et al. 2003). Recent *XMM-Newton* observations (Bourdin et al. 2013) suggest a highly disturbed ICM with the possible presence of a couple of cold fronts at the interface between the two main interacting sub-clusters and two shock fronts, one that is propagating to the eastern and another to the southwestern cluster outskirts.

At radio frequencies, A 521 hosts both a central radio halo and a peripheral relic. The former is barely detected at frequencies $\gtrsim 610$ MHz, becoming prominent below 327 MHz (Brunetti et al. 2008; Dallacasa et al. 2009; Giovannini et al. 2009). This halo is considered as the prototypical USSRH (see Paragraph 2.2). The relic is one of the best studied in the literature and it is one of the very few cases with a clear detection of an X-ray discontinuity coincident with the relic emission (Giacintucci et al. 2008; Bourdin et al. 2013).

5.1.1 X-ray analysis

A 521 was studied in the X-rays with different satellites in the course of the last years: *ROSAT* and *ASCA* (Arnaud et al. 2000), *Chandra* (Ferrari et al. 2006) and

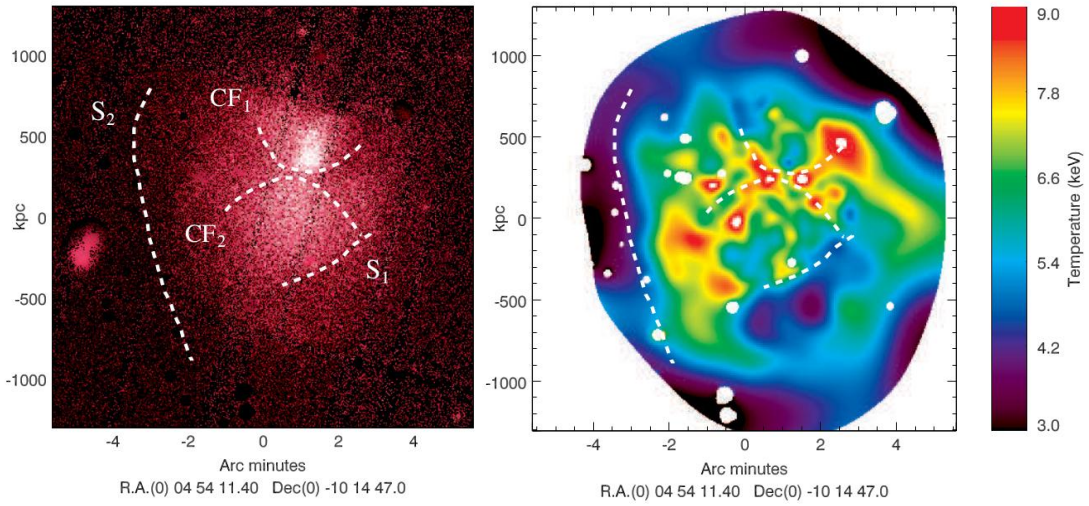

Figure 5.1: *XMM-Newton* observations of A 521 (Bourdin et al. 2013). *Left panel*: surface brightness map in the $0.5-2.5\,\mathrm{keV}$. The two cold fronts CF_1 and CF_2 and the shocks S_1 and S_2 (spatially coincident with the radio relic emission) are indicated. *Right panel*: ICM temperature map obtained from wavelet spectral imaging.

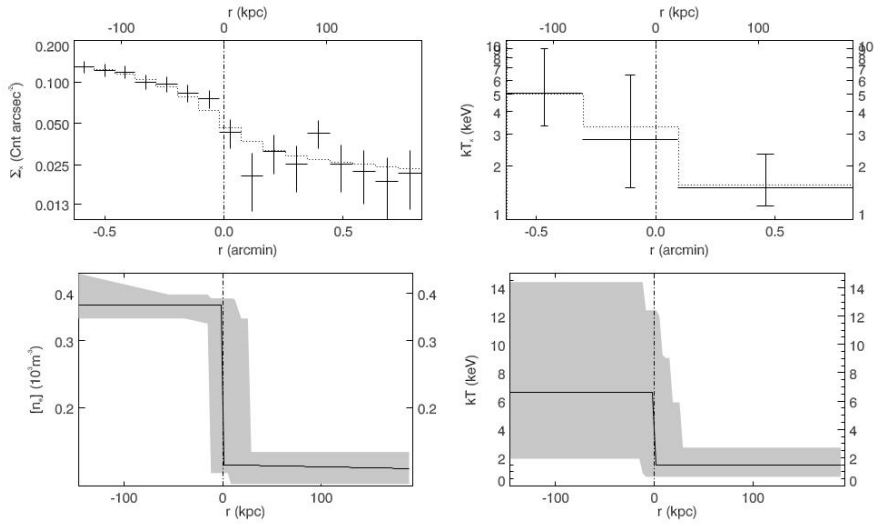

Figure 5.2: Projected brightness and temperature profiles (*top panels*) and 3D modeled ICM density and temperature profiles (*bottom panels*) across the brightness jump S_2 shown in Fig. 5.1 (Bourdin et al. 2013).

XMM-Newton (Bourdin et al. 2013). All of these analyses provide evidence of irregular morphology of the ICM distribution, indicative of the ongoing multiple mergers present in this structure. The emission and temperature maps of such a system (Fig. 5.1) both confirm a strongly substructured ICM in the cluster.

Early X-ray images revealed two central brightness clumps that have been interpreted as due to the central part of the main cluster and to a northern in-falling group, centered on the BCG (Arnaud et al. 2000). These correspond to the two bow-shaped brightness jumps found by Bourdin et al. (2013), labeled as CF_1 and CF_2 in Fig. 5.1, whose temperature features lead to identify them as cold fronts. Optical studies (Ferrari et al. 2003) also confirm the scenario of a northern merging event and provide evidence of multiple merger processes at various stages. Detailed *Chandra* observations further prove the presence of several sub-clusters and groups of galaxies converging towards the center of the cluster (Ferrari et al. 2006).

An interesting edge revealed in the X-ray images in the southeastern region of A 521, i.e. where the radio relic is located, raised the possibility that a shock front due to one of the recent merger episodes occurred in this cluster could be present (Giacintucci et al. 2008). Bourdin et al. (2013) confirmed its presence at the same time with another shock, S_1, in the western outskirts. These features, together with the cold fronts above mentioned, are shown in Fig. 5.1.

The properties of the shock coincident with the radio relic (labeled as S_2 in Fig. 5.1) were investigated in detail in Bourdin et al. (2013). They adopted a spherical model for the ICM distribution and derived with good accuracy a Mach number $\mathcal{M}_\rho = 2.42 \pm 0.19$ via density jump (Fig. 5.2), that is consistent with that expected from the radio spectrum of the radio relic (Giacintucci et al. 2008) under the assumption of DSA (see Paragraph 2.1.1). They also determined a Mach number through temperature jump $\mathcal{M}_{kT} = 3.4^{+3.69}_{-1.92}$. However, this estimate is not as accurate as the one coming from the density jump and underlines the difficulties of X-ray analyses of shock regions. In Tab. 5.8 the values found in Bourdin et al. (2013) relevant for our purposes are reported.

5.1.2 Radio analysis

The merging nature of the system is also in line with the presence of diffuse radio synchrotron sources in the cluster. In fact, A 521 host both a radio halo and a radio relic. Their synchrotron emission properties make this cluster a special laboratory in the understanding of (radio) non-thermal phenomena in GCs.

The detection of the giant radio halo in A 521 was difficult because of its extreme spectral properties. In fact, the average value of its spectral index in the range between 147 MHz and 1.4 GHz is $\alpha \sim 1.85$ (Macario et al. 2013), much steeper than the usual value of other radio halos (see Paragraph 2.2). This makes the radio emission at higher frequencies very faint. In fact, the halo was originally detected below 610 MHz, becoming clearly visible only at frequencies lower than 327 MHz (Brunetti et al. 2008). Only deep follow-up observations provided a firm detection at 1.4 GHz (Dallacasa et al. 2009), where the majority of radio halos has been discovered with the *VLA*.
The very steep spectrum of this halo leads to identify it as the prototype USSRH. This result is very important in framework of particle acceleration in GCs. In fact, together with the hint of spectral curvature (Brunetti et al. 2008; Dallacasa et al. 2009), it supports the idea that turbulence plays an important role in the acceleration of relativistic

particles in clusters and rules out secondary acceleration scenarios (Brunetti et al. 2008).

The radio relic in A 521 is located in the south-eastern peripheral part of the cluster, at the boundary of the ICM X-ray emission, at a projected distance of ~ 930 kpc. The morphology of the source is arc-shaped and highly elongated (~ 1 Mpc).

This relic is one of the best studied in the literature, with several observations available at different radio frequencies (Giacintucci et al. 2008; Macario et al. 2013). It is detected up to 5 GHz and at low frequencies it becomes confused with the progressively more dominant emission from the radio halo. The numerous flux density measures of this source lead to an overall spectrum in the range 153 MHz – 5 GHz that is well fitted by a single power-law with spectral index $\alpha = 1.45 \pm 0.02$ (Macario et al. 2013).

The synchrotron radio spectral index measured at the edge of the relic (i.e. the injection spectrum) and the Mach number are consistent with an origin of the emitting electrons based on DSA theory. Moreover, the inferred Mach number from radio data $\mathcal{M}_{\rm radio} = 2.27 \pm 0.02$ (see Eq. 2.1) is in excellent agreement with that derived from X-ray analysis (Bourdin et al. 2013). Important, Giacintucci et al. (2008) reported also evidence of a spectral steepening with distance from the edge of the relic that suggests aging of the emitting electrons in the downstream region.

Relic radial brightness profiles

In order to measure the radio brightness profiles of the relic, we used images at 327 MHz, 610 MHz and 1.4 GHz, published by Giacintucci et al. (2006), whose main properties are summarized in Tab. 5.2. We convolved all the maps at the same resolution of $16'' \times 16''$.

Table 5.2: Properties of the used radio maps.

Frequency (MHz)	rms (μJy beam^{-1})	Original HPBW ($'' \times ''$)	Instrument
327	90	15.0×12.0	*GMRT*
610	50	13.1×8.2	*GMRT*
1410	20	15.0×12.0	*VLA*

The radial brightness profiles have been extracted from two combined arc-shaped regions (with the same curvature radius) in order to avoid the bright source on the relic eastern edge, clearly visible as a knot over the sharp front of the radio emission (Fig. 5.3). The northern part of the relic has been excluded from the analysis for its patchy structure and for the possible contamination from emission of the radio halo at 327 MHz. For this reason, we also do not use the observations at 247 MHz and 147 MHz that were available at the epoch of this Thesis. The highest frequency available, at 5 GHz, has also been excluded because the patchy structure of the relic at such a frequency, mostly arising from inadequate *uv*-sampling of the short spacings.

The used radio images and the extracting regions are shown in Fig. 5.3 whereas the brightness profiles of the relic obtained at various frequencies are presented in Fig. 5.4 and in Tab. 5.3.

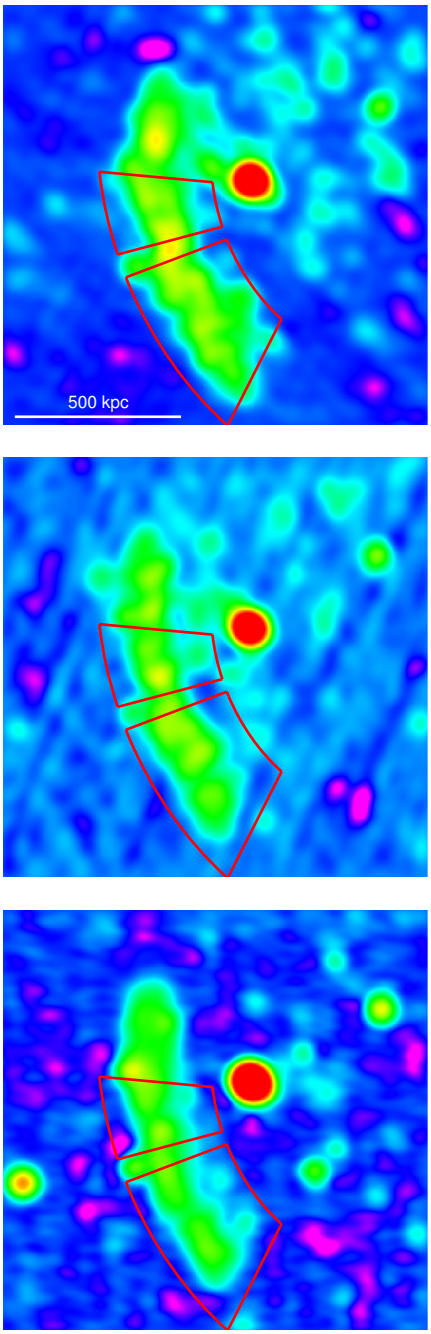

Figure 5.3: From top to bottom, 327 MHz, 610 MHz (*GMRT*) and 1.4 GHz (*VLA*) common resolution images of the radio relic in A 521. The radial profiles of Fig. 5.4 have been extracted from the two combined arc-shaped regions avoiding discrete sources.

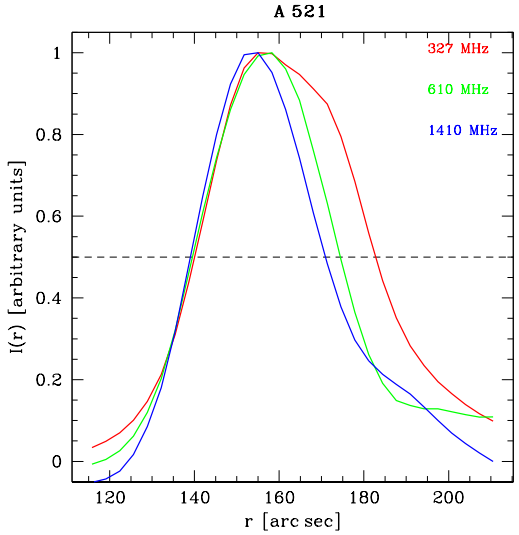

Figure 5.4: Normalized radial brightness profiles of the relic measured at different frequencies (see panel). The horizontal *dashed line* at $I(r) = 0.5$ helps in the comparison between the FWHMs at various frequencies, whose are computed in Tab. 5.3.

Table 5.3: Deconvolved FWHMs of the relic in A 521 at different frequencies. Uncertainties on the FWHMs are generally assumed as a fraction of the beam size, which we conservatively assumed 15%.

Frequency (MHz)	FWHM (kpc)
327	153.8
610	120.6
1410	106.1

5.2 CIZA J2242.8+5301

CIZA J2242.8+5301 (hereafter CIZA J2242) is a merging cluster of the Cluster In Zone of Avoidance (CIZA) survey located at $z = 0.1921$. It hosts several diffuse radio sources but its most remarkable feature certainly is the extremely narrow northern relic (van Weeren et al. 2010) which long arc-shaped morphology led to its nickname: "Sausage" relic. A fainter counter relic is also detected in the southern part of the cluster, possibly indicating the occurrence of a recent head-on merger (Roettiger et al. 1999a).

In order to understand the "Sausage" peculiarities, numerical simulations have been performed to investigate the geometry of the merger (van Weeren et al. 2011) and the possible DSA origin of the relic (Kang et al. 2012). Furthermore, observations at several different radio frequencies allowed a well detailed study of the synchrotron spectrum of the "Sausage" (Stroe et al. 2013, 2014a)

Three X-ray analyses of CIZA J2242 have been conducted so far. *XMM-Newton* study (Ogrean et al. 2013a) provides the first evidence of the complex distribution of the ICM. Although an N-S elongation of the X-ray emitting gas is likely consistent with the merger axis suggested by the double radio relic hosted in this GC, X-ray images suggest a more complex merger scenario than those inferred by numerical simulations (van Weeren et al. 2011). *Suzaku* analysis (Akamatsu & Kawahara 2013) claims a temperature jump at the location of the "Sausage" relic that is spatially coincident with one of the four brightness surface discontinuities found by *Chandra* (Ogrean et al. 2014).

5.2.1 X-ray analysis

Early *ROSAT* observations of CIZA J2242 provided evidence of disturbed and N-S elongated morphology of the ICM distribution (Voges et al. 1999). Such features are also observed in more recent *XMM-Newton* data (Ogrean et al. 2013a) which confirm a merging nature for this cluster, as shown in Fig. 5.5.

The presence of the extraordinary "Sausage" relic in the northern part of the cluster leads to several X-ray observational campaigns aimed in the search of a shock coincident with the relic source. In fact, spectral analysis of the "Sausage" radio emission leads to $\mathcal{M}_{\rm radio} \sim 4.6$ (see Eq. 2.1) (van Weeren et al. 2010), which should be easily detectable with currently operating satellites. Nevertheless, first X-ray study of CIZA J2242 (Ogrean et al. 2013a) failed in the detection of such a feature. However, this was probably due to the high *XMM-Newton* instrumental background which likely prevented any characterization of the northern relic region. In fact, *Suzaku* observations (Akamatsu & Kawahara 2013) lead to identify a temperature drop of a factor of ~ 3 across the "Sausage" (Fig. 5.6) although no surface brightness jump has been found, probably because of *Suzaku* low angular resolution. Further, more better resolution images with *Chandra* (Ogrean et al. 2014) confirm the temperature jump in the northern relic region and reveal a weak surface brightness discontinuity ($< 2\sigma$ detection) across it. Three more surface discontinuities located both on and off the merger axis are also identified in the inners of CIZA J2242 (Ogrean et al. 2014). The nature of such features is still difficult to explain because any temperature characterization of these regions could be done.

Despite the Mach number inferred by radio data analysis (van Weeren et al. 2010), X-ray results seem to indicate a significantly lower value for this shock (Akamatsu &

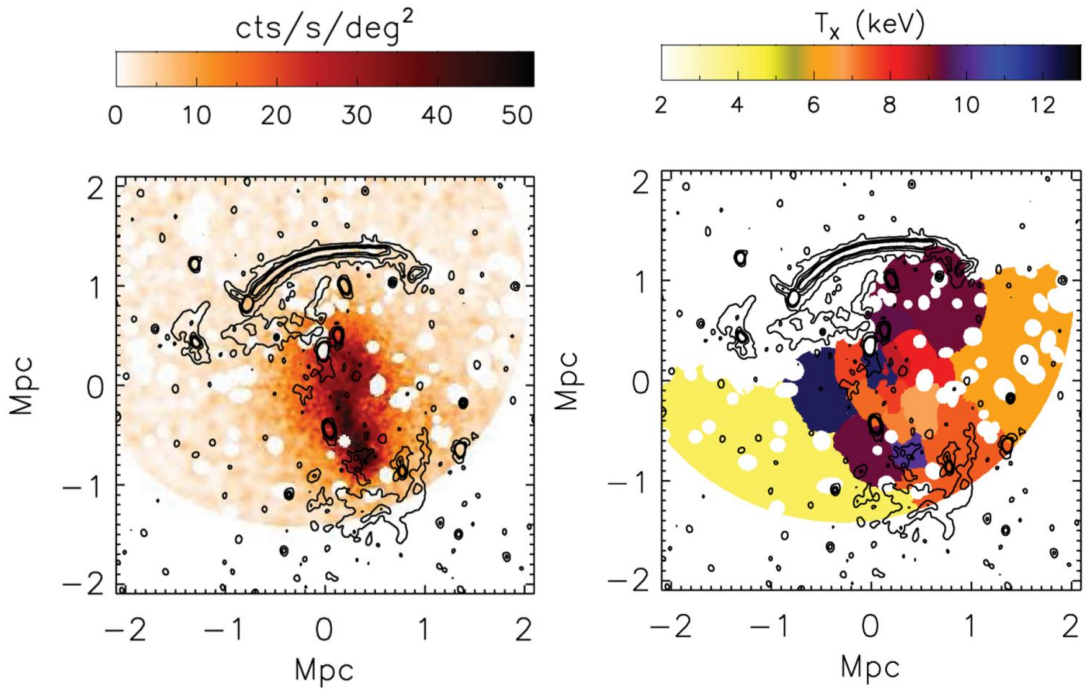

Figure 5.5: *XMM-Newton* observations of CIZA J2242 (Ogrean et al. 2013a). *Left panel*: surface brightness map in the $0.5-4\,\mathrm{keV}$ band (colors). *Right panel*: ICM temperature map (colors). In both panels *WSRT* radio contours at 1.4 GHz are overlaid.

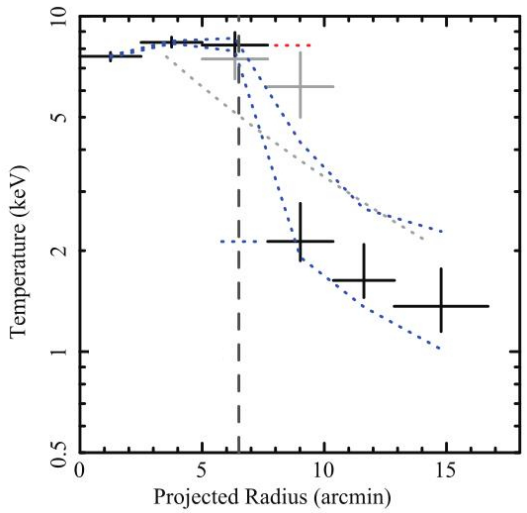

Figure 5.6: X-ray temperature profile of the "Sausage" relic in CIZA J2242 (Akamatsu & Kawahara 2013). Vertical *dashed line* indicates the position the radio relic. *Gray dotted line* indicates the "universal" temperature profile expected from the scaled temperature profile (Burns et al. 2010). The *red* and *blue horizontal bars* show the pre and post shock quantities used to derive the Mach number.

Kawahara 2013; Ogrean et al. 2014). We use the measurements obtained by *Suzaku* observations (Akamatsu & Kawahara 2013) for our analysis, which lead to a Mach number $\mathcal{M}_{kT} = 3.15^{+0.66}_{-1.31}$ estimated through temperature jump (Fig. 5.6). A compilation of Mach number derived values for this relic is given in Tab. 5.8.

5.2.2 Radio analysis

The CIZA J2242 cluster hosts several diffuse non-thermal sources at the radio wavelengths (Stroe et al. 2013). The undisputed main actor of these is the "Sausage" relic (Fig. 2.4), located at a distance of ~ 1.5 Mpc from the cluster center, which is a unique case of radio relic because its extreme morphology: a length of ~ 2 Mpc versus a very narrow thickness (van Weeren et al. 2010).

Several observations have been performed at the radio frequencies and the relic has been observed from 153 MHz (*GMRT*, Stroe et al. 2013) to 16 GHz (*AMI*, Stroe et al. 2014b). It is the only case so far of a relic detection above 5 GHz.

The availability of several flux density measures over a wide range of frequencies leads detailed studies on both the overall and the radial synchrotron spectrum. Van Weeren et al. (2010) reported a spectral index at the front of the relic of 0.6 ± 0.05 while Stroe et al. (2014a) determine a significantly steeper value of $0.77^{+0.03}_{-0.02}$. Such a discrepancy can be explained by convolution effects. The radio injection spectral index leads to a Mach number estimation based on DSA of $\mathcal{M}_{\rm radio} \sim 4.6$ that is inconsistent with X-ray observations (Akamatsu & Kawahara 2013).

Radial spectral analyses in the downstream region provide evidence of spectral curvature over the entire length of the relic (van Weeren et al. 2010; Stroe et al. 2013), as shown in Fig. 2.4. This effect is due to synchrotron and IC losses that cause a cutoff at the high frequency part of the emission spectrum after particles acceleration at the shock.

The integrated spectrum from 153 MHz to 2.3 GHz is well described by a single power-law with slope 1.06 ± 0.05 (Stroe et al. 2013). The flux density measurement at 16 GHz seems robust and it plays an important role in the understanding of the origin of radio relics. Nowadays, any relic formation mechanism can describe the high-frequency steepening. Considering such a measurement, the spectral index results indeed in $\alpha^{16\,\rm GHz}_{153\,\rm MHz} = 1.33 \pm 0.03$ (Stroe et al. 2014b) but fails in the description of the higher frequency data, which is 12σ below the predicted value. For this reason new theoretical models have to be developed in order to explain this particular feature of the "Sausage".

On the opposite side of the cluster, a smaller counter relic is detected. It does not exhibit the same well defined structure of the "Sausage" and results in a rough bow shaped morphology. Double relics have been observed in different GCs (see Paragraph 2.1) and are considered as the main proof of large shock waves propagating outward the ICM generated by head-on collision between two roughly equal-mass clusters (Roettiger et al. 1999a). For this reason, the merger scenario has been investigated through numerical simulations (van Weeren et al. 2011) in order to constrain the geometry and the mass ratio of an idealized binary merger. The simulations found that the relics are compatible with a scenario in which they are seen close to edge-on and have been generated in a merger with mass ratio of the components of about 2:1 occurred bout 1 Gyr ago.

A further indication of a shock origin comes from the polarization study of the "Sausage". It demonstrates a high level of polarization, up to 60%, indicating a well-ordered magnetic field with the polarization magnetic field vectors aligned with the relic (Fig. 2.4) as a consequence of plasma compression (van Weeren et al. 2010). Remarkably, this high polarization value can only be explained if the relic is nearly seen edge-on (Enßlin et al. 1998).

Relic radial brightness profiles

We used the radio images at 323 MHz, 610 MHz, 1.4 GHz, 1.7 GHz and 2.3 GHz, published by Stroe et al. (2013), whose main properties are summarized in Tab. 5.4. We convolved all the maps at the same resolution of $21'' \times 21''$.

Table 5.4: Properties of the used radio maps.

Frequency (MHz)	rms (μJy beam^{-1})	Original HPBW ($'' \times ''$)	Instrument
323	250	12.3×11.3	*GMRT*
610	40	6.9×5.1	*GMRT*
1382	70	21.0×15.8	*WSRT*
1714	40	16.0×13.1	*WSRT*
2272	50	12.2×10.0	*WSRT*

As already mentioned, the "Sausage" relic is very sharp and regular in morphology; this easily allows to choose the region/s where the radial brightness profiles will be extracted. The only irregularities of such a structure emerge at both the ends of the relic. Furthermore, on the western edge a discrete source is present (Fig. 5.7). For this reason, external parts of the relic have been excluded in our analysis.

Despite its remarkably narrow and arc-shaped morphology, a deeper look at the "Sausage" reveals that the front of the relic can not be described by a single curvature radius but at least two of them are required to reproduce its shape. For this reason, we divided the relic into eastern (`E`) and western (`W`) parts and we extracted the radial profiles in these different regions, as shown in Fig. 5.7. The brightness profiles of the relic obtained at various frequencies are presented in Fig. 5.8 and we report the FWHMs measured at the different frequencies in Tab. 5.5. These support our decision to distinct two different regions of the relic; in fact, slightly broader FWHMs are systematically measured for the `W` part of the source.

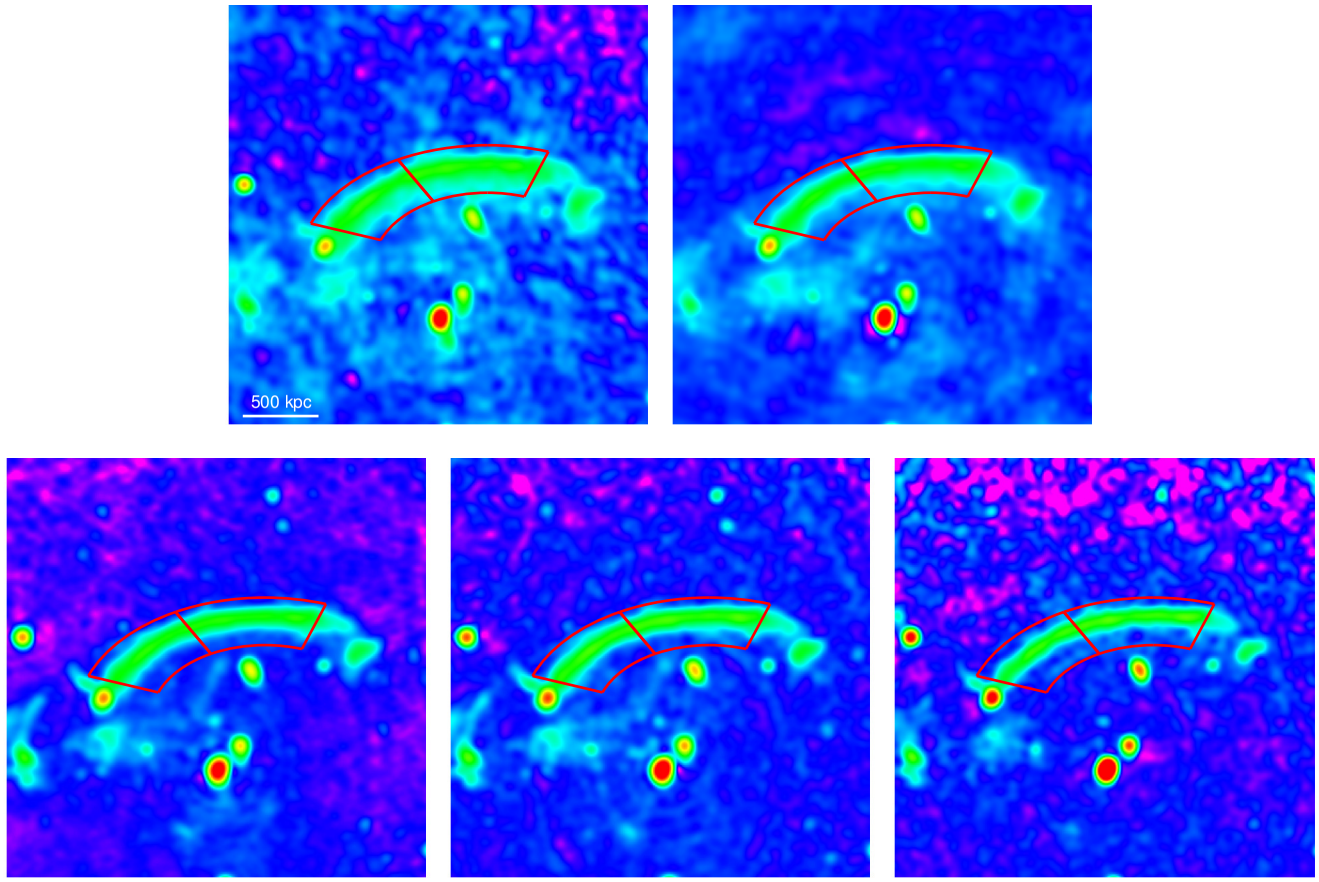

Figure 5.7: From left to right and from top to bottom, 323 MHz, 610 MHz (*GMRT*) and 1.4 GHz, 1.7 GHz and 2.3 GHz (*WSRT*) common resolution images of the "Sausage" relic. The radial profiles of Fig. 5.8 have been extracted from the two different arc-shaped regions avoiding discrete sources.

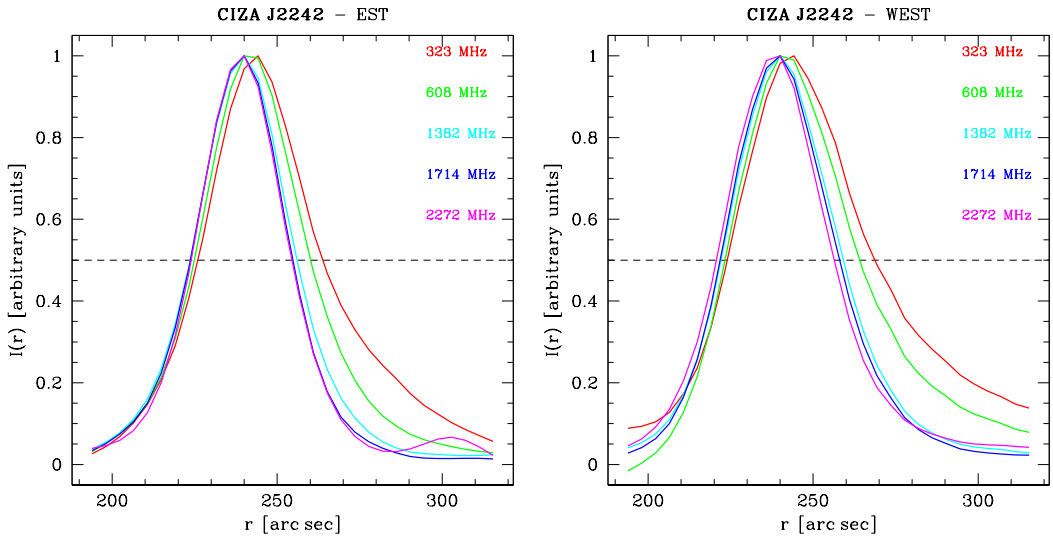

Figure 5.8: Normalized radial brightness profiles of the relic measured at different frequencies (see panels) in the `E` and `W` regions (Fig. 5.7). The horizontal *dashed line* at $I(r) = 0.5$ helps in the comparison between the FWHMs at various frequencies, whose are computed in Tab. 5.5.

Table 5.5: Deconvolved FWHMs of the "Sausage" relic for the `E` and the `W` regions at different frequencies. Uncertainties on the FWHMs are generally assumed as a fraction of the beam size, which we conservatively assumed 15%.

Frequency	FWHM	
	`E`	`W`
(MHz)	(kpc)	(kpc)
323	100.8	125.4
610	90.8	111.5
1382	78.5	97.5
1714	73.3	94.1
2272	71.4	92.5

5.3 1RXS J0603.3+4214

1RXS J0603.3+4214 (hereafter 1RXS J0603) is a cluster recently discovered by van Weeren et al. (2012) located at $z = 0.225$. Several multi-wavelength observations of this GC have been performed. In the radio band, the cluster hosts three relics and a halo.

The main peculiarity of this cluster is undoubtedly the large and bright northern relic (see Fig. 5.9). It has an unusual linear morphology, with a broader part to the west, that led to its nickname: "Toothbrush" relic. Detailed radio spectral analysis of this source has been reported in van Weeren et al. (2012). Recently the "Toothbrush" has been the target of *LOFAR* observations (van Weeren et al. 2015) as one of the targets of the *LOFAR* Survey Key Project.

The cluster 1RXS J0603 has also been investigated in the X-rays. *XMM-Newton* observations provide evidence for a recent merger activity and three density and temperature discontinuities have been reported in Ogrean et al. (2013b), suggesting the presence of shocks in the ICM. However, the characterization of the shocks is still controversial, as demonstrated by recent *Chandra* observations (van Weeren et al. 2015). In the X-rays, the structure of the cluster is very complicated and numerical simulations (Brüggen et al. 2012) failed in providing a clear explanation of the cluster dynamics. At the same time, the structure of the relic suggests a complex triple merger.

5.3.1 X-ray analysis

Few X-ray observations of 1RXS J0603.3 exist so far. The cluster was detected as an extended source in the *ROSAT* All Sky Survey, which provided the first indication of a north-south elongation of the ICM emission (van Weeren et al. 2012). The extended morphology and the high X-ray luminosity (Tab. 5.1) are consistent with a massive cluster undergoing a major merger event.

The first detailed X-ray investigation of the cluster was performed by Ogrean et al. (2013b) using *XMM-Newton* data. They confirmed the disturbed state of the system revealing two emission clumps in the northern and southern parts of the cluster (Fig. 5.9). These features are connected by a bridge of emission.

The attention of the X-ray analysis was mainly focused to the northern part of the cluster, where the "Toothbrush" relic stands out. Ogrean et al. (2013b) claimed at least three weak ($\mathcal{M} \lesssim 2.5$) shock features in 1RXS J0603.3. Their asymmetric locations with respect to the merger axis (the imaginary line connecting the two cluster cores) indicate a merger with a non-zero impact parameter. The northern shock, i.e. the shock that is expected to trace the "Toothbrush", is puzzling. In fact, (i) it is visible only along the broadest part of the relic, (ii) it is not coincident with the outer edge of the relic and (iii) it extends more than 0.5 Mpc beyond its western boundary. The Mach number of this shock was estimated by fitting surface brightness profiles taken in different regions across the relic, resulting in $\mathcal{M} \sim 1 - 2.5$, depending on the region.

Recently, *Chandra* observations aimed at obtaining better constraints on the shock in the "Toothbrush" region were performed by van Weeren et al. (2015). The overall *Chandra* view (imaging and temperature map) of 1RXS J0603.3 is shown in Fig. 5.9. The X-ray morphology of the cluster is very disturbed, showing a clear bi-modality and a bridge connecting the two cores. The temperature map reveals a high-temperature region (~ 15 keV) in the southern part of the cluster.

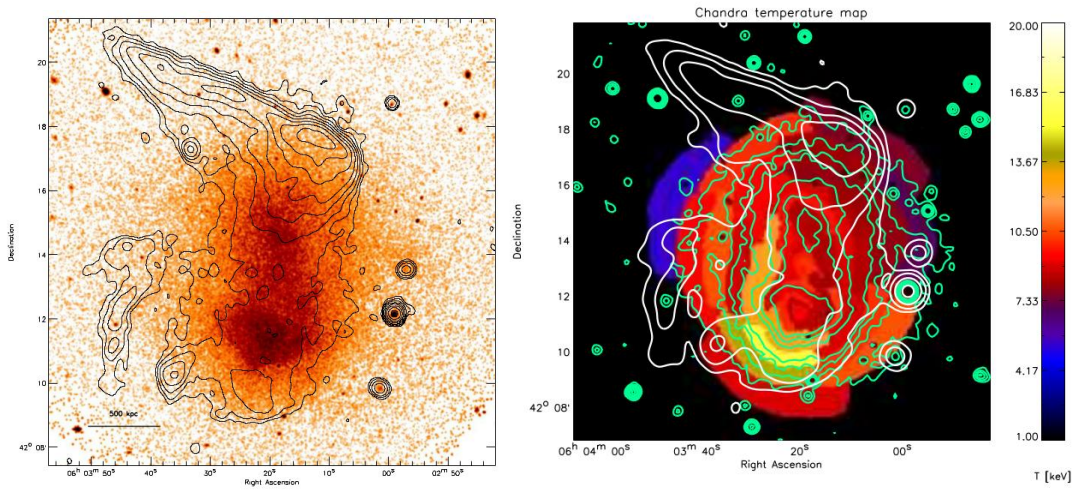

Figure 5.9: *Chandra* observations of 1RXS J0603.3 (van Weeren et al. 2015). *Left panel*: surface brightness map in the $0.5-2\,\mathrm{keV}$ band (colors). *Right panel*: ICM temperature map (colors). In both panels *LOFAR* radio contours at $120-181\,\mathrm{MHz}$ are overlaid. The "Toothbrush" relic appears as an elongated structure in the northern part of the cluster.

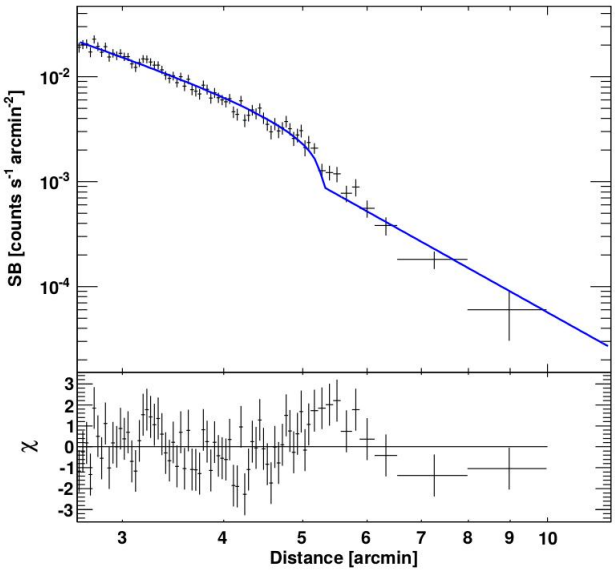

Figure 5.10: X-ray surface brightness profile across the broadest part of the "Toothbrush" relic. The *blue line* shows the best fitted broken power-law density model assumed for the shock (van Weeren et al. 2015).

The relic-shock analysis with *Chandra* leads to a different interpretation with respect to the *XMM-Newton* data. In fact, the position of the shock determined by *Chandra* (van Weeren et al. 2015) differs from that determined by *XMM-Newton* (Ogrean et al. 2013b) and is consistent with the outer edge of the relic. Still the measurement of the Mach number of the shock came up to be problematic. Indeed, X-ray data suggest the presence of a very weak shock $\mathcal{M}_{\rm SB} \sim 1.5$, as obtained by fitting a broken power-law density model (Eq. 4.7) to the surface brightness profile (Fig. 5.10) taken across the broadest relic region. Fore sake of clarity, in Tab. 5.8 a summary of van Weeren et al. (2015) shock analysis is reported.

5.3.2 Radio analysis

Non-thermal phenomena are present in different flavors in 1RXS J0603.3: three radio relics and an elongated radio halo have been identified in such a system (van Weeren et al. 2012). The main radio-feature of the cluster is the northern, bright and large "Toothbrush" relic. As its name suggests, the relic exhibits a peculiar morphology, showing a narrow and straight western part which suddenly broaden (Fig. 5.11). It is one of the largest relics observed, with a major axis of ~ 2 Mpc.

Brüggen et al. (2012) investigated the "Toothbrush" through numerical simulations. Their triple merger model, assuming a main N-S major event with a third less massive substructure moving in from the S-E, is able to reproduce (i) the length of the relic, (ii) its shape and (iii) the angle with respect to the major axis of the X-ray emission.

At the cluster center, radio observations reveal the presence of an elongated radio halo. Its emission recalls the X-ray morphology of the cluster (Fig. 5.9) and extends up to the broadest part of the northern relic. The sources are indeed connected by a region with $\alpha \gtrsim 2$ that flattens to $\alpha \sim 1.2$ towards the cluster center. This led van Weeren et al. (2012) to speculate that the relativistic particles that are accelerated at the shock may be re-accelerated by merger driven turbulence and form the halo. Overall, the spectral index of the halo results in $\alpha \sim 1.15$ in the 74 MHz $-$ 4.9 GHz (van Weeren et al. 2012) and exhibits nearly uniform value across the whole source (van Weeren et al. 2015).

However, the radio analyses of 1RXS J0603.3 have mainly been focused on the "Toothbrush", leading to a deep view on this source. The relic has been observed with the *GMRT* and *WSRT* (van Weeren et al. 2012) and, more recently, with *LOFAR* (van Weeren et al. 2015). The first analysis in van Weeren et al. (2012) provided a detailed spectral study of the northern relic. The (overall) spectral index between 74 and 4.9 GHz is $\alpha = 1.10 \pm 0.02$ averaged over the whole source. However, spectral index distribution map of the source indicates a steepening of α and an increasing spectral curvature in the post-shock region. At the edge of the relic the measured injection index is $\alpha_{inj} \sim 0.8$. Few selected regions manifest spectral index as flat as $\alpha_{inj} \sim 0.65$. These measurements are not consistent with the Mach number derived from X-ray observations of the putative shock, indicating $\mathcal{M}_{\rm radio} = 2.8^{+0.5}_{-0.3}$ (van Weeren et al. 2015) under the assumption of DSA (Eq. 2.1). Nevertheless, X-ray observations have large uncertainties and small variations in the injection spectral index lead to significant Mach number deviations.

The "Toothbrush" front is highly polarized, with a polarization percentage up to $\sim 60\%$ at 4.9 GHz over its entire length (van Weeren et al. 2012), although with different polarization levels (the narrower part is more polarized). The electric field vectors are mainly perpendicular to the relic orientation, except in the western region.

Relic radial brightness profiles

The availability of several observations at different radio wavelengths allowed us to cover a wide range of frequencies in our analysis. We used the maps at 147 MHz, 241 MHz, 325 MHz, 610 MHz, 1.2 GHz, 1.4 GHz, 1.7 GHz and 2.3 GHz, published and convolved at the same resolution by van Weeren et al. (2012), whose main properties are summarized in Tab. 5.6.

Table 5.6: Properties of the used radio maps.

Frequency (MHz)	rms (μJy beam^{-1})	Original HPBW ($'' \times ''$)	Instrument
147	950	26.2×22.0	*GMRT*
241	350	16.0×12.0	*GMRT*
325	80	12.0×8.7	*GMRT*
610	40	5.1×4.1	*GMRT*
1221	50	29.0×19.0	*WSRT*
1382	40	27.1×16.4	*WSRT*
1714	30	23.6×15.6	*WSRT*
2272	40	16.1×9.8	*WSRT*

The unusual linear morphology of the "Toothbrush" forced us to separate at least two regions where the radial brightness profiles can be extracted. The northern boundary of the source is sharp, while the emission fades more slowly toward the cluster center. As a first approximation, the relic can be roughly divided into western (`W`) and eastern (`E`) regions (Fig. 5.11). The former is broader and luminous while the latter is straight and narrower.

In determining the extracting region for the `W` part of the relic one must take into account the contribution of the radio halo emission. In fact, the halo progressively emerges at lower observing frequencies, where the relic emission becomes confused with that coming from the cluster center. Moreover, high-resolution observations of the `W` part of the relic display a complex filamentary morphology, where some "streams" of emission extend from the northern to the southern part of the source.

The `E` part of the relic is more linear and regular. The radio emission brightens and fades twice along this narrow extension but also its width slightly changes. For this reason, we choose an extracting region at its center, avoiding (i) the considerably narrow part that connects the `E` to `W` part of the relic and (ii) the tilted edge at the `E` boundary of the relic.

The brightness profiles of the relic obtained for the two regions at the various frequencies are presented in Fig. 5.12 and in Tab. 5.7.

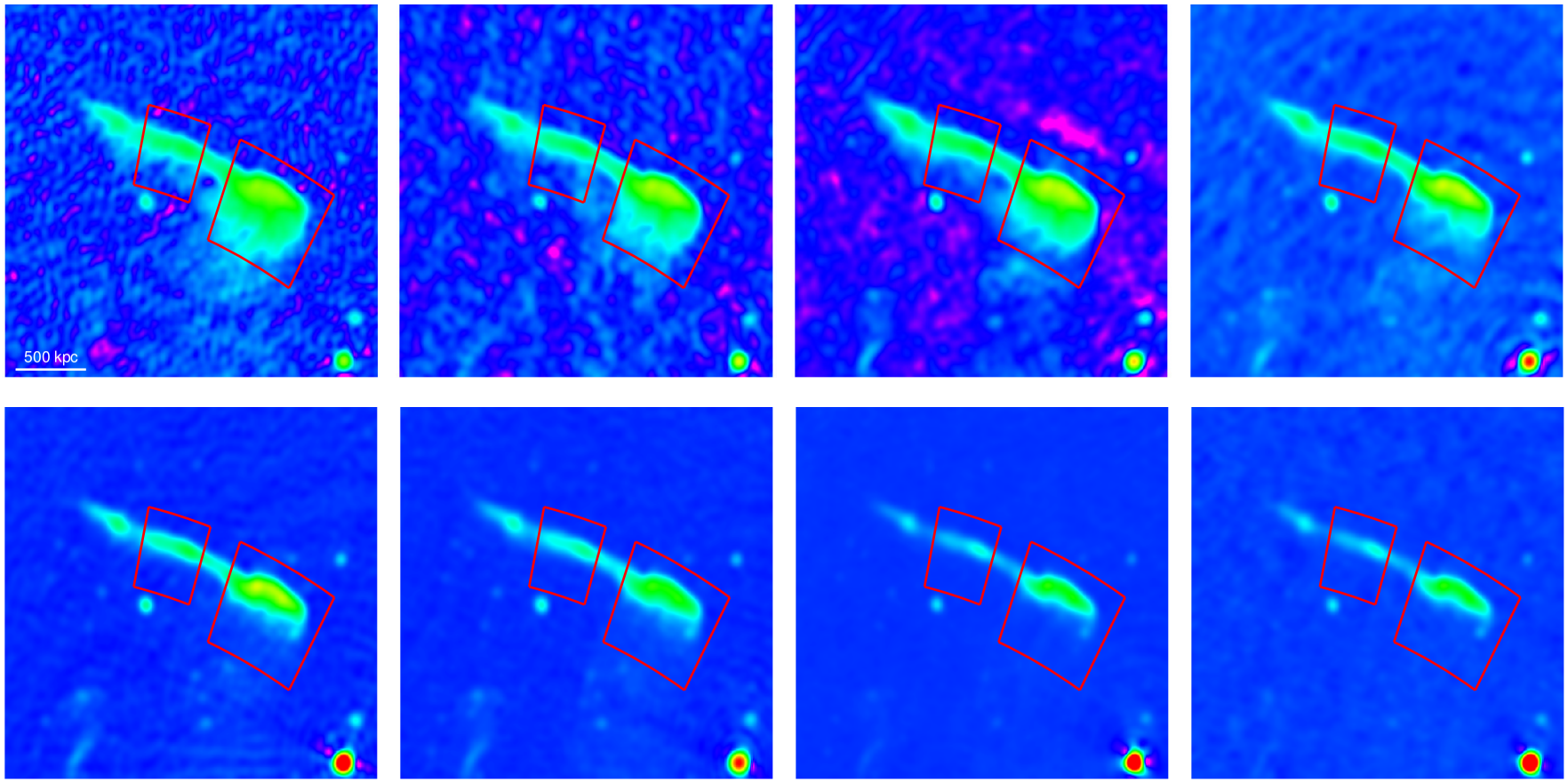

Figure 5.11: From left to right and from top to bottom, 147 MHz, 241 MHz, 325 MHz, 610 MHz (*GMRT*) and 1.2 GHz, 1.4 GHz, 1.7 GHz and 2.3 GHz (*WSRT*) common resolution images of the "Toothbrush" relic. The radial profiles of Fig. 5.12 have been extracted from the two different regions avoiding discrete sources.

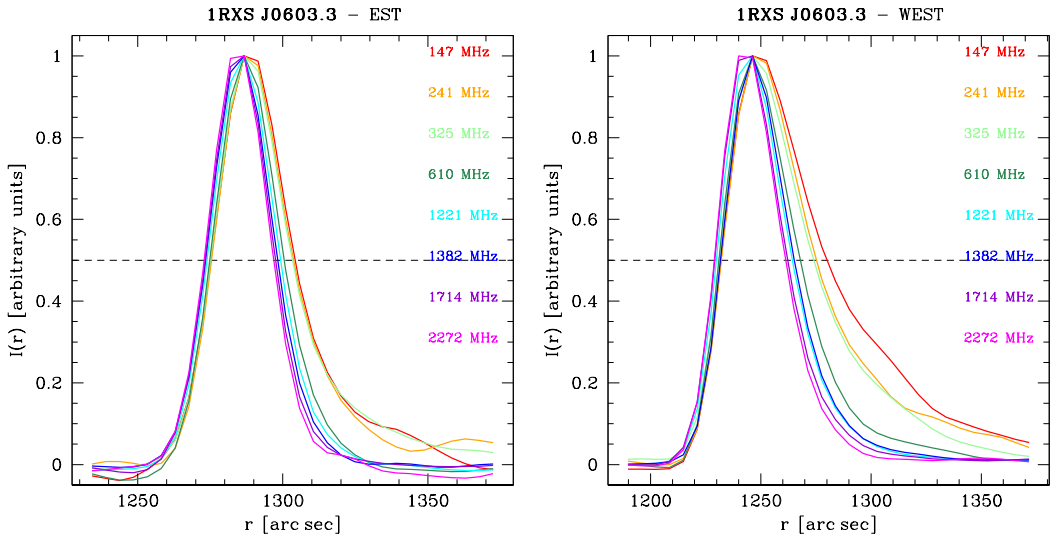

Figure 5.12: Normalized radial brightness profiles of the relic measured at different frequencies (see panels) in the `E` and `W` regions. The horizontal *dashed line* at $I(r) = 0.5$ helps in the comparison between the FWHMs at various frequencies, whose are computed in Tab. 5.7.

Table 5.7: Deconvolved FWHMs of the "Toothbrush" relic for the `E` and the `W` regions at different frequencies. Uncertainties on the FWHMs are generally assumed as a fraction of the beam size, which we conservatively assumed 15%.

Frequency	FWHM	
	`E`	`W`
(MHz)	(kpc)	(kpc)
147	79.3	160.0
241	76.6	139.3
325	74.6	135.4
610	62.3	114.4
1221	61.3	105.0
1382	58.9	100.1
1714	54.8	97.2
2272	52.7	95.0

5.4 Magnetic field estimates

In order to constrain the magnetic field and the geometry of the sources, X-ray and radio observations of the relic region are both required (Chapter 4).

The X-ray properties of the shock allow to determine V_d, which represents the downstream velocity of accelerated particles. Such a measurement requires the determination of the Mach number of the shock and an estimate of the temperature upstream of the shock (see Eq. 4.8). These are two crucial parameters in our model that unfortunately are affected by substantial uncertainties in their determination.

Mach number measurements can be obtained through different techniques such as the search of discontinuities in the profiles of temperature (Eq. 4.5), density (Eq. 4.6) or surface brightness (Eq. 4.7) taken across the region where the shock is supposed to exist. However, it may happen that the jump is detected in the density profile and not in the temperature profile (or vice-versa). This depends on projection effects, on the photon statistics and on the angular resolution of the X-ray observations.

The temperature upstream of the shock is constrained by spectral analysis of the unperturbed region. Also in this case, however, measurements are limited by photon statistics and low signal-to-noise level, implying large errors. In such cases it is possible to use the Rankine-Hugoniot jump condition for temperature (Eq. 4.4) to infer T_u starting from the better constrained T_d, once the Mach number of the shock is determined.

In Tab. 5.8 we report the main properties of the shocks spatially coincident with the relics in our sample.

Table 5.8: Shock region properties for the analyzed radio relic sample.

	A 521[a]	CIZA J2442[b]	1RXS J0603[c]
kT_u (keV)	1.5 ± 0.1	$2.11^{+2.15}_{-0.48}$	$8.3^{+3.2}_{-2.4}$
$\mathcal{M}_\rho$	2.42 ± 0.19	–	–
$\mathcal{M}_{kT}$	$3.40^{+3.69}_{-1.92}$	$3.15^{+0.66}_{-1.31}$	–
$\mathcal{M}_{\rm SB}$	–	–	~ 1.5
$\mathcal{M}_{\rm radio}$	2.27 ± 0.02	$4.6^{+1.3}_{-0.9}$	$2.8^{+0.5}_{-0.3}$
$\mathcal{C}$	2.64	3.07	$\sim$1.71
c_s (km s^{-1})	~ 630	~ 750	~ 1210
V_d (km s^{-1})	578 ± 193	768^{+401}_{-192}	~ 1050

[a]Reference work: Bourdin et al. (2013).

[b]Reference work: Akamatsu & Kawahara (2013).

[c]Reference work: van Weeren et al. (2015).

The radial brightness profiles in Fig. 5.4, 5.8, 5.12 and the FWHMs in Tab. 5.3, 5.5, 5.7 clearly show that the relics become progressively broader at progressively lower observing frequencies, independently from the profile extracting region. This can be interpreted as due to the aging/advection of electrons downstream after being accelerated at the shock location.

Once downstream velocity and FWHMs are collected, our approach can be finally applied. Going back to Eq. (4.2), one must solve

$$\mathrm{FWHM}_\nu = L\cos\theta + V_d\tau_\nu \sin\theta$$

for different values of θ. The information on the magnetic field resides in the particle life-time τ_ν. As a first step, we consider the simplest model of aging due to IC and synchrotron emission (Paragraph 4.3.1).

5.4.1 A 521

A value of the magnetic field of the relic in A 521 was derived in Giacintucci et al. (2006) using equipartition energy condition (see Paragraph 3.3). Assuming an electron power-law energy spectrum with a slope $\delta = 2\alpha + 1$ and using the classical equipartition equations (computed in the frequency range $10\,\mathrm{MHz} < \nu < 100\,\mathrm{GHz}$), they achieved an equipartition magnetic field $B_{eq} = 0.4\,\mu\mathrm{G}$. Adopting the "revised" equipartition equations (Eq. 3.6) they derived $B'_{eq} \sim 1.3\,\mu\mathrm{G}$.

We assume two possible values of the major axis of the relic estimated from the radio images, $L_1 \sim 620\,\mathrm{kpc}$ and $L_2 \sim 1020\,\mathrm{kpc}$, and apply our method for the two cases.

In Fig. 5.13 contour regions of the combination of (B, θ) are shown for three different frequencies. We find that there is a fairly large region (B, θ) where constraints derived at different frequencies overlap. The resulting magnetic field in the downstream region is in the range $0.6 - 8.5\,\mu\mathrm{G}$. The different choices of L induce only minor changes on the constrained values for the magnetic field while the geometry of the region is consistent within $\sim 2°$.

Dashed lines in Fig. 5.13 represent the limits provided by (i) the comparison between the thermal and the magnetic field energy densities at the relic location and (ii) by the lack of IC emission from the relic (see Paragraph 4.2.1).

(i) By using Eq. (4.10), temperature and density profiles of the downstream region (Fig. 5.2) lead to estimate the magnetic fields corresponding to 10 and 30% of the local thermal energy density: $B_{0.1} < 4.3\,\mu\mathrm{G}$ and $B_{0.3} < 7.4\,\mu\mathrm{G}$, respectively. These values can be considered as upper limits for the magnetic field. Strong non-linear amplification of magnetic field, implying dynamical important fields downstream, is indeed unlikely because of the weak shocks that are detected in the relic regions.

(ii) We also combine our constraints with those deriving from the lack of IC emission from the relic. We use the X-ray brightness profile extracted across the relic (Bourdin et al. 2013) and derive an upper limit to the IC emission $F_{[0.5-2.5\,\mathrm{keV}]} \sim 4.4 \times 10^{-6}\,\mathrm{ph\,s^{-1}\,cm^{-2}}$ by assuming that if the 50% of the X-ray surface brightness across the source (i.e. at the profile discontinuity) would be contributed by IC, it should be detectable in the soft X-rays. Using Eq. (2.2) and this limit, we derive a corresponding lower limit for the magnetic field in the relic $B_{IC} > 1.2\,\mu\mathrm{G}$. Limits based on IC are particularly relevant as they rule out the lower values of the magnetic field that are instead allowed by our method (shaded region in Fig. 5.13).

In Fig. 5.13 we also show the values of the magnetic field in the upstream, unperturbed region of the relic. These values have been obtained from those derived from the analysis based on the aging of electrons downstream and scaled upstream by taking into account the compression of the field at the shock (Eq. 4.9). The upstream magnetic field then results to be in the range $0.2 - 3.2\,\mu\mathrm{G}$. Also in this case constraints are combined with limits inferred from Eq. (4.10), resulting in $B_{0.1} < 1.5\,\mu\mathrm{G}$ and $B_{0.3} < 2.5\,\mu\mathrm{G}$.

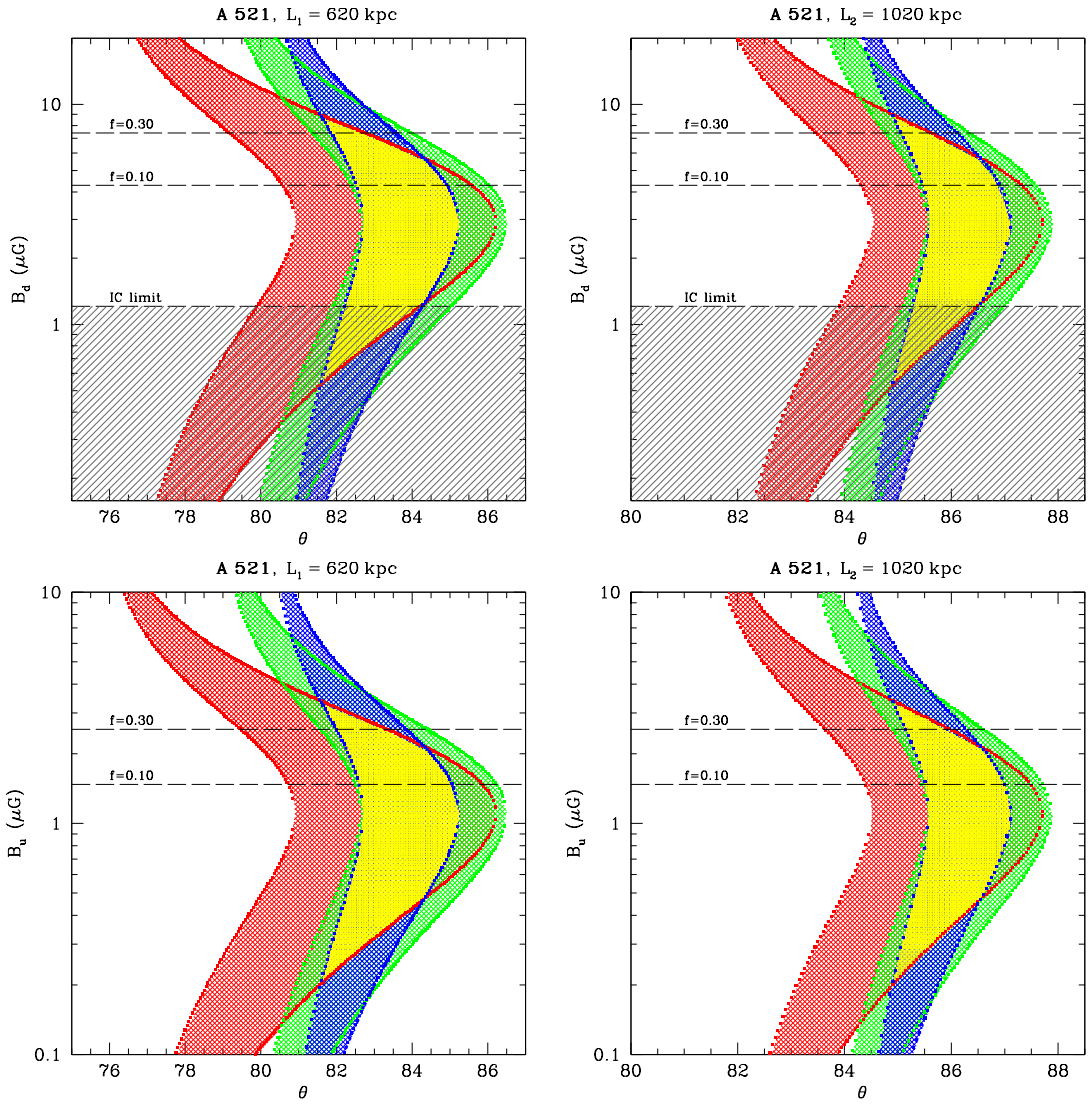

Figure 5.13: Magnetic field and angle contour regions (68%) of the relic in A 521 (color scheme: same of Fig. 5.4, the *yellow region* displays the intersection of the three frequencies) for two choices of L (see panels). Magnetic fields are reported for the downstream (*top panels*) and for the upstream (*bottom panels*) regions. The *dashed lines* mark magnetic fields with energy density 10 and 30% of the (local) thermal one. The *shaded region* marks the forbidden magnetic field values as obtained from the lack of IC emission from the relic.

5.4.2 CIZA J2442

The "Sausage" magnetic field was already investigated in a previous work by van Weeren et al. (2010) by adopting the method based on the thickness of the relic/aging of electrons downstream. The details of that work have already been presented in Paragraph 3.5. We only recall that they estimated a magnetic field strength of either $< 1.2\,\mu$G or $> 5\,\mu$G.

Although similar to our method, the approach of van Weeren et al. (2010) was carried out by assuming a value of the Mach number of the shock that is significantly overestimated, thus leading to a larger value of the downstream velocity. In fact, at the time of their study only the Mach number derived by radio analysis (Eq. 2.1) was available, which has been recently proved to be inconsistent with the results coming from X-ray studies (Akamatsu & Kawahara 2013; Ogrean et al. 2014). Since the value of the downstream velocity is a crucial parameter in this kind of approach (see Appendix A), we re-perform the analysis for this source. Furthermore, van Weeren et al. (2010) used measurements of the relic thickness at a single frequency, being so very sensitive to uncertainties due to projection effects and geometry of the shock/relic surface.

The "Sausage" was divided in two parts during the analysis. The corresponding linear sizes for the relic major axis in the `E` and `W` regions are $L_E \sim 685\,$kpc and $L_W \sim 850\,$kpc, respectively.

In Fig. 5.14 contour regions of the combination of (B, θ) are shown for five different frequencies. The `E` and the `W` parts of the "Sausage" only differ of $\sim 1^\circ$ in inclination angle and an almost edge-on view of the relic is confirmed by our model. The magnetic fields span nearly the same range of strength $0.1 - 14.4\,\mu$G.

With the same arguments made for the relic in A 521, in Fig. 5.14 we report limits coming from (i) considerations about the energy budget of the ICM and (ii) from the IC emission from the relic. In this respect, we use the *Suzaku* analysis by Akamatsu & Kawahara (2013) which provides temperature, pressure and surfaces brightness profiles taken across the shock.

(i) The upper limits to the magnetic field strength (Eq. 4.10) are $B_{0.1} < 4.8\,\mu$G and $B_{0.3} < 8.4\,\mu$G, corresponding to 10 and 30% of the local thermal energy density.

(ii) X-ray surface brightness profile of the relic region leads us to estimate an upper limit to IC emission $F_{[0.5-10\,\mathrm{keV}]} \sim 2.2 \times 10^{-5}\,\mathrm{ph\,s^{-1}\,cm^{-2}}$. Using this result, Eq. (2.2) provides a magnetic field lower limit $B_{IC} > 1.5\,\mu$G. Such an estimate rules out the lower value obtained by van Weeren et al. (2010) and a fraction of our constraints (shaded region in Fig. 5.14).

Bottom panels of Fig. 5.14 show the magnetic field strength in the upstream region of the relic, obtained by applying Eq. (4.9). In this case, the upper limits inferred from Eq. (4.10) result in $B_{0.1} < 1.2\,\mu$G and $B_{0.3} < 2.1\,\mu$G.

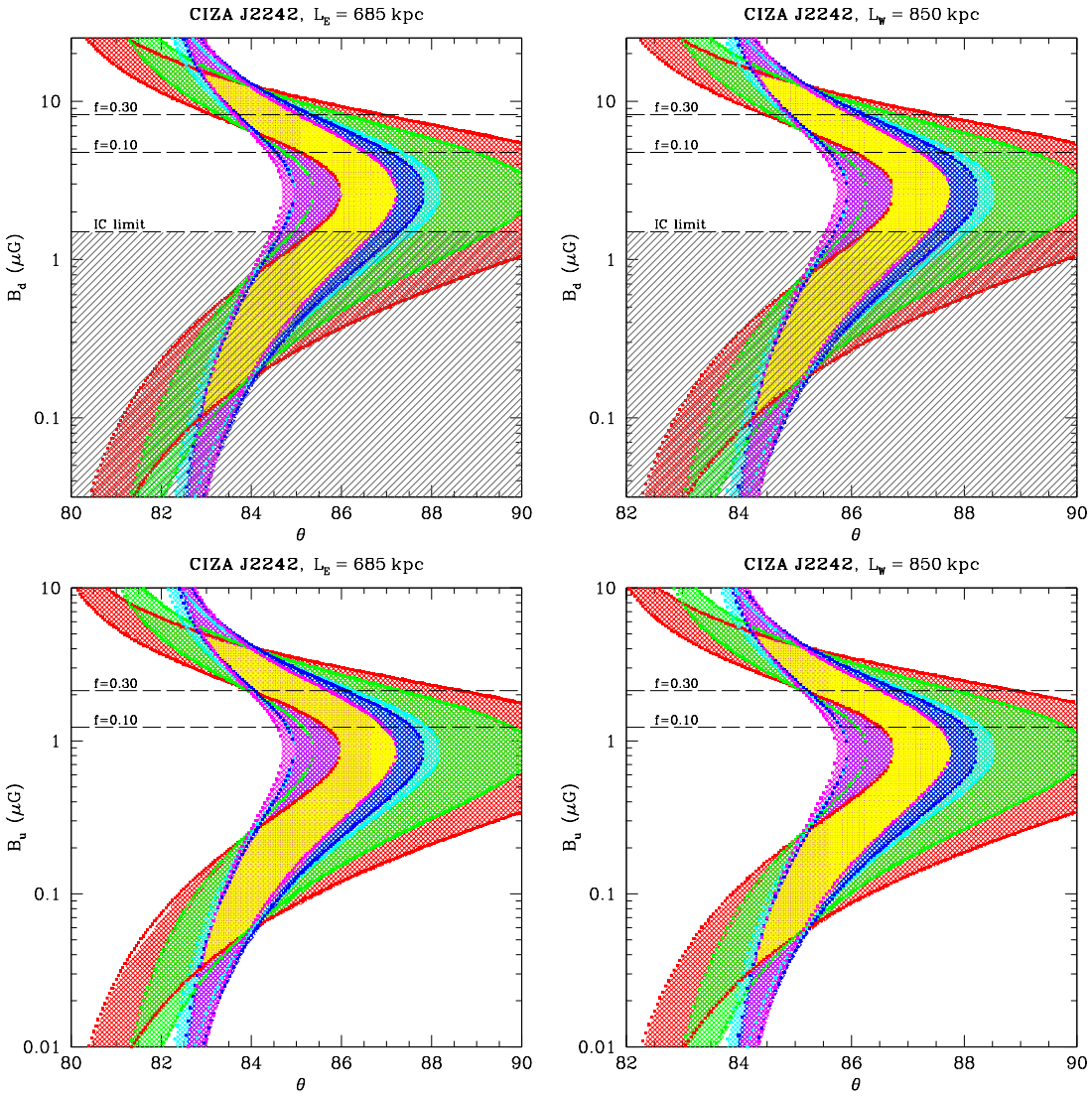

Figure 5.14: Magnetic field and angle contour regions (68%) of the relic in CIZA J2242 (color scheme: same of Fig. 5.8, the *yellow region* displays the intersection of the five frequencies) for `E` and `W` regions (see panels). Magnetic fields are reported for the downstream (*top panels*) and for the upstream (*bottom panels*) regions. The *dashed lines* mark magnetic fields with energy density 10 and 30% of the (local) thermal one. The *shaded region* marks the forbidden magnetic field values as obtained from the lack of IC emission from the relic.

5.4.3 1RXS J0603

Van Weeren et al. (2012) estimated the magnetic field at the front of the "Toothbrush" relic by assuming minimum energy condition in the source. They used the "revised" equipartition formula (Eq. 3.6) and obtained $B'_{eq} = 9.2\,\mu$G or $B'_{eq} = 7.4\,\mu$G assuming a minimum energy cutoff for the electrons $\gamma_{min} = 100$ and $\gamma_{min} = 5000$, respectively. These values indicate a relatively high magnetic field strength.

We attempt to apply our method to the case of the "Toothbrush". In the analysis we select two regions, E and W, assuming linear sizes for the relic major axis (estimated from the radio maps) of 420 and 600 kpc, respectively. However, as described in Paragraph 5.3.1, the properties of the shock connected with this relic are quite uncertain and this is a severe limitation (see Appendix A). As a consequence, we do not derive constraints in the (B, θ) plane, rather we attempt to obtain information on the magnetic field in the relic studying the scalings of its thickness with observed radio frequency.

In Fig. 5.15 we display[1] both for E and W regions the net particle life-time (i.e. subtracted from the projection contribution) as a function of the frequency for different angles θ. This kind of plots allow us to exclude some relic inclination angles. The red line represents the line for which particle life-time is maximized, i.e. when $B = B_{CMB}/\sqrt{3}$ in Eq. (3.8), and thus life-times above this line are forbidden. This allows us to exclude situations where the inclination angle is too large. On the other hand, if we suppose that the relic is not observed edge-on, another condition is $L\cos\theta >$ FWHM, namely the situation where "all" the thickness of the relic is due to projection effects. Multi-frequency observations allow us to optimize this constraint as we can use the minimum observed value of the FWHM, that is the one at the highest frequency, where aging is less important. Limiting cases (i.e. minimum values of θ) are shown in Fig. 5.15 as situations where the value of the particle life-time rapidly decreases at high frequencies, where small values of θ would result in "negative" life-times.

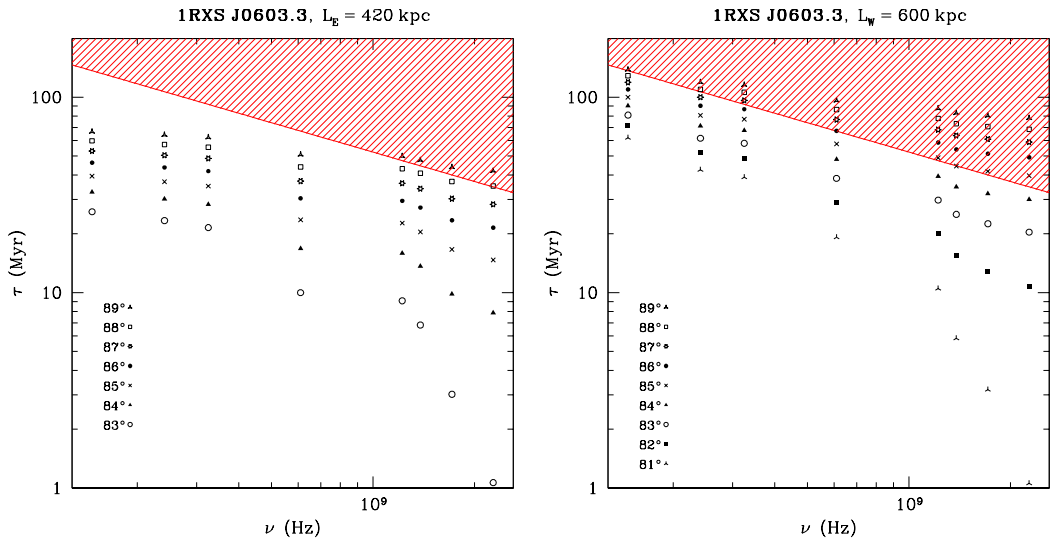

Figure 5.15: Aging of emitting particles for E and W regions. Symbols indicate different θ angles (see panels). The *red line* delimits the forbidden region for particle life-times.

[1] Note that for the E relic region we adopted the same V_d of the W part (Tab. 5.8).

For the W region, the relic geometry is constrained between $\sim 80°$ and $\sim 85°$. We find that the data can be reproduced by two scenarios:

- for $83° \lesssim \theta \lesssim 85°$ radiative aging models (Paragraph 4.3.1) are suitable to describe the collected data. In such cases, the particle life-time is $\propto \nu^{-1/2}$ (Eq. 3.8) and it can be simultaneously described by two values of the magnetic field strength (Fig. 3.5). The best fit is achieved for $\theta = 83°$, leading to either $B = 0.45\,\mu$G or $B = 9.3\,\mu$G (Fig. 5.16);

- for $\theta < 83°$ a steepening with frequency is observed. Although this situation may be affected by projection effects (and indeed we excluded angles $< 80°$ as discussed before), a scaling steeper than $\tau_\nu \propto \nu^{-1/2}$ may suggest the presence of re-acceleration in the downstream region. As discussed in Paragraph 4.3.2, in this case the observing frequency and particle life-time are related by the following expression

$$\nu_c = 1.2 \times 10^6 B \left\{ \frac{\chi}{(B_{CMB}^2 + B^2)[1 - \exp(-\chi\tau)]} \right\}^2 (1+z)^{-1}$$

  where $\chi = 1/t_{acc}$. For each given frequency, we evaluated the magnetic field strength for different t_{acc}. The best model is achieved when the field B is the same for each frequency, namely when the scatter of B around a "mean" value is minimized, as shown in the left panel of Fig. 5.17. We found that a re-acceleration time of $t_{acc} = 50\,$Myr can well reproduce the data at $\theta = 82°$ (Fig. 5.17). In this case, the resulting magnetic field strengths are either $B = 0.15\,\mu$G or $B = 14.5\,\mu$G.

As a final remark, we point out that the lower values obtained for the magnetic field strength are ruled out by the lack of IC emission from the relic. In fact, by using the surface brightness profile taken across the shock (Fig. 5.10), we infer an upper limit to IC emission of $F_{[0.5-2\,\mathrm{keV}]} \sim 6.1 \times 10^{-14}\,\mathrm{erg\,s^{-1}\,cm^{-2}}$, which leads to $B_{IC} > 2.2\,\mu$G.

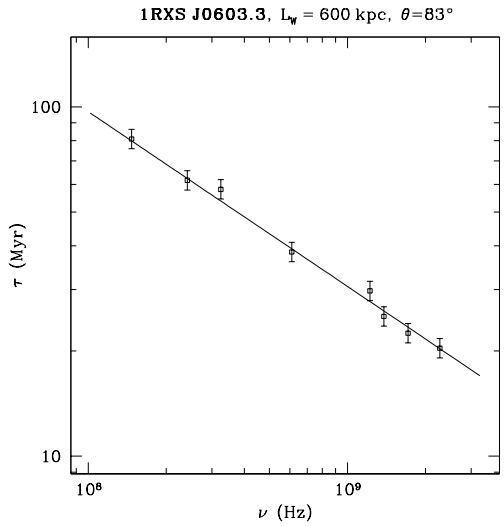

Figure 5.16: Best fit for $\theta = 83°$. The observed data are well reproduced by a pure radiative model with $B = 0.45\,\mu$G either $B = 9.3\,\mu$G (*solid line*).

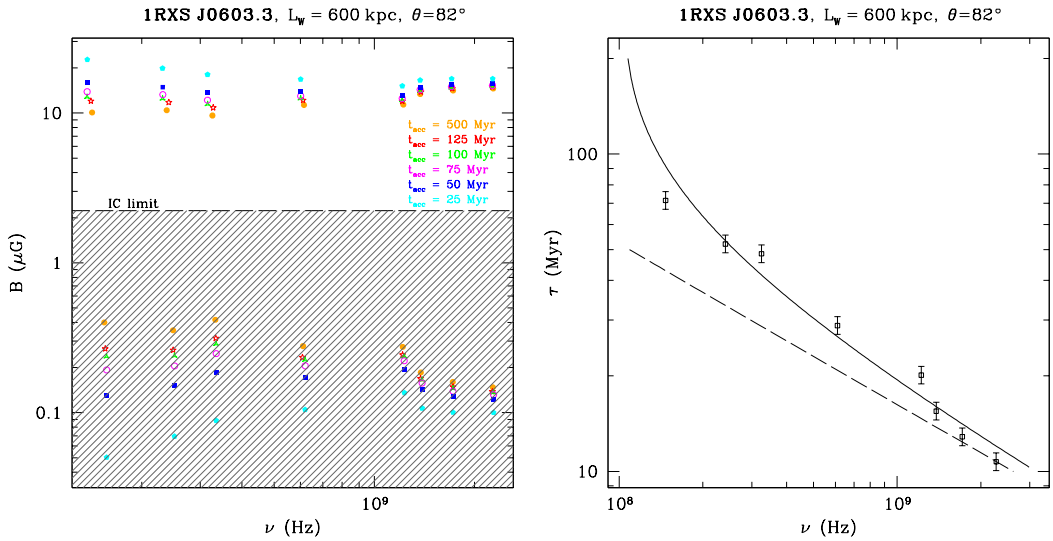

Figure 5.17: Best fits for $\theta = 82°$. *Left panel*: magnetic field as a function of frequency for different t_{acc} (see panel). The best fit value of t_{acc} is achieved when B is the same at various frequencies, i.e. for $t_{acc} = 50$ Myr. *Right panel*: re-acceleration model (*solid line*) versus data points. It leads to $B = 0.45\,\mu$G either $B = 9.3\,\mu$G. For comparison, we report the model of pure radiative aging for which $\tau_\nu \propto \nu^{-1/2}$ (*dashed line*).

For the E part of the relic, the angle is between $\sim 83°$ and $\sim 89°$ if we assume the same V_d of the W region (Tab. 5.8). However, we stress that for this part of the relic no shock is yet detected due to limitations in the X-ray data. Consequently, we restrict to a qualitative analysis based on Fig. 5.15:

- the data points at $\theta = 84°$ provide a fit with slope -0.5, indicative of a pure radiative scenario. For smaller angles, particle life-times drop dramatically at high frequencies, indicating that projection effects are overestimated;

- the more interesting case is when $\theta \gtrsim 84°$, where flatter slopes are progressively achieved. According to Paragraph 4.3.3, flatter scaling can be obtained under the hypothesis of a decaying magnetic field in the downstream region. In this case, the particle life-time is related to the observing frequency with

$$\nu_c = 1.2 \times 10^6 B_0 \exp\left(-\frac{\tau}{t_e}\right)\left\{B_{CMB}^2\tau + \frac{B_0^2 t_e}{2}\left[1-\exp\left(-\frac{2\tau}{t_e}\right)\right]\right\}^{-2}(1+z)^{-1}\,.$$

  where t_e is the time-scale of the decay. This scenario is particularly intriguing since the substantial difference between the E and W regions as well as their change with observing frequencies (Fig. 5.11).

In conclusion, the W region of the relic considerably broadens at low frequencies and mixes with the halo emission, suggesting that particles are sustained by additional processes, possibly re-acceleration, in the downstream region. On the other hand, the broadening of the E region of the relic at low frequencies is very small, suggesting that particle aging in the downstream region is very fast. This can be explained by a magnetic

field declining downstream because at later stages (namely longer times and distances from the edge of the relic, thus lower frequencies) electrons would emit in a weaker magnetic field, where life-time is shorter (for electrons emitting at a fixed frequency) as the main cooling process becomes IC (Paragraph 4.3.3). We will give final remarks on the "Toothbrush" case in Paragraph 6.4.

Chapter 6

Discussion

RADIO RELICS are useful tools to prove magnetic field strengths in cluster peripheries, where other methods can not be of any help. We used a geometric model combined with physical arguments based on the transport of the downstream emitting particles to derive constraints on the field intensity and evolution with time for three relics. Our idealization of the relic/shock region is simple and requires few parameters. We combined the constraints with limits obtained from the lack of IC emission from the radio relic and from considerations based on the energy content of the magnetic field in relic regions. In the case of the "Toothbrush", the possible parameter determination was spoiled by a controversial Mach number investigation. In this case, we adopted a different approach which takes advantage of the radio observations available over a wide range of frequencies.

Our magnetic field estimates confirm that μG magnetic fields exist at the cluster boundaries. This has interesting consequences regarding the spatial distribution of the magnetic field and the role of non-thermal components in GCs. In the following, we will compare our results with those already present in the literature. At the end of this Chapter we highlight the limits of our method and its uncertainties. Final considerations on the "Toothbrush" case are then given.

6.1 Overall results

An overview of the magnetic field and angle constraints achieved in Chapter 5 is reported in Tab. 6.1. For the clusters A 521 and CIZA J2442, our magnetic field estimates span almost an order of magnitude in strength. In the case of 1RXS J0603, we derive two significantly separated field strength values.

Lower limits to the field strength, B_{IC}, due to the lack of IC emission from relics allow to exclude a significant fraction of the gathered values. Further (upper) limits to the field, $B_{0.1}$ and $B_{0.3}$, are derived assuming that the field energy density is 10 and 30% of the local thermal energy density, respectively. Both these limits are reported in Tab. 6.1.

In determining the sample of radio relics suitable for our analysis we selected sources with a possible edge-on view along the line-of-sight. This was confirmed by our analysis ($\theta > 80°$). Our constraints indicate that magnetic fields above the μG level exist in cluster outskirts.

Table 6.1: Overall results of (B, θ) for the relic sample. For the cluster 1RXS J0603 (W region) we report the constraints obtained with the pure radiative aging model and with a scenario consistent with particle re-acceleration on a time-scale $t_{acc} = 50$ Myr. In Table, magnetic fields are expressed in μG.

	A 521	CIZA J2442	1RXS J0603	
			(radiative)	(re-acceleration)
θ	$81° - 85°$	$83° - 87°$	$83°$	$82°$
B_d	$0.6 - 8.5$	$0.1 - 14.4$	0.45, 9.3	0.15, 14.5
$B_{d,0.1}$	< 4.3	< 4.8	$-$	
$B_{d,0.3}$	< 7.4	< 8.2	$-$	
B_{IC}	> 1.5	> 1.2	> 2.2	
B_u	$0.2 - 3.2$	$0.03 - 4.9$	$\sim 0.26, \sim 5.4$	$\sim 0.09, \sim 8.5$
$B_{u,0.1}$	< 1.5	< 1.2	$-$	
$B_{u,0.3}$	< 2.5	< 2.1	$-$	

6.2 Magnetic field distribution

Magnetic fields are not dynamically relevant in GCs (e.g. Dolag et al. 2005a). In fact, the strength derived by comparing the thermal energy density

$$\varepsilon_{th}(r) = 3 n_e(r) k_B T(r) \tag{6.1}$$

to the magnetic field energy density

$$\varepsilon_B(r) = \frac{B(r)^2}{8\pi}$$

is typically larger with respect to the observed $\sim \mu$G field level. Thermal gas density in GCs is often assumed to follow a β-model (Eq. 1.4), hence a magnetic field constant with radius would lead magnetic field energy density to be comparable, or even higher, to the thermal one. As a consequence, B must decrease with cluster radius.

Jaffe (1980) first suggested that cluster magnetic field distribution would depend on the thermal gas density and on the distribution of massive galaxies and therefore would decline with the cluster radius. Hints to the radial gradient of the cluster magnetic field strength are possibly suggested by the spatial correlation found in some GCs between the X-ray brightness and the radio halo brightness (Govoni et al. 2001).

However, the main observational results regarding magnetic field intensity and topology in GCs are obtained from Faraday rotation studies (Paragraph 3.1). In a milestone work, Clarke et al. (2001) showed that polarized sources observed behind or within GCs exhibit higher RM (Fig. 3.2), demonstrating the magnetization of the ICM. The investigation of RM for sources at different impact parameters from cluster cores suggests also the radial dependency of cluster magnetic fields (A 119, Murgia et al. 2004; A 2255, Govoni et al. 2006; A 2382, Guidetti et al. 2008; Coma cluster, Bonafede et al. 2010, 2013). Generally, RM studies support that magnetic fields are not ordered on cluster-size but fluctuate over a wide range of spatial scales.

6.2.1 The role of numerical simulations

Whether the origin of cluster magnetic fields is *cosmological* or *galactic* (Paragraph 3.6) it does not seem important to explain current field strengths and structures. Seed fields increase their strengths during structure formation process. In fact, a magnetized spherical cloud undergoing gravitational collapse is subjected to plasma compression, thus magnetic field amplification. Since the cloud density is $\rho \propto r^{-3}$ and the magnetic flux $\Phi_B = Br^2$ must be conserved, it is $B \propto \rho^{2/3}$. This leads to increasing magnetic field intensities during the collapse and gives a natural dependency of B with r. However, gravitational collapse is not sufficient itself to explain the observed $\sim \mu$G field level in GCs.

Numerical simulations play an important role to understand the magnetic field amplification in GCs (see Dolag et al. 2008 for a review). Cosmological MHD simulations show that seed fields are further amplified by shear flows, shocks and turbulence driven by merger/accretion events during cluster formation (Fig. 3.6). Turbulent diffusion is also expected to spread magnetic fields in cluster outskirts (e.g. Xu et al. 2009). As a result, the final magnetic field properties (namely B in massive systems) are not dependent of the seed. It is worth mentioning that these results are obtained by using a variety of different codes, which are based on different numerical schemes.

Merger events introduce large amounts of MHD instabilities (e.g. Roettiger et al. 1996, 1997, 1999b). These are responsible for swirling motions and magnetic field amplification. The preexisting field initially becomes quite filamentary, as a result of stretching and compression caused by shocks and bulk flows during matter in-fall; at this stage only a minimal amplification occurs. When the bulk flow is replaced by turbulent motions (e.g. eddies), the field amplification is more rapid, particularly in localized regions (Fig. 3.7). The integrated merging history of a cluster is then fundamental to explain its magnetic field strength and structure. Since high-mass clusters undergo the most energetic mergers, they are expected to exhibit higher magnetic field strengths, as suggested by the $B-T$ correlation gathered by numerical simulations (Dolag et al. 2005a). Dolag et al. (2001) predicted also the existence of a correlation between Faraday rotation and cluster X-ray flux. Since the RM dispersion is obtained from

$$\sigma^2_{RM} \propto \int_0^L (n_e B_{\parallel})^2 \, dl$$

and the X-ray flux is

$$F_X \propto \int_0^L n_e^2 \sqrt{T} \, dl$$

the two observables relate the two line-of-sight integrals with each other, therefore by comparing these two quantities cluster magnetic field versus thermal density are actually compared. The magnetic field profile can be represented by

$$\langle B \rangle (r) = \langle B_0 \rangle \left(\frac{n_e(r)}{n_0} \right)^{\eta} \tag{6.2}$$

where $\langle B_0 \rangle$ is the mean magnetic field strength at the cluster center and a β-model (Eq. 1.4) is assumed for $n_e(r)$. It is worth noting the following trends for different η:

- if $\eta = 1$ the magnetic field scales with n_e;
- if $\eta = 1/2$ the magnetic field energy density ε_B scales with ε_{th};
- if $\eta = 2/3$ the magnetic field is frozen in the plasma.

In general, numerical simulations predict a magnetic field profile similar to the density profile. This predicted scaling is consistent with that measured with RM, as shown in Fig. 6.1.

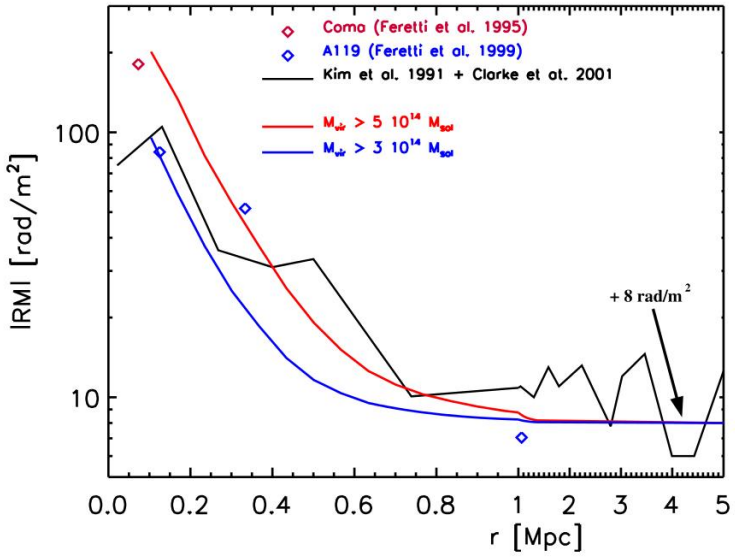

Figure 6.1: Comparison of RM in simulations with observations of Abell clusters, as a function of the distance from the cluster center (Dolag et al. 2008). The *smooth lines* represent the median values of |RM| produced by simulated clusters with masses above $5 \times 10^{14}\,M_\odot$ (*upper line*) and $3 \times 10^{14}\,M_\odot$ (*lower line*). The *broken line* represents the median of combined data taken from the independent samples presented in Kim et al. (1991) and Clarke et al. (2001). *Diamonds* refer to the sources observed in A 119 (Feretti et al. 1999) and to the source 5C4.81 observed in the Coma cluster (Feretti et al. 1995).

6.2.2 Constraints on thermal and magnetic field energy density ratio

The Coma cluster is a suitable target to investigate the magnetic field profile because it is a massive and nearby GC. In fact, first Faraday rotation studies were performed in such a cluster, leading a field strength of $\sim \mu$G (Kim et al. 1990, 1991). More recently, Bonafede et al. (2010) performed a detailed analysis of RM of polarized sources at different impact parameters from the cluster core and compared them with simulated σ_{RM} values. They constrained magnetic field strength and slope (Eq. 6.2) to be in the range $(B_0 = 3.9\,\mu\text{G}, \eta = 0.4)$ and $(B_0 = 5.4\,\mu\text{G}, \eta = 0.7)$ within 1σ (Fig. 6.2). The best fit values are achieved for $B_0 = 4.7\,\mu$G and $\eta = 0.5$, hence a scaling between ε_B and ε_{th} is inferred. In a more recent work, Bonafede et al. (2013) extended RM study to probe the magnetic field properties in the outskirts of the cluster, where the radio relic is located. In this case, the resulting magnetic field strength is higher with respect to that expected from the extrapolation of the scaling observed by Bonafede et al. (2010) (Fig. 6.2).

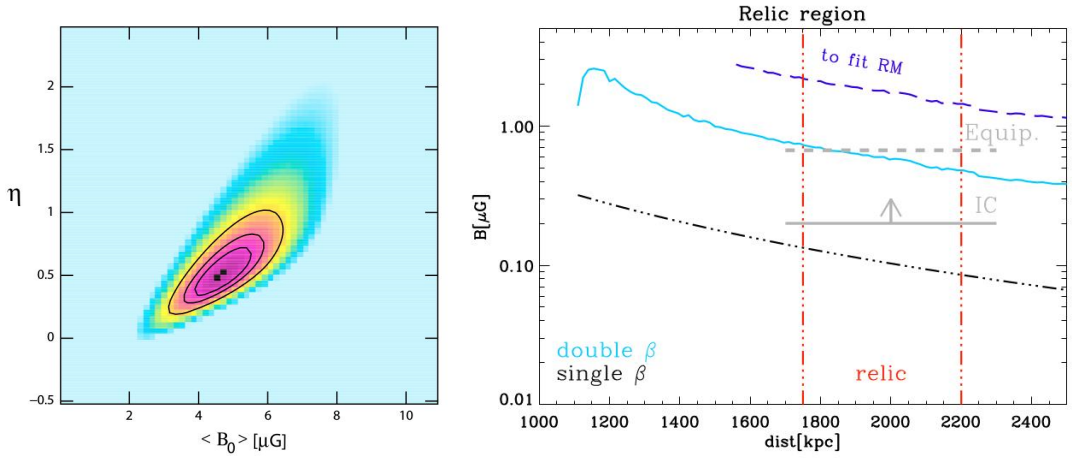

Figure 6.2: *Left panel*: allowed (B_0, η) region (contours are reported at 1, 2, 3σ) gathered by the comparison between simulated and observed σ_{RM} in the Coma cluster (Bonafede et al. 2010). *Right panel*: magnetic field profiles in Coma cluster outskirts (Bonafede et al. 2013). The *black dashed-double-dotted line* displays the profile obtained by Bonafede et al. (2010), the *cyan line* displays the profile assuming a double-β model for the gas density. The *blue dashed line* displays the magnetic field needed to fit the RM data in the relic region and beyond. Overplotted are the lower limit from IC (Feretti & Neumann 2006) and the estimation from equipartition (Thierbach et al. 2003).

In order to extend the constraints on the magnetic field distribution in GC outskirts, we use our magnetic field estimates in radio relic. Our measurements lead to delineate the $\varepsilon_{th}/\varepsilon_B$ ratio at cluster boundaries with interesting implications for the magnetic field profile. We compare the results obtained in Chapter 5 for A 521 and CIZA J2242 to the detailed analyses of Bonafede et al. (2010, 2013) for the Coma cluster.

To obtain $\varepsilon_{th}(r)$, thermal gas density and temperature profiles are both required (see Eq. 6.1). The following information has been collected:

- in the **Coma cluster**, the ICM can be considered almost isothermal, with $kT = 8.25 \pm 0.10$keV (Arnaud et al. 2001). The density profile $n_e(r)$ can be described by a β-model with parameters determined by Briel et al. (1992). The relic region has been recently observed with *Suzaku* (Akamatsu et al. 2013; Simionescu et al. 2013) providing both temperature and density profiles;
- **A 521** density and temperature profiles in the relic region have been both derived in Bourdin et al. (2013);
- **CIZA J2242** relic X-rays analysis can be found in Akamatsu & Kawahara (2013).

Our results have been obtained for different GCs. In order to achieve a fair comparison we re-scale distances from the cluster center in term of

$$r_{500} = \sqrt[3]{\frac{3M_{500}}{4\pi\Delta_{500}}}$$

where M_{500} is the mass within which the average density Δ_{500} is 500 times the critical density ρ_{crit}. The constraints collected for the three clusters are reported in Tab. 6.2.

Table 6.2: Thermal and magnetic field energy density values at the relic distance d_{RR} for three different clusters. Two energy density values for ε_B indicate the (IC) lower and the upper limits inferred from observations. In the case of the Coma cluster they indicate the values obtained by Bonafede et al. (2013).

	Coma	A 521	CIZA J2442
z	0.023	0.247	0.192
M_{500} ($10^{14}\,M_\odot$)	5.3	6.9	8.0
r_{500} (Mpc)	1.2	1.2	1.3
d_{RR} (Mpc)	~ 2	~ 0.9	~ 1.2
ε_{th} (erg cm^{-3})	3.3×10^{-12}	4.0×10^{-12}	7.5×10^{-12}
ε_B (erg cm^{-3})	4.3×10^{-14}	5.8×10^{-14}	8.0×10^{-14}
	2.3×10^{-13}	2.2×10^{-12}	7.1×10^{-12}

The comparison between the Coma cluster results and our constraints on A 521 and CIZA J2442 are presented in Fig. 6.3. Our values obtained for $\varepsilon_{th}/\varepsilon_B$ appear biased low with respect to those in Bonafede et al. (2010), while they appear better in line with those in Bonafede et al. (2013). On one hand this might be natural because both our results and Bonafede et al. (2013) refer to regions where radio relics are present, whereas Bonafede et al. (2010) focused on the central Mpc region of the cluster. However, it still is uncertain how much this can affect the $\varepsilon_{th}/\varepsilon_B$ ratio because shocks increase both ε_{th} and ε_B. Considering a situation where the magnetic field is only compressed (in a plasma with $\Gamma = 5/3$), it is

$$\left(\frac{\varepsilon_{th}}{\varepsilon_B}\right)_d \sim \left(\frac{\varepsilon_{th}}{\varepsilon_B}\right)_u \frac{(\mathcal{M}^2+3)^2(5\mathcal{M}^2-1)}{64\mathcal{M}^4}$$

that is not enough to explain a significant decrease of $\varepsilon_{th}/\varepsilon_B$ for low Mach numbers (for $\mathcal{M} = 2$ the decrease is $\sim 10\%$). Obviously, non-linear amplification of B downstream is expected at shocks (e.g. Riquelme & Spitkovsky 2010), however shock associated with relics are weak and it is not clear how much they can non-linearly amply the magnetic field.

Another possibility (see Bonafede et al. 2013) is that the region of the Coma relic (and we may guess the same for our relics) is dynamically very active, hence B can be biased up with respect to the average value in the cluster volume.

Alternatively, our results in Fig. 6.3 may suggest a picture where the magnetic field spatial distribution is broader than that of the thermal plasma, i.e. $\eta < 0.5$ in Eq. (6.2). Indications for a broader distribution of magnetic fields come from the radial profiles of radio halos, that in several cases are much broader than the X-ray profiles (e.g. Govoni et al. 2001; Planck Collaboration 2013).

As a final remark, it is worth noting that the constraints on B in relics are strongly contributed from the limits derived by the lack of detectable IC emission from relic sources. Although this leads only to lower limits on B, it discriminates a large variety of model profiles, leading to upper limits on the $\varepsilon_{th}/\varepsilon_B$ ratio. In this respect, future more sensitive X-ray observations of relic regions (especially aimed to search surface brightness discontinuities) will provide a real breakthrough in this field.

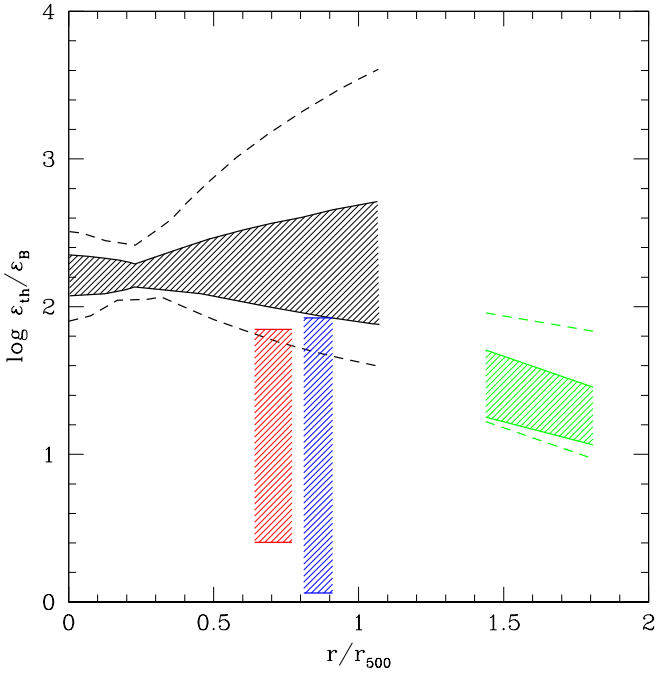

Figure 6.3: The ratio between thermal and magnetic field energy densities as a function of r_{500} for three GCs. In *black*, we report Bonafede et al. (2010) results at 1σ (*shaded region*) and 3σ (*dashed lines*) for the Coma cluster. Boxes indicate the constraints for the relics in Coma (*green*) (Bonafede et al. 2013), in A 521 (*red*) and in CIZA J2442 (*blue*).

6.3 Limitations

We adopted a model in which particles accelerated at the shock surface are then advected downstream the shock. The relic thickness as measured at different radio frequencies is given by the combination of the downstream velocity and the particle lifetime. In the latter resides the magnetic field information we are interested in. Projection effects affect the observed relic transverse size, hence the geometric model of Fig. 4.1 has been developed. This clearly is a shock idealization and it assumes two simplifications: (i) a sheet-like front and (ii) a constant Mach number on its "surface".

(i) The first point is questioned by the large variety of relic morphologies observed in the literature. For this reason, we extracted radial brightness profiles in the most regular regions of the source to prevent effects due to the proper relic morphology, as patchy or filamentary structures. This, together with the requirement of a nearly edge-on view of the source, significantly reduces the number of relics suitable for this analysis.

(ii) Mach number variations on shock fronts inferred from numerical simulations are claimed (Skillman et al. 2013). Moreover, X-ray shock analyses consider large regions across the relic to maximize the signal-to-noise ratio. As a result, mean values are achieved. Only deep and detailed observations would overtake such a limitation.

In selecting the profile extracting regions, we avoided discrete sources along the line-of-sight and the possible contamination due to radio halos, which commonly reside in the relic surroundings. If not, these would increase the measured FWHMs, leading to wrong relic transverse sizes. However, these effects are not particularly relevant if compared to the uncertainties from the X-ray analysis.

We used the Mach number to infer the downstream velocity (Eq. 4.8), which set one of the two physical parameters leading to the relic observed thickness, hence it is a crucial quantity in our model (see Appendix A). Its estimation is a real issue since the weak shocks expected in the ICM. Although various approaches to infer $\mathcal{M}$ exist (see Paragraph 4.2), the shock characterization may result ambiguous and different techniques may lead to different Mach numbers. In few cases, an inconsistency between the Mach number derived from X-rays and that derived from radio observations has been observed (e.g. Akamatsu & Kawahara 2013). However, recent simulations of cluster shocks indicate that such a discrepancy might be due to projection effects (Hong et al. 2015).

The other parameter that concerns relic transverse size is particle life-time. This can only be evaluated theoretically. As a first approximation particle ages radiatively. However, various processes could play a role downstream the shock in increasing or decreasing particle energy, hence its life-time. We considered models for re-acceleration and decaying magnetic field. Future radio observations, e.g. with *LOFAR*, will help in the discrimination between the models that mostly diverge at low frequency.

6.4 The "Toothbrush" case

The cluster 1RXS J0603 has a complex nature as well as its northern relic. New X-ray and radio observations are both under analysis to unveil the puzzling scenario of this system. We focused on the "Toothbrush", which is one of the most spectacular radio relics ever detected so far. Its peculiarities are due to its unusual morphology, to its large ($\sim 2\,\mathrm{Mpc}$) linear size and to the lack of a clear shock wave detection across the source. Although the detailed radio analyses performed by van Weeren et al. (2012, 2015) suggest a $\mathcal{M}_{\mathrm{radio}} = 2.8^{+0.5}_{-0.3}$, X-ray observations are not yet conclusive to claim a shock detection. As a remark, the putative shock emerges only in the broadest part of the relic (Ogrean et al. 2013b) even if the radio spectral index map and the spectral curvature of the relic are consistent with DSA along the whole relic major axis. In this respect, deeper X-ray investigation are needed to verify the valid hypothesis of an underlying shock.

The uncertainties deriving from the X-ray analysis forced us to adopt another approach to investigate the magnetic field in the "Toothbrush". We used the uniquely large number of available observations covering the frequency range $147\,\mathrm{MHz} - 2.3\,\mathrm{GHz}$ to infer both particle aging and geometry.

For the broadest part of the relic (`W` region), our estimates are consistent either with a pure radiative aging or with a particle re-acceleration model, depending on the projection. The latter scenario is interesting and it was also invoked by van Weeren et al. (2012) with arguments related to the spectral index flattening in the region between the relic and the halo. Re-acceleration (e.g. by turbulence) downstream the shock could also play a role in powering the radio halo, located directly south of the `W` relic region, as suggested by the spatial connection between the two sources.

The `E` part of the "Toothbrush" has a significantly narrow transverse size with respect to the `W` region, indicating that some processes might occur and suppress particle advection. Unfortunately, no Mach number is measured in this relic region due to limitations in the X-ray observations. Thus, we only have the possibility to investigate this part of the relic using scalings between aging and frequency assuming the same

downstream velocity for whole the relic length. We found that a decaying magnetic field is an attractive scenario suggested by the flat slopes between τ and ν achieved in Fig. 5.15. Such a decay can be naturally explained if the relaxation/expansion of the gas downstream or if magnetic reconnection in the downstream region occur. This would be the first detection of a decaying magnetic field in a radio relic. As a final remark, if we assume that the downstream velocity is the same over the whole relic major axis and particle are accelerated by the same shock front, a simultaneous IC and spatially constant synchrotron emission for both the regions can not explain the observed relic morphology, hence re-acceleration in the `W` part or a decaying field in the `E` part would be automatically invoked.

General conclusion

Our method combines both radio and X-ray observations of the source and it is based on a fair and clearly simplified geometric model. Nevertheless, it is able to give reasonable constraints on the magnetic field strength in a sample of radio relics. The limits from the lack of IC emission and from considerations on the magnetic field energy density in the relic region contribute to restrict the allowed field values. As a final result the combination of these approaches provide fairly good constraints on the magnetic field properties.

In the case of the “Toothbrush”, the absence of a clear shock detection does not allow a straight application of the model. This highlights that X-ray observations are fundamental in our approach and they also have a large impact on the magnetic field achieved (Appendix A). For this reason, the “Toothbrush” has been studied evaluating the aging of the emitting particles. Its peculiar morphology leads to investigate smaller regions with respect to those of the other selected relics. In this case, we find that more complex aging scenarios could be present. However, the interpretation of this radio relic still is challenging nowadays. Only future multi-wavelength studies will shed light on this object.

Conclusions

NON-THERMAL PHENOMENA in GCs represent a promising research field to unveil a wide number of physical processes in the ICM. In the radio band, diffuse synchrotron emission proves the existence of relativistic particle and magnetic fields on cluster scale. Radio relics play a fundamental role in testing non-thermal phenomena at the cluster boundaries. They are found in merging systems and their connection with gigantic shocks is now well established by a number of observational facts.

There is broad consensus on the hypothesis that relics are due to DSA. Shock are indeed capable to accelerate high-energy particles and amplify magnetic fields, although the mechanisms that generate relics are still debated and differences with the case of SNR clearly emerge from numerous studies. Radio relics are also important probes of magnetic field properties in cluster outskirts, proving the presence of μG fields at Mpc distances from cluster centers. Indeed this has been the central point of our Thesis. This Thesis work has been focused on radio relics with the purpose to achieve the first solid estimates of the magnetic field strength in cluster outskirts.

We adopted the method presented by Markevitch et al. (2005). This method allows to constrain the magnetic filed in radio relics by combining the measurements of the thickness of relics with the downstream velocity of the shock that is responsible for the acceleration of the emitting electrons. We extended this approach:

- by taking into account projection effects using a geometric model;
- by considering several physical scenarios for the evolution of electrons and magnetic field downstream;
- by combining measurements of the thickness of the relics taken at several different frequencies.

This has been discussed in Chapter 4. In addition to the constraints on the magnetic field obtained from the thickness of radio relics we also derive limits on the magnetic fields from the non-detection of IC X-rays emission from the sources.

We studied three well known radio relics in the clusters A 521, CIZA J2242 and 1RXS J0603. These relics are seen almost edge-on, thus minimizing projection effects. In addition deep X-ray observations have measured the shocks connected with these relics and allow to derive suitable limits on the IC emission from the relics. In the following we briefly highlight the most relevant results.

(i) Under the assumption that the magnetic field is constant in the downstream region, combining the X-ray and the radio measurements at several frequencies, we were able to derive the magnetic field in A 521 and CIZA J2242.8. For these two relics we derived limits on the field strength from the lack of IC emission in the X-rays. These limits proved to be important as they rule out a range of (lower) values of the magnetic field that are still consistent with the analysis of the relic thickness. The final outcome of our analysis is a fairly defined range of magnetic field values and shock inclination angles that is allowed to explain multi-frequency observations of the relics (Paragraphs 5.4.1 and 5.4.2). As a second step we attempted to use our measurements to improve current constraints on the spatial profile of magnetic fields in GCs. We combined our measurements with the constraints derived by Bonafede et al. (2010, 2013) for the Coma cluster using Faraday rotation measurements. In doing that we re-scaled distances in units of r_{500}. This combination suggests that the spatial profile of the magnetic field energy density is broader than that of the thermal gas. Alternatively, radio relics may trace dynamically active regions where the magnetic field is locally amplified with respect to the thermal energy and consequently it appears biased high with respect to the average value in the cluster volume.

(ii) In the case of the relic in 1RXS J0603 the X-ray measurements are unable to firmly constrain the properties of the shock and thus we adopted a more simplified approach based on the scaling between the thickness of the relic and the observing frequencies (Paragraph 5.4.3). Nevertheless, for this relic we obtained very intriguing results. In particular, our analysis suggests the presence of particle re-acceleration downstream in the `W` region of the relic and a magnetic field decaying downstream in the `E` part of this relic. This scenario is particularly attractive as it could naturally explain the peculiar relic morphology with a narrow part (`E`) and a broader part (`W`). We also showed that future observations at lower frequencies, with *LOFAR*, will be able to confirm our conjectures.

In general, the future for the studies of non-thermal emission in GCs is promising thanks to the next generation of radio telescopes. In fact, new instruments such as *LOFAR*, *SKA* and a number of its precursors, will enter into unexplored territories, reaching unprecedented sensitivities to cluster scale emission over a broad frequency range. In particular in connection with the work carried out in this Thesis, *LOFAR*, that will probe the Universe at frequencies well below the 100 MHz, will constrain the transport and aging of electrons with lower energies. These electrons have longer lifetimes and will probe physical conditions downstream at large distances from the shock and at long time-scales, thus allowing to discriminate among different scenarios.

As a final note, we mention that first results of this Thesis have been presented in a poster at the international conference:

"**SnowCluster - The Physics of Galaxy Clusters**" in Snowbird (USA), March 2015
Title: *Constraining magnetic field strengths in radio relics: the case of Abell 521*
Authors: *A. Botteon, G. Brunetti, D. Dallacasa*

Appendix A

Mock radio relics

THE GEOMETRIC MODEL presented in Chapter 4 is based on few parameters to work. However, the estimation of the downstream velocity V_d, which enters in Eq. (4.2), and its error σ_{V_d} represents an issue in our idealization since they are derived from the determination of the Mach number of the shock which is often uncertain. Different observational approaches may indeed lead to different values of the shock Mach number (see Chapter 5).

In order to illustrate how the contour regions of (B, θ) are influenced by the parameters of our model it is useful to simulate a simple set of radio relics. The "standard" fictional radio relic of Fig. 4.2 has been created adopting typical values for a relic source:

- relic major axis length: $L = 1000\,\mathrm{kpc}$
- downstream velocity: $V_d = 1000 \pm 100\,\mathrm{km\,s^{-1}}$
- redshift: $z = 0.2$

it will thus be considered as the reference relic to compare with the others. In the following, we show contour regions for mock radio relics, in particular:

- in Fig. A.1 we show the changes in the (B, θ) plane induced by changing the major axis of the relic, L. We conclude that results are not significantly affected by changes in L. Changes are significant if we restrict the analysis using only one observing frequency, however the combination of constraints from several frequencies essentially allows us to disentangle projection effects from aging. The reason why results do not significantly depend on L is because the projection effects are sub-dominant with respect to aging effects at low frequencies;

- in Fig. A.2 we show that the fractional error on the downstream velocity, $\frac{\sigma_{V_d}}{V_d}$, strongly influence the "allowed" region of (B, θ), hence it is a critic point of the model. We conclude that a condition necessary to carry out during our analysis is a good determination of the value of the downstream velocity (i.e. of $\mathcal{M}$ and T_u). For this reason, in Chapter 5 we do not apply this analysis to the case of the "Toothbrush" relic;

- connected to the previous point, in Fig. A.3 we show that the downstream velocity, V_d, plays an important role in determining B, since the relic FWHM is $\propto V_d$ (at fixed τ_v);

For each comparison we report the "standard" fictional radio relic of Fig. 4.2.

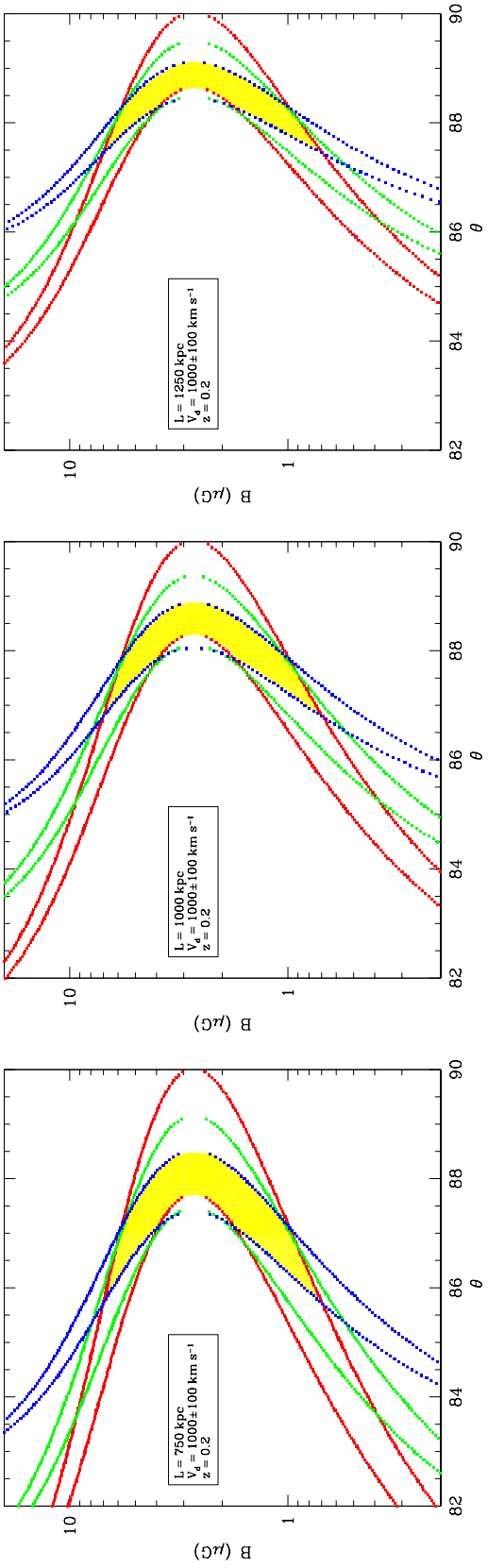

Figure A.1: Effects of L on magnetic field and angle contour regions (see panel for the parameters). At the center the "standard" fictional radio relic is reported. Three frequencies are considered (color scheme: *red* for the low-frequency, *green* for the intermediate-frequency and *blue* for the high-frequency). The *yellow* regions display the "allowed" combination of (B, θ).

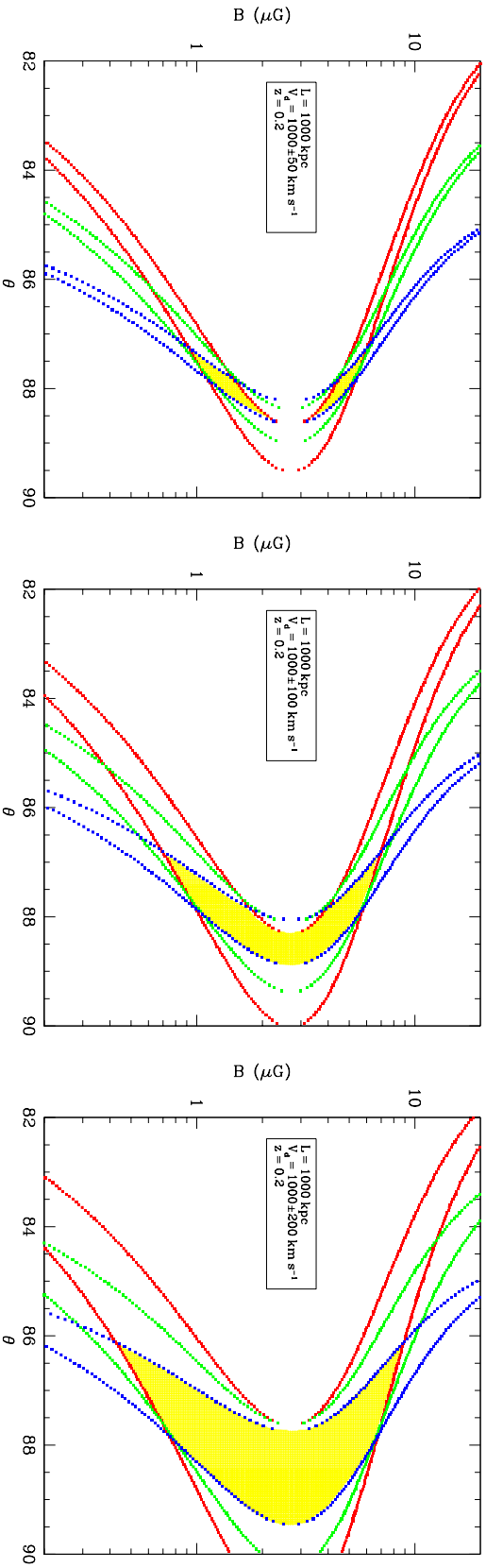

Figure A.2: Effects of $\frac{\sigma_{V_d}}{V_d}$ on magnetic field and angle contour regions (see panel for the parameters). At the center the "standard" fictional radio relic is reported. Three frequencies are considered (color scheme: *red* for the low-frequency, *green* for the intermediate-frequency and *blue* for the high-frequency). The *yellow* regions display the "allowed" combination of (B, θ).

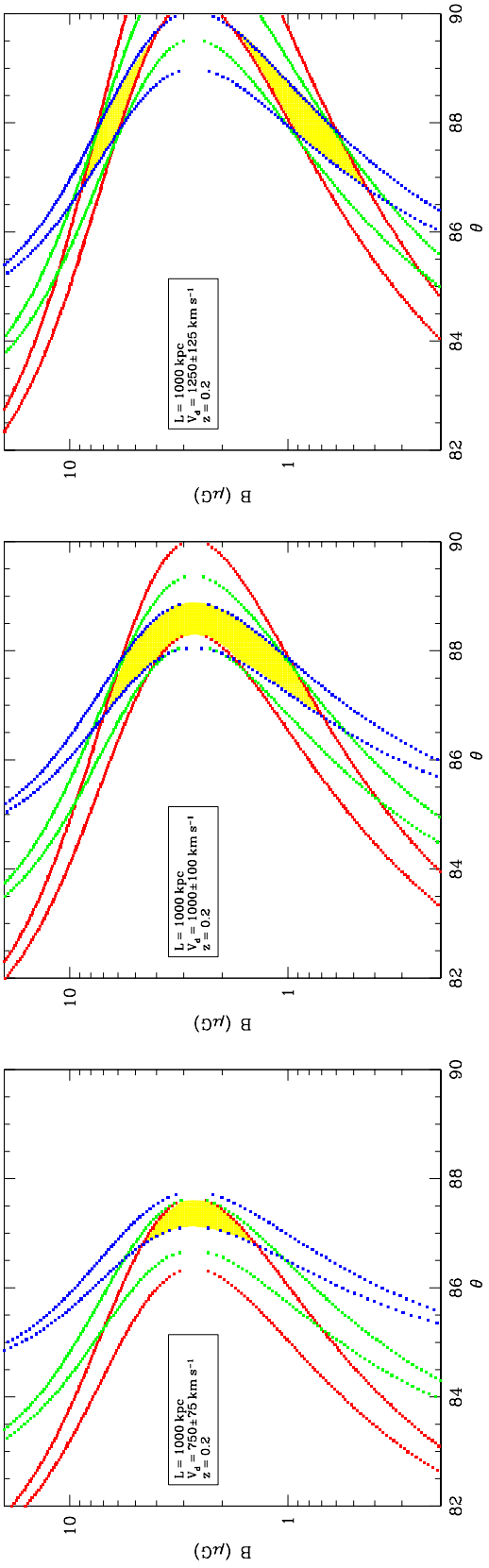

Figure A.3: Effects of V_d on magnetic field and angle contour regions (see panel for the parameters). At the center the "standard" fictional radio relic is reported. Three frequencies are considered (color scheme: *red* for the low-frequency, *green* for the intermediate-frequency and *blue* for the high-frequency). The *yellow* regions display the "allowed" combination of (B, θ).

Bibliography

Abell, G. O. 1958, ApJS, 3, 211

Abell, G. O. 1965, A&A Rev., 3, 1

Ackermann, M., Ajello, M., Albert, A., et al. 2014, ApJ, 787, 18

Ackermann, M., Ajello, M., Allafort, A., et al. 2010, ApJ, 717, L71

Akamatsu, H., Inoue, S., Sato, T., et al. 2013, PASJ, 65, 89

Akamatsu, H. & Kawahara, H. 2013, PASJ, 65, 16

Akamatsu, H., Takizawa, M., Nakazawa, K., et al. 2012, PASJ, 64, 67

Aleksić, J., Alvarez, E. A., Antonelli, L. A., et al. 2012, A&A, 541, A99

Allen, S. W., Taylor, G. B., Nulsen, P. E. J., et al. 2001, MNRAS, 324, 842

Arnaud, M., Aghanim, N., Gastaud, R., et al. 2001, A&A, 365, L67

Arnaud, M., Maurogordato, S., Slezak, E., & Rho, J. 2000, A&A, 355, 461

Bacchi, M., Feretti, L., Giovannini, G., & Govoni, F. 2003, A&A, 400, 465

Bagchi, J., Durret, F., Neto, G. B. L., & Paul, S. 2006, Science, 314, 791

Bagchi, J., Enßlin, T. A., Miniati, F., et al. 2002, Nature, 7, 249

Bagchi, J., Pislar, V., & Lima Neto, G. B. 1998, MNRAS, 296, L23

Bahcall, N. A. & Lubin, L. M. 1994, ApJ, 426, 513

Bartels, R., Zandanel, F., & Ando, S. 2015, ArXiv e-prints

Begeman, K. G., Broeils, A. H., & Sanders, R. H. 1991, MNRAS, 249, 523

Bell, A. R. 1978a, MNRAS, 182, 147

Bell, A. R. 1978b, MNRAS, 182, 443

Berezinsky, V. S., Blasi, P., & Ptuskin, V. S. 1997, ApJ, 487, 529

Best, P. N., von der Linden, A., Kauffmann, G., Heckman, T. M., & Kaiser, C. R. 2007, MNRAS, 379, 894

Bicknell, G. V., de Ruiter, H. R., Parma, P., Morganti, R., & Fanti, R. 1990, ApJ, 354, 98

Biermann, L. 1950, Z. Naturforsch. A Phys. Sci., 5, 65

Blandford, R. & Eichler, D. 1987, Phisics Rep., 154, 1

Blasi, P. 2000, ApJ, 532, L9

Blasi, P. & Colafrancesco, S. 1999, Astropart. Phys., 12, 169

Blasi, P., Gabici, S., & Brunetti, G. 2007, Int. J. Mod. Phys. A, 22, 681

Bonafede, A., Feretti, L., Giovannini, G., et al. 2009a, A&A, 503, 707

Bonafede, A., Feretti, L., Murgia, M., et al. 2010, A&A, 513, A30

Bonafede, A., Giovannini, G., Feretti, L., Govoni, F., & Murgia, M. 2009b, A&A, 494, 429

Bonafede, A., Intema, H. T., Brüggen, M., et al. 2014, ApJ, 785, 1

Bonafede, A., Vazza, F., Brüggen, M., et al. 2013, MNRAS, 433, 3208

Boschin, W., Girardi, M., & Barrena, R. 2013, MNRAS, 434, 772

Bourdin, H., Mazzotta, P., Markevitch, M., Giacintucci, S., & Brunetti, G. 2013, ApJ, 764, 82

Briel, U. G., Henry, J. P., & Boehringer, H. 1992, A&A, 259, L31

Briel, U. G., Henry, J. P., Lumb, D. H., et al. 2001, A&A, 365, L60

Brown, S. & Rudnick, L. 2009, AJ, 137, 3158

Brown, S. & Rudnick, L. 2011, MNRAS, 412, 2

Brüggen, M., van Weeren, R. J., & Röttgering, H. J. A. 2012, MNRAS, 425, L76

Brunetti, G. 2004, in The Role of VLBI in Astrophysics, Astrometry and Geodesy, ed. F. Mantovani & A. Kus, 29

Brunetti, G., Blasi, P., Reimer, O., et al. 2012, MNRAS, 426, 956

Brunetti, G., Cassano, R., Dolag, K., & Setti, G. 2009, A&A, 507, 661

Brunetti, G., Giacintucci, S., Cassano, R., et al. 2008, Nature, 455, 944

Brunetti, G. & Jones, T. W. 2014, Int. J. Mod. Phys. D, 23, 30007

Brunetti, G. & Lazarian, A. 2007, MNRAS, 378, 245

Brunetti, G. & Lazarian, A. 2011, MNRAS, 410, 127

Brunetti, G., Setti, G., & Comastri, A. 1997, A&A, 325, 898

Brunetti, G., Setti, G., Feretti, L., & Giovannini, G. 2001, MNRAS, 320, 365

Brunetti, G., Venturi, T., Dallacasa, D., et al. 2007, ApJ, 670, L5

Burkert, A. 1995, ApJ, 447, L25

Burns, J. O., Skillman, S. W., & O'Shea, B. W. 2010, ApJ, 721, 1105

Bykov, A. M., Dolag, K., & Durret, F. 2008, Space Sci. Rev., 134, 119

Carilli, C. L. & Taylor, G. B. 2002, ARA&A, 40, 319

Carlstrom, J. E., Holder, G. P., & Reese, E. D. 2002, ARA&A, 40, 643

Cassano, R. & Brunetti, G. 2005, MNRAS, 357, 1313

Cassano, R., Brunetti, G., Norris, R. P., et al. 2012, A&A, 548, A100

Cassano, R., Brunetti, G., & Setti, G. 2006, MNRAS, 369, 1577

Cassano, R., Ettori, S., Brunetti, G., et al. 2013, ApJ, 777, 141

Cassano, R., Ettori, S., Giacintucci, S., et al. 2010, ApJ, 721, L82

Cassano, R., Gitti, M., & Brunetti, G. 2008, A&A, 486, L31

Cavaliere, A. & Fusco-Femiano, R. 1976, A&A, 49, 137

Cavaliere, A. & Fusco-Femiano, R. 1978, A&A, 70, 677

Chandran, B. D. G. & Cowley, S. C. 1998, Phys. Rev. Lett., 80, 3077

Clarke, T. E. & Enßlin, T. A. 2006, AJ, 131, 2900

Clarke, T. E., Kronberg, P. P., & Böhringer, H. 2001, ApJ, 547, L111

Coles, P. & Lucchin, F. 2002, Cosmology: The Origin and Evolution of Cosmic Structure, Second Edition

Cowie, L. L. & Songaila, A. 1977, Nature, 266, 501

Crawford, C. S., Allen, S. W., Ebeling, H., Edge, A. C., & Fabian, A. C. 1999, MNRAS, 306, 857

Dallacasa, D., Brunetti, G., Giacintucci, S., et al. 2009, ApJ, 699, 1288

de Gasperin, F., van Weeren, R. J., Brüggen, M., et al. 2014, MNRAS, 444, 3130

De Grandi, S., Ettori, S., Longhetti, M., & Molendi, S. 2004, A&A, 419, 7

De Grandi, S. & Molendi, S. 2001, ApJ, 551, 153

De Lucia, G. & Blaizot, J. 2007, MNRAS, 375, 2

De Lucia, G., Kauffmann, G., & White, S. D. M. 2004, MNRAS, 349, 1101

Deiss, B. M., Reich, W., Lesch, H., & Wielebinski, R. 1997, A&A, 321, 55

Dennison, B. 1980, ApJ, 239, L93

Dicke, R. H., Peebles, P. J. E., Roll, P. G., & Wilkinson, D. T. 1965, ApJ, 142, 414

Dogiel, V. A. 2000, A&A, 357, 66

Dolag, K., Bykov, A. M., & Diaferio, A. 2008, Space Sci. Rev., 134, 311

Dolag, K., Grasso, D., Springel, V., & Tkachev, I. 2005a, JCAP, 1, 9

Dolag, K., Schindler, S., Govoni, F., & Feretti, L. 2001, A&A, 378, 777

Dolag, K., Vazza, F., Brunetti, G., & Tormen, G. 2005b, MNRAS, 364, 753

Donnert, J., Dolag, K., Brunetti, G., & Cassano, R. 2013, MNRAS, 429, 3564

Dreher, J. W., Carilli, C. L., & Perley, R. A. 1987, ApJ, 316, 611

Dressler, A. 1980, ApJ, 236, 351

Drury, L. O. 1983, Rep. Prog. Phys., 46, 973

Einasto, J. 1965, TrAIm, 5, 87

Enßlin, T. A., Biermann, P. L., Klein, U., et al. 1998, A&A, 332, 395

Enßlin, T. A., Kronberg, P. P., Perley, R. A., & Kassim, N. E. 1999a, in Diffuse Thermal and Relativistic Plasma in Galaxy Clusters, ed. H. Boehringer, L. Feretti, & P. Schuecker, 21

Enßlin, T. A., Lieu, R., & Biermann, P. L. 1999b, A&A, 344, 409

Enßlin, T. A., Pfrommer, C., Miniati, F., & Subramanian, K. 2011, A&A, 527, A99

Ettori, S. & Fabian, A. C. 2000, MNRAS, 317, L57

Ettori, S., Gastaldello, F., Gitti, M., et al. 2013, A&A, 555, A93

Fabian, A. C. 1994, ARA&A, 32, 277

Fabian, A. C., Sanders, J. S., Allen, S. W., et al. 2003, MNRAS, 344, L43

Fabian, A. C., Sanders, J. S., Ettori, S., et al. 2000, MNRAS, 318, L65

Felten, J. E. 1996, in Astronomical Society of the Pacific Conference Series, Vol. 88, Clusters, Lensing and the Future of the Universe, ed. V. Trimble & A. Reisenegger, 271

Feretti, L. 1999, in Diffuse Thermal and Relativistic Plasma in Galaxy Clusters, ed. H. Boehringer, L. Feretti, & P. Schuecker, 3

Feretti, L., Dallacasa, D., Giovannini, G., & Tagliani, A. 1995, A&A, 302, 680

Feretti, L., Dallacasa, D., Govoni, F., et al. 1999, A&A, 344, 472

Feretti, L., Fusco-Femiano, R., Giovannini, G., & Govoni, F. 2001, A&A, 373, 106

Feretti, L., Giovannini, G., Govoni, F., & Murgia, M. 2012, A&A Rev., 20, 54

Feretti, L. & Neumann, D. M. 2006, A&A, 450, L21

Ferrari, C., Arnaud, M., Ettori, S., Maurogordato, S., & Rho, J. 2006, A&A, 446, 417

Ferrari, C., Govoni, F., Schindler, S., Bykov, A. M., & Rephaeli, Y. 2008, Space Sci. Rev., 134, 93

Ferrari, C., Maurogordato, S., Cappi, A., & Benoist, C. 2003, A&A, 399, 813

Finoguenov, A., Sarazin, C. L., Nakazawa, K., Wik, D. R., & Clarke, T. E. 2010, ApJ, 715, 1143

Fixsen, D. J. 2009, ApJ, 707, 916

Fujita, Y., Takizawa, M., & Sarazin, C. L. 2003, ApJ, 584, 190

Fusco-Femiano, R., Dal Fiume, D., De Grandi, S., et al. 2000, ApJ, 534, L7

Fusco-Femiano, R., Dal Fiume, D., Feretti, L., et al. 1999, ApJ, 513, L21

Fusco-Femiano, R., Dal Fiume, D., Orlandini, M., et al. 2001, ApJ, 552, L97

Fusco-Femiano, R., Landi, R., & Orlandini, M. 2007, ApJ, 654, L9

Fusco-Femiano, R., Orlandini, M., Brunetti, G., et al. 2004, ApJ, 602, L73

Gallagher, J. S. & Ostriker, J. P. 1972, AJ, 77, 288

Gaspari, M., Melioli, C., Brighenti, F., & D'Ercole, A. 2011, MNRAS, 411, 349

Giacintucci, S., Venturi, T., Bardelli, S., et al. 2006, Nature, 11, 437

Giacintucci, S., Venturi, T., Macario, G., et al. 2008, A&A, 486, 347

Giovanelli, R. & Haynes, M. P. 1985, ApJ, 292, 404

Giovannini, G., Bonafede, A., Feretti, L., Govoni, F., & Murgia, M. 2010, A&A, 511, L5

Giovannini, G., Bonafede, A., Feretti, L., et al. 2009, A&A, 507, 1257

Giovannini, G. & Feretti, L. 2004, JKAS, 37, 323

Giovannini, G., Feretti, L., & Stanghellini, C. 1991, A&A, 252, 528

Giovannini, G., Feretti, L., Venturi, T., Kim, K.-T., & Kronberg, P. P. 1993, ApJ, 406, 399

Gitti, M., Brighenti, F., & McNamara, B. R. 2012, Adv. Astron., 2012, 6

Gitti, M., Brunetti, G., Feretti, L., & Setti, G. 2004, A&A, 417, 1

Gitti, M., Brunetti, G., & Setti, G. 2002, A&A, 386, 456

Gitti, M., Ferrari, C., Domainko, W., Feretti, L., & Schindler, S. 2007, A&A, 470, L25

Gómez, P. L., Loken, C., Roettiger, K., & Burns, J. O. 2002, ApJ, 569, 122

Govoni, F., Enßlin, T. A., Feretti, L., & Giovannini, G. 2001, A&A, 369, 441

Govoni, F. & Feretti, L. 2004, Int. J. Mod. Phys. D, 13, 1549

Govoni, F., Murgia, M., Feretti, L., et al. 2005, A&A, 430, L5

Govoni, F., Murgia, M., Feretti, L., et al. 2006, A&A, 460, 425

Govoni, F., Murgia, M., Markevitch, M., et al. 2009, A&A, 499, 371

Grasso, D. & Rubinstein, H. R. 2001, Phys. Rep., 348, 163

Guidetti, D., Murgia, M., Govoni, F., et al. 2008, A&A, 483, 699

Gunn, J. E. & Gott, J. R. 1972, ApJ, 176, 1

Harris, D. E. & Grindlay, J. E. 1979, MNRAS, 188, 25

Hoeft, M. & Brüggen, M. 2007, MNRAS, 375, 77

Hong, S. E., Kang, H., & Ryu, D. 2015, ArXiv e-prints

Iapichino, L. & Brüggen, M. 2012, MNRAS, 423, 2781

Jaffe, W. J. 1977, ApJ, 212, 1

Jaffe, W. J. 1980, ApJ, 241, 925

Jeltema, T. E. & Profumo, S. 2011, ApJ, 728, 53

Johnston-Hollitt, M. 2003, PhD thesis, University of Adelaide

Jones, F. C. & Ellison, D. C. 1991, Space Sci. Rev., 58, 259

Kale, R., Venturi, T., Giacintucci, S., et al. 2015, ArXiv e-prints

Kang, H. & Jones, T. W. 2005, ApJ, 620, 44

Kang, H., Ryu, D., & Jones, T. W. 2012, ApJ, 756, 97

Kauffmann, G., White, S. D. M., & Guiderdoni, B. 1993, MNRAS, 264, 201

Kempner, J. C., Blanton, E. L., Clarke, T. E., et al. 2004, in The Riddle of Cooling Flows in Galaxies and Clusters of galaxies, ed. T. Reiprich, J. Kempner, & N. Soker, 335

Keshet, U. & Loeb, A. 2010, ApJ, 722, 737

Kim, K.-T., Kronberg, P. P., Dewdney, P. E., & Landecker, T. L. 1990, ApJ, 355, 29

Kim, K.-T., Kronberg, P. P., Giovannini, G., & Venturi, T. 1989, Nature, 341, 720

Kim, K.-T., Tribble, P. C., & Kronberg, P. P. 1991, ApJ, 379, 80

King, I. 1962, AJ, 67, 471

Kritsuk, A. G. 1983, Afz, 19, 263

Kronberg, P. P. 2002, Phys. Today, 55, 40

Kronberg, P. P., Lesch, H., & Hopp, U. 1999, ApJ, 511, 56

Krymskii, G. F. 1977, Dokl. Akad. Nauk SSSR, 234, 1306

Lacey, C. & Cole, S. 1993, MNRAS, 262, 627

Landau, L. D. & Lifshitz, E. M. 1959, Fluid mechanics

Large, M. I., Mathewson, D. S., & Haslam, C. G. T. 1959, Nature, 183, 1663

Limber, D. N. & Mathews, W. G. 1960, ApJ, 132, 286

Macario, G., Venturi, T., Brunetti, G., et al. 2010, A&A, 517, A43

Macario, G., Venturi, T., Intema, H. T., et al. 2013, A&A, 551, A141

Malkov, M. A. & Drury, L. O. 2001, Rep. Prog. Phys., 64, 429

Markevitch, M., Govoni, F., Brunetti, G., & Jerius, D. 2005, ApJ, 627, 733

Markevitch, M., Ponman, T. J., Nulsen, P. E. J., et al. 2000, ApJ, 541, 542

Markevitch, M. & Vikhlinin, A. 2007, Phys. Rep., 443, 1

Maurogordato, S., Proust, D., Beers, T. C., et al. 2000, A&A, 355, 848

Mazzotta, P. & Giacintucci, S. 2008, ApJ, 675, L9

McNamara, B. R. & Nulsen, P. E. J. 2007, ARA&A, 45, 117

Merritt, D. 1984, ApJ, 280, L5

Miniati, F. 2015, ApJ, 800, 60

Miniati, F., Jones, T. W., Kang, H., & Ryu, D. 2001, ApJ, 562, 233

Mukhanov, V. F. & Chibisov, G. V. 1981, J. Exp. Theor. Phys., 33, 532

Murgia, M., Govoni, F., Feretti, L., et al. 2004, A&A, 424, 429

Murgia, M., Govoni, F., Markevitch, M., et al. 2009, A&A, 499, 679

Mushotzky, R. F. 1984, Phys. Scr. Vol. T, 7, 157

Nakazawa, K., Sarazin, C. L., Kawaharada, M., et al. 2009, PASJ, 61, 339

Navarro, J. F., Frenk, C. S., & White, S. D. M. 1997, ApJ, 490, 493

Newman, W. I., Newman, A. L., & Rephaeli, Y. 2002, ApJ, 575, 755

Oemler, A. 1976, ApJ, 209, 693

Ogrean, G. A., Brüggen, M., Röttgering, H. J. A., et al. 2013a, MNRAS, 429, 2617

Ogrean, G. A., Brüggen, M., van Weeren, R. J., et al. 2013b, MNRAS, 433, 812

Ogrean, G. A., Brüggen, M., van Weeren, R. J., et al. 2014, MNRAS, 440, 3416

Ostriker, J. P. & Hausman, M. A. 1977, ApJ, 217, L125

Pacholczyk, A. G. 1970, Radio astrophysics. Nonthermal processes in galactic and extragalactic sources

Pariiskii, Y. N. 1972, AZh, 49, 1322

Parma, P., Murgia, M., Morganti, R., et al. 1999, A&A, 344, 7

Pentericci, L., Van Reeven, W., Carilli, C. L., Röttgering, H. J. A., & Miley, G. K. 2000, A&AS, 145, 121

Penzias, A. A. & Wilson, R. W. 1965, ApJ, 142, 419

Perkins, J. S., Badran, H. M., Blaylock, G., et al. 2006, ApJ, 644, 148

Perley, R. A. & Taylor, G. B. 1991, AJ, 101, 1623

Peterson, J. R. & Fabian, A. C. 2006, Phys. Rep., 427, 1

Petrosian, V. 2001, ApJ, 557, 560

Pfrommer, C. & Enßlin, T. A. 2004, A&A, 413, 17

Pinzke, A., Oh, S. P., & Pfrommer, C. 2013, MNRAS, 435, 1061

Pinzke, A., Oh, S. P., & Pfrommer, C. 2015, ArXiv e-prints

Planck Collaboration. 2011, A&A, 536, A8

Planck Collaboration. 2013, A&A, 554, A140

Planck Collaboration. 2015, ArXiv e-prints

Rephaeli, Y. 1979, ApJ, 227, 364

Rephaeli, Y., Gruber, D. E., & Blanco, P. 1999, ApJ, 511, L21

Rephaeli, Y., Gruber, D. E., & Rothschild, R. E. 1987, ApJ, 320, 139

Riquelme, M. A. & Spitkovsky, A. 2010, ApJ, 717, 1054

Roettiger, K., Burns, J. O., & Loken, C. 1996, ApJ, 473, 651

Roettiger, K., Burns, J. O., & Stone, J. M. 1999a, ApJ, 518, 603

Roettiger, K., Loken, C., & Burns, J. O. 1997, A&AS, 109, 307

Roettiger, K., Stone, J. M., & Burns, J. O. 1999b, ApJ, 518, 594

Rosati, P., Borgani, S., & Norman, C. 2002, ARA&A, 40, 539

Rosati, P., Della Ceca, R., Norman, C., & Giacconi, R. 1998, ApJ, 492, L21

Rossetti, M. & Molendi, S. 2004, A&A, 414, L41

Rottgering, H. J. A., Wieringa, M. H., Hunstead, R. W., & Ekers, R. D. 1997, MNRAS, 290, 577

Rudnick, L. & Blundell, K. M. 2003, ApJ, 588, 143

Ryu, D., Kang, H., & Biermann, P. L. 1998, A&A, 335, 19

Ryu, D., Kang, H., Hallman, E. J., & Jones, T. W. 2003, ApJ, 593, 599

Sarazin, C. L. 1986, Rev. Mod. Phys., 58, 1

Sarazin, C. L. & Kempner, J. C. 2000, ApJ, 533, 73

Schlickeiser, R., Sievers, A., & Thiemann, H. 1987, A&A, 182, 21

Sijbring, L. G. 1993, A radio continuum and HI line study of the perseus cluster

Simionescu, A., Werner, N., Urban, O., et al. 2013, ApJ, 775, 4

Skillman, S. W., Xu, H., Hallman, E. J., et al. 2013, ApJ, 765, 21

Soucail, G., Fort, B., Mellier, Y., & Picat, J. P. 1987, A&A, 172, L14

Spitzer, L. 1962, Physics of Fully Ionized Gases

Spitzer, L. & Baade, W. 1951, ApJ, 113, 413

Springel, V., Frenk, C. S., & White, S. D. M. 2006, Nature, 440, 1137

Springel, V., White, S. D. M., Jenkins, A., et al. 2005, Nature, 435, 629

Stroe, A., Harwood, J. J., Hardcastle, M. J., & Röttgering, H. J. A. 2014a, MNRAS, 445, 1213

Stroe, A., Rumsey, C., Harwood, J. J., et al. 2014b, MNRAS, 441, L41

Stroe, A., van Weeren, R. J., Intema, H. T., et al. 2013, A&A, 555, A110

Sunyaev, R. A. & Zeldovich, Y. B. 1972, CoASP, 4, 173

Tarter, J. C. 1975, PhD thesis, University of Berkeley

Taylor, G. B. & Perley, R. A. 1993, ApJ, 416, 554

Thierbach, M., Klein, U., & Wielebinski, R. 2003, A&A, 397, 53

Tribble, P. C. 1991, MNRAS, 253, 147

van Weeren, R. J., Andrade-Santos, F., Brüggen, M., et al. 2015, ApJ (submitted)

van Weeren, R. J., Brüggen, M., Röttgering, H. J. A., & Hoeft, M. 2011, MNRAS, 418, 230

van Weeren, R. J., Röttgering, H. J. A., Bagchi, J., et al. 2009a, A&A, 506, 1083

van Weeren, R. J., Röttgering, H. J. A., Brüggen, M., & Cohen, A. 2009b, A&A, 505, 991

van Weeren, R. J., Röttgering, H. J. A., Brüggen, M., & Hoeft, M. 2010, Science, 330, 347

van Weeren, R. J., Röttgering, H. J. A., Intema, H. T., et al. 2012, A&A, 546, A124

Vazza, F., Brüggen, M., Gheller, C., & Wang, P. 2014, MNRAS, 445, 3706

Vazza, F., Brüggen, M., van Weeren, R. J., et al. 2012, MNRAS, 421, 1868

Vazza, F., Brunetti, G., & Gheller, C. 2009a, MNRAS, 395, 1333

Vazza, F., Brunetti, G., Kritsuk, A., et al. 2009b, A&A, 504, 33

Vazza, F., Ferrari, C., Brüggen, M., et al. 2015, ArXiv e-prints

Vazza, F., Tormen, G., Cassano, R., Brunetti, G., & Dolag, K. 2006, MNRAS, 369, L14

Venturi, T., Giacintucci, S., Dallacasa, D., et al. 2013, A&A, 551, A24

Vikhlinin, A., Markevitch, M., & Murray, S. S. 2001a, ApJ, 551, 160

Vikhlinin, A., Markevitch, M., & Murray, S. S. 2001b, ApJ, 549, L47

Voges, W., Aschenbach, B., Boller, T., et al. 1999, A&A, 349, 389

Völk, H. J., Aharonian, F. A., & Breitschwerdt, D. 1996, Space Sci. Rev., 75, 279

Watson, D., Christensen, L., Knudsen, K. K., et al. 2015, Nature, 519, 327

Wik, D. R., Sarazin, C. L., Finoguenov, A., et al. 2011, ApJ, 727, 119

Wik, D. R., Sarazin, C. L., Finoguenov, A., et al. 2009, ApJ, 696, 1700

Willson, M. A. G. 1970, MNRAS, 151, 1

Xu, H., Li, H., Collins, D. C., Li, S., & Norman, M. L. 2009, ApJ, 698, L14

Zandanel, F., Colin, P., Lombardi, S., et al. 2013, ArXiv e-prints

ZuHone, J. A., Brunetti, G., Giacintucci, S., & Markevitch, M. 2015, ApJ, 801, 146

ZuHone, J. A., Markevitch, M., & Brunetti, G. 2011a, Mem. Soc. Astron. Ital., 82, 632

ZuHone, J. A., Markevitch, M., Brunetti, G., & Giacintucci, S. 2013, ApJ, 762, 78

ZuHone, J. A., Markevitch, M., & Lee, D. 2011b, ApJ, 743, 16

Zwicky, F. 1937, ApJ, 86, 217